UNIVERSIDAD DE SONORA
DIVISIÓN DE CIENCIAS EXACTAS Y NATURALES
Departamento de Investigación en Física

UV INDUCED AFTERGLOW AND THERMOLUMINESCENCE IN EU-DOPED ALKALI HALIDES AT LOW TEMPERATURE

Tesis

que para cubrir parcialmente los requisitos para obtener el grado de:

DOCTOR EN CIENCIAS (FÍSICA)

presenta:

SUSANA ÁLVAREZ GARCÍA

HERMOSILLO, SONORA

20 DE ABRIL DE 2005

Universidad de Sonora

Repositorio Institucional UNISON

ABSTRACT

This work is focused on the study of the mechanisms involved in the afterglow (AG) and the thermoluminescence (TL) phenomena in Eu-doped alkali halides exposed to low-energy UV radiation at low temperature. Our study of the radiation induced defect formation and defect recombination is based on the excitonic theory. In pure alkali halides, this theory establishes that the primary products of irradiation are F centers and H centers. The process of formation of these defects from free electrons and holes implies the formation of self-trapped excitons (STEs) which relax to an off center configuration similar to nearest neighbor F–H defect pairs. The formation of a stable defect pair would be due by the migration of the H center far enough from the F center position.

In Eu-doped alkali halides, the formation of stable defects responsible for AG and TL phenomena could be observed after irradiation with UV light of energy close to the high-energy absorption band of the Eu-impurity. It was considered that UV irradiation at low temperature induces the formation of a STE in the vicinity of the impurity which results in the formation of an F–H pair. We propose that the migration of the H center occurs along dislocation lines. This model predicts that the AG decay follows a $t^{-3/2}$ law after pulsed irradiation.

Our experimental work is developed in a research facility designed to perform systematic studies of PL, AG and TL after irradiation with UV-visible light at temperatures from 20 K to 300 K. The Eu-doped alkali halide samples were submitted to different thermal treatments which are known to be efficient for the precipitation of the impurity in different phases. The participation of the dislocation lines in the AG and TL phenomena was analyzed by exposing the samples to deformation treatments which results in the movement and the formation of dislocations.

The experiments show a higher participation of Eu-aggregates in the AG and TL process than Eu-v_c dipoles. Furthermore, it is shown that the participation of dipoles is much higher in deformed crystals. This results allow us to propose that: (1) radiation induced defect

formation at low temperature occurs mainly around dislocations because they may serve as guiding lines for the H centers to separate from the F center to form stable F–H center pairs. Here it is assumed that the migration of H centers in dislocation lines is fast compared to the migration in the bulk at temperatures too low to allow the H-center migration through the bulk; (2) aggregation of impurity ions occurs mainly near dislocations because, firstly, impurity ions migrate faster along dislocation lines causing the aggregation rate to increase and secondly the impurity ions are trapped into dislocations where they remain mobile along the dislocation.

CONTENTS

INTRODUCTION

Europium doped alkali halides have some excellent properties of energy conversion and storage of ionizing radiation. During the last fifty years, these properties and the underlying mechanisms have been extensively investigated and a great deal of our knowledge about these mechanisms is now well established. Applications of these mechanisms can be found in thermoluminescent dosimeters, two-dimensional X-ray imaging plates and erasable/rewritable optical memories [Schlapp 2002, Nensel 1998, Nanto 1994]. Furthermore, the knowledge assimilated in alkali halides could be applied to other materials like for example Eu-doped BaFBr crystals. The latter one is actually the commercial material used in the previous mentioned applications [Schlapp 2004, Hesse 2004, Seggern 1999, Kimura 1998, Rüter 1990].

Europium doped alkali halides also are sensible to UV-light. This is an interesting property for applications in personal dosimetry of UV light in the actinic region and for this reason they received much attention [Aguirre 1989]. In fact, the process of defect formation responsible for the UV sensibility has been one of the main topics of research in our laboratory (*Laboratorio de Estado Sólido del Departamento de Investigación en Física de la Universidad de Sonora*) for more than two decades [see for example, Larios-Cota 1980]. Although some progress in understanding the mechanism for UV induced defect formation was achieved, many aspects remained puzzling. It was found that non-ionizing UV light produces radiation defects like F and F_Z centers with a strong preference for F_Z center formation [Aceves 1994]. When the work of this thesis started, several projects concerning the mechanism of UV induced formation and dosimetric properties in Eu-doped alkali halides were running. In these projects optically stimulated luminescence, photo-transfer and thermoluminescence (TL) mainly at room temperature (RT) were investigated. However, it was soon realized that the mechanism of defect formation at RT was obscured by non-well understood thermally assisted processes. Therefore several lines of investigation were started at low temperature of which

one of them was dedicated to the afterglow (AG) and TL at low temperature. In this line of investigation, the work described in this thesis has been performed.

The main puzzle to resolve was why apparently electron and hole traps, as revealed in TL and AG experiments, were formed by UV-radiation with too low energy for ionizing the lattice. The model for radiation induced defect formation and defect recombination applied in our group was based on the energy band theory of insulators [Piters 1993]. This theory is most easily explained by the energy level diagram as schematically shown in Fig. I.1. The levels are concentrated in the core bands (not shown in Fig. I.1), valence band and the conduction band. For a crystal without lattice defects there are no energy levels between these bands that could be occupied by electrons (band gap). However when a crystal contains defects (intrinsic or by addition of impurities), the lattice is locally distorted giving rise to localized energy levels between the valence and the conduction band. In the ground state all electrons are localized in the core bands, valence band and the lowest energy levels at the defects.

During irradiation (Fig. I.1a), electrons may transit from the valence band into the conduction band leaving a hole in the valence band (transition [1]). The electron and hole wander through the lattice and come across lattice defects. The electron may be trapped by a transition to the lowest available energy level at the defect (transition [2]). The hole may also

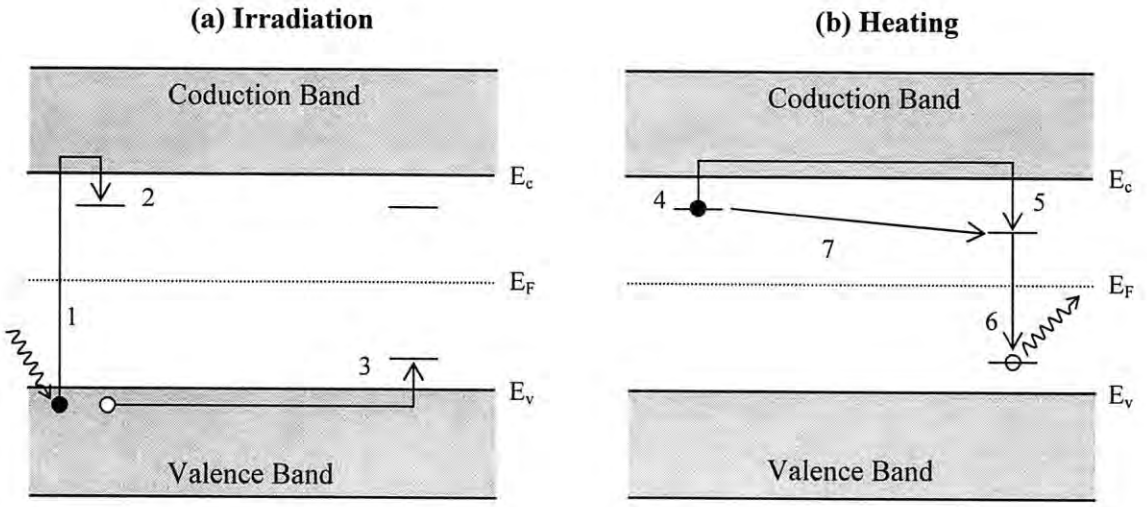

Fig. I.1. Band model for creation and recombination of damage. E_C is the energy of the bottom of the conduction band, E_V is the energy of the top of the valence band and E_F is the Fermi energy. Electrons are denoted by filled circles, holes by open circles and transitions by arrows.

be trapped at a lattice defect by a transition of the electron from the lowest energy level above the valence band (transition [3]). So after irradiation an amount of energy is stored in the crystal in the form of separated charges.

When the crystals is heated (Fig. I.1b), the charges may be thermally released. The temperature at which the carriers (electrons or holes) are released depends on the energy difference of the trap and the conduction band (for electrons) or the valence band (for holes). Then, at a certain temperature the electrons trapped at a specific defect are released (transition [4]). The released electrons wander through the conduction band and may across a defect with a trapped hole. Due to the relaxation of the lattice around the defect according the new situation, the electron transits from the ionized state (free electron in the conduction band) to and excited state (transition [5]). This transition is radiationless. The excited electron transits to the ground state (recombination of hole and electron) resulting in TL emission (transition [6]). A non-thermal transition of the electron from the electron-trap to the excited state (transitions [7]) could occurs via an electron tunneling process between the energy levels. From here, the recombination occurs through transition [6] resulting in AG luminescence.

Following this model, the dominant theory for the formation of defects during UV-irradiation with photon energy less than the band gap was that the electrons come from the UV-ionization of the Eu impurity. However, the observation of free electrons by photoconductivity measurements that initially supported this theory [Aguirre 1988] could not be confirmed. Furthermore, the Eu^{3+} as product of the Eu ionization was not observed after UV irradiation. Only in highly precipitated Eu-doped NaCl crystals irradiated with X-rays and in highly doped KCl:Eu crystals [Aguilar 1982], Eu^{3+} could be detected. Furthermore, several authors suggests that Eu^{3+} can not be formed in dilute Eu-doped alkali halides in which TL and AG was observed [Opyrchal 1986].

Because of the controversies over this mechanism, we change radically our approach to the problem. We discard the concept of electron and hole traps and we adopt the excitonic theory of radiation defect formation. In this theory, F centers (an anion vacancy with a bound electron) and H centers (a X_2^- molecule at the anion lattice site aligned in the <110> direction) are considered as the primary radiation products. The H center plays the role of the mobile entity instead of the electron in the energy band theory. Although we realize that

electron traps could be present in the crystal, we consider that they do not contribute significantly to any process or mechanism explaining the results of this thesis.

The excitonic theory of defect formation is well established and a description of our actual knowledge about the creation and recombination of defect centers in pure alkali halides is presented in Chapter 1. The reported studies about the role played by the Eu impurity in alkali halides exposed to X- and UV-radiation is also included. Chapter 1 is planned as an introduction to the theory of defect formation by excitonic mechanism and provide us a justification to treat the AG and TL as resulting from F and H center production during irradiation. Assuming the formation of F and H centers, we developed an alternative model for AG not based on tunneling but on H center migration. This model is presented in Chapter 2. An analytical approach of the AG-decay time dependency and results of a simulation analysis complete the discussion. In Chapter 3 the experimental setup designed to automate the measurements of AG and TL luminescence under UV irradiation is described. Chapter 4 presents the general features of the AG and TL in different Eu-doped alkali halides. Chapter 5 presents the influence of the precipitated/aggregated state of the Eu impurity in the AG and TL in KCl:Eu crystals. Chapter 6 presents the effect of press treatments in the AG and TL in KCl:Eu. Finally, the general conclusions and the perspectives of this work are discussed.

CHAPTER 1:
THEORETICAL REVIEW

This thesis is focused on the study of the mechanisms involved in the afterglow and the thermoluminescence in Eu-doped alkali halides. Thermoluminescence has been extensively studied due to its application to the study of the dosimetric properties of the materials. There are two different approaches to explain the thermoluminescence phenomena: the mobile electron model based on the energy band theory of insulators [review in Chen 1997] and the mobile interstitial model based on the theory of the creation of F–H defect centers during irradiation. The first model has been extensively used to describe the kinetics of TL and related phenomena and its dosimetric application. The second model is less common extended in TL studies however it presents a more realistic view of the physical processes occurring in the crystal during and after the irradiation. Our following discussion will be based on the second model. In view of that, this chapter is initiated with a review of our present knowledge of the formation of stable defects in pure alkali halides (section 1.1). This mechanism has been extensively treated in the literature and we will focus on the review of Song and Williams [Song 1996] summarizing the most relevant aspects. We will discuss the most relevant works related to the recombination of defect centers in alkali halides (section 1.2). Finally, several works analyzing the role played by the impurity in Eu-doped alkali halides are summarized (section 1.3).

1.1 Defects formation in alkali halide crystals

The main defects formed during irradiation in alkali halides are F and H centers. In this section, the process of formation of these defects from free electrons and holes produced during irradiation is described. The process of formation goes through several steps of which one of them is the formation of trapped excitons. The process of self-trapping is described in section 1.1.1. Section 1.1.2 deals with the properties of the STE in alkali halides. Finally, in section 1.1.3 the formation of F and H centers from STE is discussed.

1.1.1 General theory of self-trapping of excitons in alkali halides

An exciton is the lowest excited state of a crystal in which the excited electron and the hole remain spatially correlated. The correlation of the pair results in a set of discrete binding energy states at lower energy than those of the free electron–hole pair. These discrete states are responsible for the strong absorption lines observed just below the direct band gap. The radiative annihilation of the exciton could be induced by photon absorption in one of the exciton lines. The same luminescence emission could be produced by band-to-band excitation followed by electron–hole pairing into the exciton state.

The theories about excitons consider the correlation of the electron–hole pair in an excited crystal where the ions remain rigidly at their perfect lattice sites. When this simplification is relaxed, the lattice would be deformed by the presence of the exciton leading in same cases to a self-trapping process.

In general, a charge carrier in a deformable lattice creates an attractive potential well in which it is momentarily trapped. The time scale of such trapping can vary in a wide range, as can the spatial localization of the lattice deformation, depending on the strength and the type of electron–lattice interaction. The continuum model developed by Toyozawa predicts that the adiabatic potential energy of an electron in a deformable lattice (elastic and dielectric deformation) presents two types of minima as a function of the localization radius of the electron: a [Toyozawa 1983]. The first minimum at $a_F > a_0$, with a_0 the lattice constant, represents a nearly free state F characterized by moderate polarization of the lattice and the second minimum at $a_F = a_0$ represents a completely localized state S (self-trapped) with strong

dilatation as well as strong polarization of the lattice. In Fig. 1.1, the phase diagram to the different states is plotted in the coordinate space of the two normalized electron–phonon coupling constants, g_l and g_s, which are the optical and the acoustic contribution to the lattice relaxation energy normalized by the kinetic energy of the electron, respectively. The different phases are F (free, single minimum), S (self-trapped, single minimum), $F(S)$ (free with a higher metastable S minimum) and $S(F)$ (self-trapped with a higher metastable F minimum). The criterion of whether the F or S state is metastable with respect to the other is given by the relative depths of the two minima which depend of the magnitude of g_s. The (g_s, g_l) coordinates of electrons and holes in a number of materials are shown in the diagram, indicating the nature of the respective carriers.

In alkali halides the electrons remain free in the crystal but the holes are self-trapped immediately after their formation. The hole is localized on an halide ion which then forms a covalent bond with one of the halide neighbors, resulting in a X_2^- molecule ion within the crystal (X^- represents a halide ion). As long as the electrons are trapped elsewhere, self-trapped holes are stables at temperatures low enough to allow their migration. As a result, their

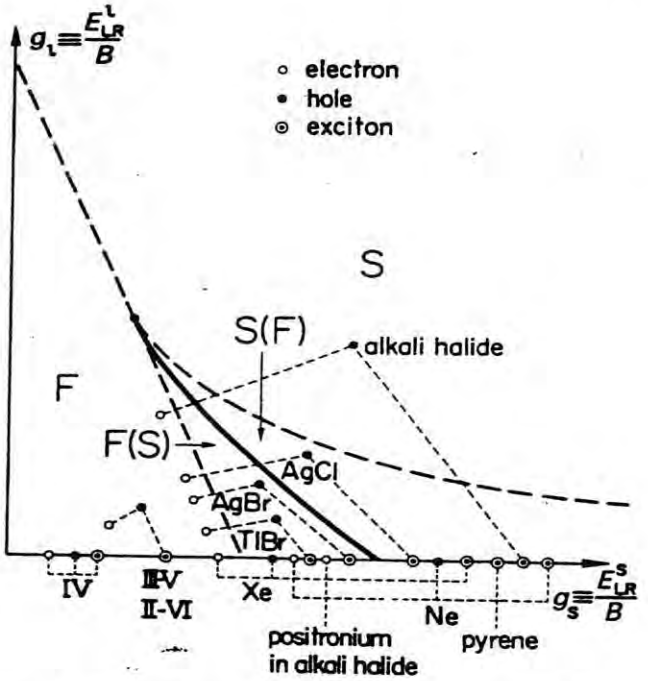

Fig. 1.1. Phase diagram showing stability of free (F) and self-trapped (S) carriers in the g_l–g_s plane. The (g_l–g_s) coordinates for electrons, holes, and excitons in several materials are noted [Fig. 1 in Toyozawa 1983].

structure has been well studied receiving the name of V_k centers.

An exciton is electrically neutral and some differences between self-trapping of excitons and of charge carriers could be expected. In first order approximation, the internal coordinates of the exciton can be neglected and considered as a single neutral particle with $g_l = 0$. Such case comprises points on the g_s axis of Fig. 1.1. The metastable self-trapping of the excitons occurs for any $g_s > 2/3$ and the stable self-trapping for $g_s > 1$. The presence of the barrier between free and self-trapped exciton states (STEs) allows that both states coexist as evidenced by the coexistence of two intrinsic luminescence bands: one very narrow with little Stokes shift due to the free excitons, and the other broad and strongly Stokes-shifted due to the STEs.

1.1.2 STEs in alkali halides

STEs have been extensively studied in alkali halides. They were the first materials in which self-trapping was predicted and amongst the first one in which STE was observed. Initially the STE was considered as an electron bound to a V_k center, being the on-center model. However, there is actually enough evidence showing that the electron is more than a passive bound charge. The interaction of hole and electron together with the deformable lattice produces a relaxed configuration of the pair which could be quite different to the V_k center.

The theoretical studies of the configuration of the STE are based on finding the equilibrium structure by minimizing the total energy of the lattice containing the STE. The simulation results imply that there is a strong instability in the on-center configuration and the V_k core undergoes an axial translation along a <110> direction. At the same time the excited electron charge density concentrates on the nascent anion vacancy after the V_k core shifts to one side. Therefore, the electron and hole charge density of the STE split in space and the resulting structure of the STE is more like a primitive F–H pair, being the off-center configuration (Fig. 1.2).

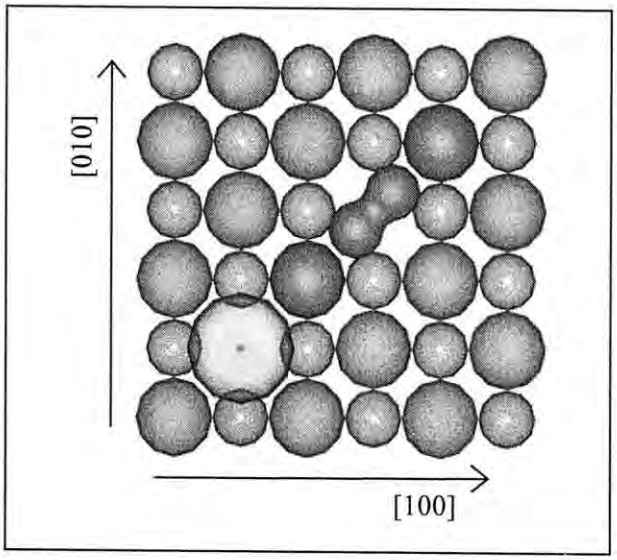

Fig. 1.2. Representation of the F–H pair in alkali halides with the NaCl-type structure. Blue and brown spheres represent the alkali and the halide ions, respectively. The green sphere represents the electron charge density (around the halide vacancy) and the yellow spheres represent the H center: a Cl_2^- molecule in a halide position and associated with two neighbors halide ions along a <110> direction.

Experimental studies have revealed that more than one STE configuration is possible, each one responsible of a different luminescence emission. In all alkali halides subjected to band-gap excitation there is a long-lived, highly Stokes-shifted luminescence band polarized perpendicular (π) to the major axis of the V_k center originating from a triplet state of the STE. In about half of the alkali halides, there is also a short-lived, significantly less Stoke-shifted band polarized parallel (σ) to the V_k associated to a singlet state of the STE. In a few alkali halides (RbI is the clearest example) there is a third STE luminescence band (E_x) located between the σ and the π band [Song 1996, pg. 146 and references therein].

The positions of the STE luminescence bands of nine alkali halides shown in Fig 1.3, suggests the classification of the STE emissions in three different type of bands labeled as I, II, and III in order of increasing Stokes shift. Each luminescence band has been associated to a different degree of off-center relaxation of the halogen pair as follows. The type I band (σ-band) is observed for crystals with larger halide ions, in which off-center motion of the halogen molecular ion core is most constrained and therefore it was attributed to the $V_k + e$ configuration (on-center). Detailed theoretical calculations have shown that even in such crystals there is a small off-center relaxation of the V_k core, as well as of the surrounding ions

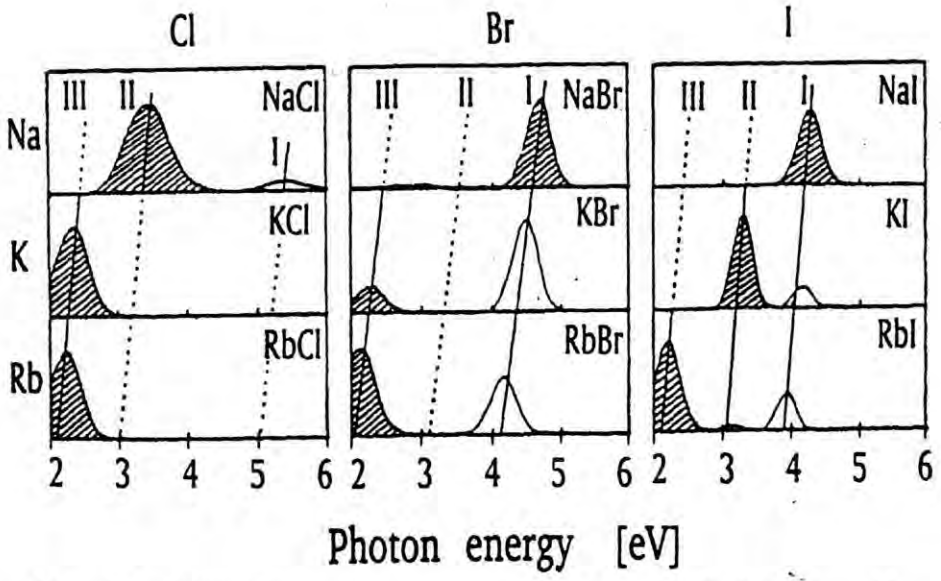

Fig. 1.3. STE luminescence spectra of nine alkali halides, with predominantly triplet bands shaded and predominantly singlet bands not shaded. Apparent correlations among luminescence bands within a given halide family are indicated by lines labeled I, II, or III. A dotted line means that anticipated luminescence bands are missing [Fig. 5.17 in Song 1996].

and, therefore, the type I STE could be described as "nearly on-center". Because of the extreme Stokes shift of band III (π-band), a substantial extra lattice relaxation in addition to the V_k distortion is expected. This band was attributed to off-center STEs with a configuration close to the nearest neighbor F–H pair. Finally, the type II band (E_x band) is associated to an intermediate degree of off-center relaxation.

Kayanuma suggested schematic configuration coordinate diagrams to account for the singlet and triplet STE emission in crystals such as KCl, KBr, and RbBr (Fig. 1.4a) and in crystals such as NaI and NaBr (Fig. 1.4b) [Kayanuma 1989]. The configurational diagrams correspond to a section in the Q_1–Q_2 space (coordinate Q_1 related to the breathing mode of the dihalide molecule and Q_2 to the translational mode) at $Q_1 \neq 0$.

In Fig. 1.4a, the triplet STE potential surface is adiabatically unstable at $Q_2 = 0$. The singlet adiabatic potential surface (APS) associated with the same orbital state as the triplet is stable within a shallow minimum about $Q_2 = 0$, and this is the origin of the σ luminescence (type I). In KCl and RbCl, where no type I luminescence is observed, it was concluded that the adiabatic instability is strong that not even the singlet surface has a local minimum at $Q_2 = 0$.

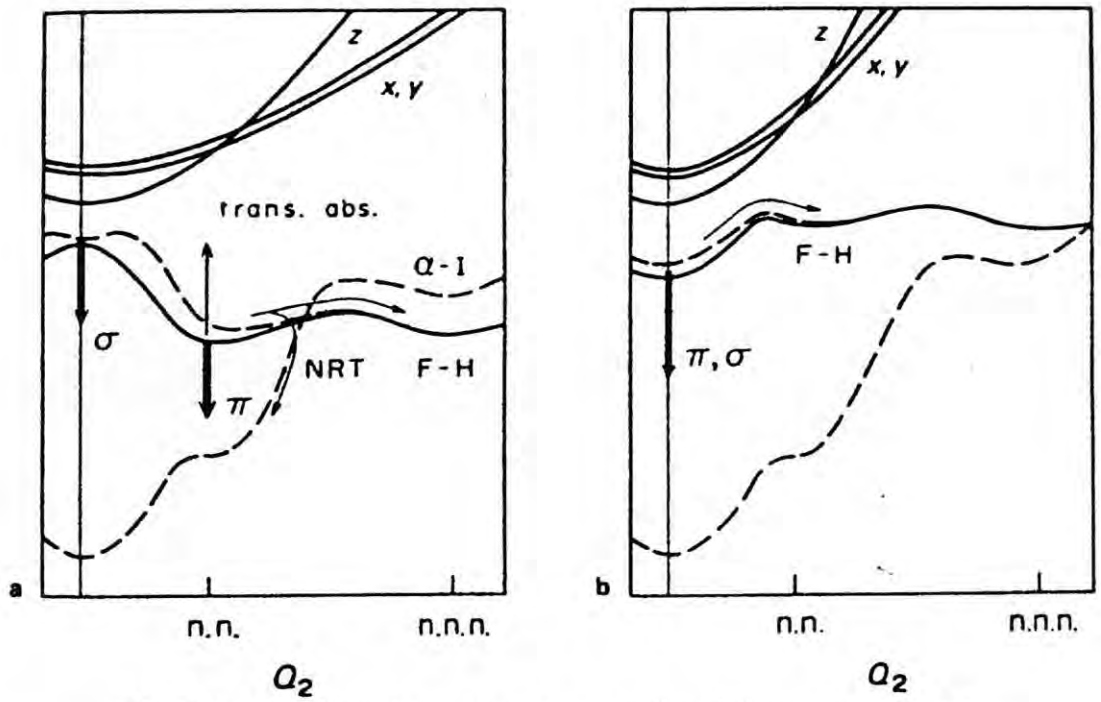

Fig. 1.4. (a) Schematic configuration coordinate diagram proposed for triplet (solid lines) and singlet (dashed lines) states of the STE / F–H system for KBr and RbBr. The optical transitions for σ and π luminescence are denoted by vertical arrows. The adiabatic potential surfaces for KCl and RbCl are essentially the same as shown here except that the on-center point of the singlet surface is presumed unstable. **(b)** Similar configuration coordinate diagram for the STE states in NaBr and NaI [Figs. 11 and 13 in Kayanuma 1989].

In NaI and NaBr, the halogen molecular ion is larger with respect to the lattice spacing and is thus difficult to displace off-center along Q_2. Kayanuma proposed (Fig. 1.4b) that in NaI and NaBr there is a minimum in both the singlet and triplet APS at $Q_2 = 0$. In fact, in these cases both singlet and triplet components are observed in the type I band.

Finally, it was experimentally observed that the interband excitation produces σ and π luminescence but the excitation to the exciton band produces only the π luminescence [Ikezawa 1969]. This result was justified by Kayanuma as follows: (*i*) in the interband excitation, the primary products are a free electron and a free hole. The hole is instantly self-trapped to form a V_k-center without potential barrier and then the electron is captured and cascades down to the lowest on-center STE state (Fig. 1.5); (*ii*) in the case of excitation in the exciton band, the free exciton undergoes a tunneling through the potential barrier to the self-trapped state in the translational mode (Q_2). In the Q_1–Q_2 space, the tunneling will take

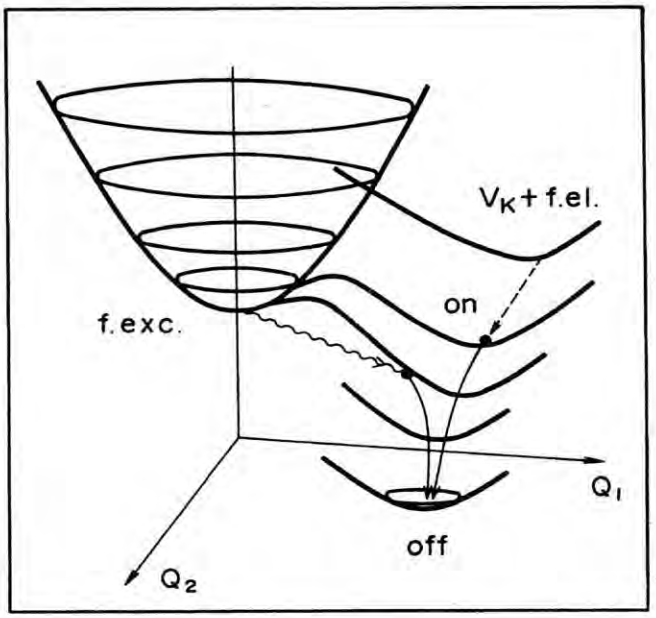

Fig. 1.5. Two relaxation paths to the off-center minimum point of the STE. The wavy line and the dashed line represent the tunneling and the cascade relaxation, respectively [Fig.12 in Kayanuma 1989].

directly to some off-center position of the APS without passing the on-center configuration since the lowest potential barrier is located at the direction $Q_2 \neq 0$ [Kayanuma 1989].

1.1.3 Defect formation in alkali halides

In the previous section, it was pointed out that the equilibrium configuration of the STE in alkali halide crystals is almost like a nearest neighbor F–H defect pair. Table 1.1 compares r_0, a measure of the extent of the F-center wave function, to d_{FH}, the calculated F–H pair separation in a STE configuration for several alkali halides. This table evidences that no large or violent transformation is needed to convert a relaxed STE to a really separated F–H pair.

In order to form F centers and H centers that survive beyond the STE radiative decay time, some of the F–H pairs must acquire larger mutual separation. To be specific, their separation should be such that the F center electron wave function has negligible overlap with the hole on the H center. Then, the discussion of F–H defect pair formation in alkali halides is focused on how the additional separation of the F and H centers relative to the STE

Crystal	d_{FH}	r_0	Crystal	d_{FH}	r_0
NaF	4.5	1.7	NaBr	2.5	2.2
KF	5.6	1.8	KBr	6.2	2.3
RbF	4.3	1.9	RbBr	7.2	2.3
NaCl	3.0	2.1	NaI	3.0	2.3
KCl	6.5	2.2	KI	3.0	2.4
RbCl	6.6	2.2	RbI	4.0	2.5

Table 1.1. Calculated distance d_{FH} (in Å) between the excited electron on the anion vacancy site and the center of the H center in the off-center triplet STE. The distance d_{FH} should be compared to the parameter r_0 (in Å) which is a measure of the extent of the F-center wave function [Table 6.1 in Song 1996].

configuration comes about. The energy required to convert an STE to a stable F center and H center is comparable to the energy of H-center diffusion in many alkali halides (75 meV in KCl), thus is presumable that the H center moves thermally from the STE site to form separated defects.

The temperature dependence of the formation of stable F centers and the quenching of the π-luminescence presents two different relationships which divide the alkali halides in two categories (Fig. 1.6). In the first one, which includes KI, RbI, NaBr, NaCl, LiBr and LiCl, the rate of luminescence decay anti-correlates with the rate of conversion to F–H pairs (Fig. 1.6a). In the other group, which includes KCl, KBr and RbBr, the STE luminescence quenches before the onset of temperature-dependent production of F–H defect pairs and furthermore there is a significant production of defects even at very low temperature (Fig. 1.6b).

In general, the probability of conversion of a STE to an F–H defect pair increases with temperature. In alkali halides which have minimal defect formation probability at low temperature, the STE luminescence and the conversion to F–H pairs are competitive channels for the STE decay (Fig. 1.6a). This result evidences that STE and F–H defect pairs of all separation lie on the same APS, representing the lowest electronic excited state of the crystal. Then, the thermal conversion from STE to the F–H defect pairs takes place entirely on the ESF surface.

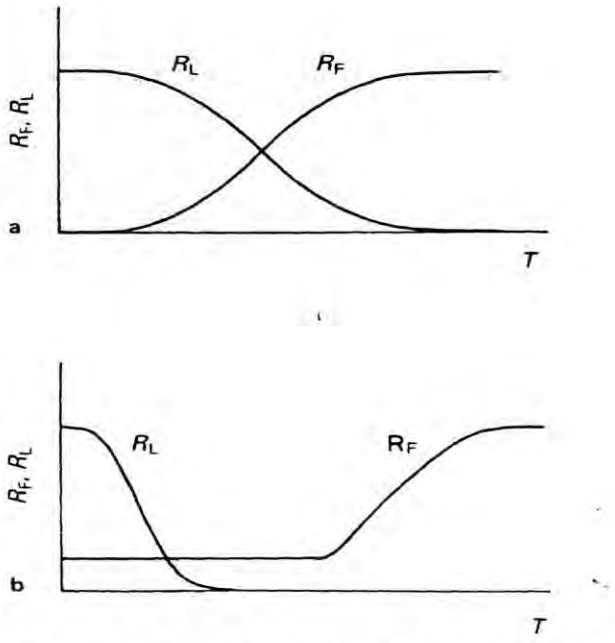

Fig. 1.6a, b. Schematic diagram illustrating the temperature dependence of the intensity of the π-polarized STE luminescence (~ R_L) and of the primary yield of F centers (~ R_F) for two categories into which alkali halides are generally found to divide [Fig. 6.5 in Song 1996.]

At temperatures below about 40 K, the H center becomes immobile on the scale of the STE lifetime, and it is generally observed that the thermally activated channel of defect formation is closed. However several alkali halides exhibit significant F–H pair production efficiency when irradiated at temperatures as low as 4.2 K (Fig. 1.6b). The H-center displacement in that case must occur out of thermal equilibrium with the lattice. This process has been termed the "dynamic process" of F–H pair production. It was suggested that the key of the dynamic conversion should be the effectiveness to use the stored energy of the STE to displace the H center over barriers that are comparable to those deduced from thermal activation. In Fig. 1.7 the alkali halides which exhibit the dynamic conversion process have been catalogued by the calculated relaxation of the off-center STE configuration. The potential energy drop associated with the relaxation of the surrounding ions is denoted by ΔE_1, while the energy drop associated with off-center motion of the X_2^- core toward the F–H pair is denoted ΔE_2. Then, the energy ΔE_1 is mostly wasted on relaxation of surrounding ions and the energy ΔE_2 should be convertible to kinetic energy of motion toward larger F–H

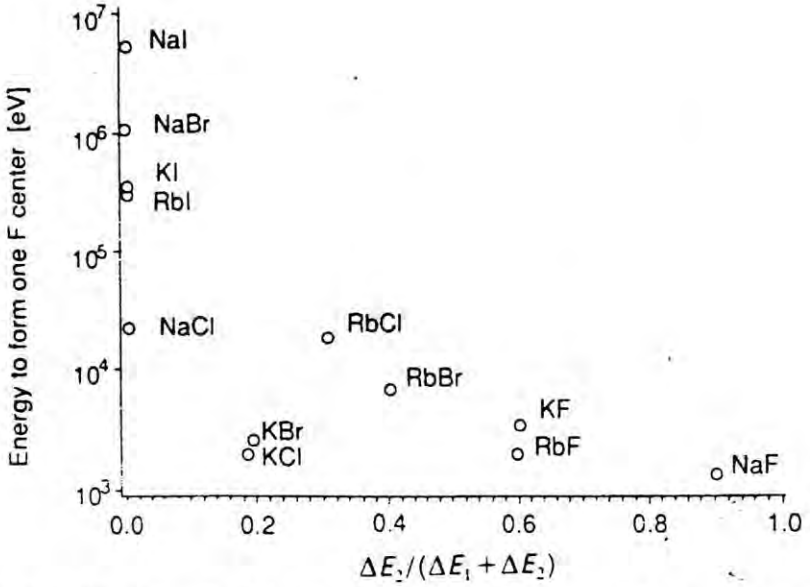

Fig. 1.7. The energy of the incident radiation per stable F center formed versus $\Delta E_2/(\Delta E_1+\Delta E_2)$, where ΔE_1 is the energy wasted in the relaxation of the surrounding atoms, and ΔE_2 is the energy used to the displacement of the X_2^- core toward larger F–H separation [Fig. 6.13 in Song 1996].

separation. Fig. 1.7 clearly shows that the ratio $\Delta E_2/(\Delta E_1+\Delta E_2)$ tends toward larger values in crystals that exhibit F-center formation at low temperatures.

Finally, the time-scale for the defect formation in alkali halide crystals was experimentally estimated by F-center absorption after excitation with amplified dye laser pulses of duration 1.8 ps in a KBr crystal at RT. The experimental data show a 2 ps rapid rise which was attributed to dynamic conversion and a 50 ps slower rise attributed to thermal conversion at RT.

1.2 Defect recombination in alkali halides

Nowadays it is commonly accepted that F–H pairs are the primary products of the electronic excitation of alkali halides. The secondary products due to the motion of F and/or H defects are generally defects trapped at impurity centers present in the crystal or complex aggregated defect centers. At low temperatures, where the F and H centers are immobile, the formation of other defects like α–I centers was also observed. This is due to the tunneling of the excited electron from an F center to an H center which was theoretically demonstrated to be non-radiative [Shluger 1981]. In general, the kinetic of the F–H recombination could be discussed in terms of two mechanisms: electron tunneling and H center migration. In some circumstances the F–H recombination results in the emission of the STE luminescence as was experimentally observed.

1.2.1 Kinetic of the F–H center pair recombination

The kinetic of the recombination of F–H center pairs was studied by thermal annealing experiments where the optical absorption intensity associated to each defect is followed at increasing temperatures. In this way, it was established that in X-irradiated KCl crystals at low temperature, F and H centers present simultaneous annealing steps at around 36 and 49 K [Behr 1967]. The first step was found to be of first order and was attributed to the recombination of correlated F–H pairs. The second step was not first order and was attributed to the recombination of uncorrelated F–H pairs. There is a controversy in the assignment of the peak at 36 K which was also attributed to recombination of F centers with V_k centers not with H centers [Purdy 1975]. Other authors reports annealing steps at 35, 42, 47 and 52 K [Lushchik 1992].

The multi-step structure of the thermal annealing experiments were analyzed according to two mechanisms: (1) the tunneling transfer of an electron from the F center to the H center, and (2) the H center diffusion to the neighborhood of the F center [Kotomin 1994]. At temperatures below the delocalization temperature of H centers (T_d), the tunneling recombination is the predominant mechanism. As the temperature exceeds T_d, this tunneling is

accelerated by H center diffusion. Lastly, at temperatures high enough diffusion becomes so fast that H centers approach their complementary F centers before an electron tunneling occurs, and annihilate with them restoring the perfect crystalline lattice.

Both static tunneling recombination and diffusion annihilation depend on the relative distance between partners, via the exponential change of the overlap of the wavefunction of F and H centers in the former case and the number of hops necessary for their encounter in the latter case. At their birth, F and H centers are spatially correlated and their relative distances hardly exceed several nearest neighbors (NNs). This conclusion is supported by molecular dynamic simulations and theoretical studies of the temperature dependence of F center accumulation [Kotomin 1994 and references therein].

The theoretical study of the diffusion-controlled annihilation of F–H center pairs not further than third/fourth nearest neighbors allowed to fit the experimental data of the multi-step structure of F center annealing. However, quantum mechanical calculations of the F–H tunneling recombination in KCl, yield the values of parameters $W_0 = 10^{13}\ s^{-1}$ and a = 0.5 Å defining the tunneling probability per unit time to be $W(r) = W_0 \exp(-r/a)$, where r is the relative distance between defects. From here, the tunneling lifetime for the three first F–H NNs oriented along the <110> axis was estimated as $\approx 1 ns$, $\approx 1 \mu s$ and $\approx 1 ms$, respectively [Kotomin 1994]. Therefore, the F–H pairs involved in the annealing steps are expected to be destroyed by the tunneling recombination at much shorter times (μs-ms) than that involved in the annealing experiments (minutes time scale). This dilemma was not resolved but it was argued that the multi-stage annealing could originate either from a set of secondary reactions between defects rather than their correlated annealing or from a portion of close F–H centers whose tunneling recombination is prohibited at short relative distances (several NNs) due to their parallel spin orientation remained after the STE structure decay into F–H pairs [Kotomin 1994].

1.2.2 STE luminescence in the F–H recombination

The simultaneous study of thermal bleaching of defects and of thermoluminescence (TL) in KCl crystals irradiated at around liquid Helium temperature allows to associate the observed low temperature glow peaks with the annealing steps mentioned above [Purdy 1975]. The TL emission of the 49 K peak included a band around 2.32 eV which corresponds with the π-emission of the STE. Therefore, the TL recombination could be considered as the "reverse reaction" of the F–H defect creation.

In the TL emission of a X-irradiated KBr crystal the peak at around 30 K presents the σ and the π-luminescence emission of the STE [Tanimura 1974, 1980]. In that work, a detailed study of the quantitative correlation between the amount on the decayed H and F centers and the TL intensity of both emission bands was reported. When the emission originates from F–H recombination, it is expected that the maximum TL intensity should be proportional to the decrement of F and H centers. However, it was found that the σ-emission intensity does not follow a linear correlation with the amount of decayed F and H centers and that the π-emission can be separated in two components, one of them showing the same dependence as the σ-emission and the other showing the expected linearity. Then it was concluded that the recombination between F–H pairs in KBr results only in the π-emission. The σ-emission and a component of the π-emission observed in the TL recombination are due to some indirect reaction of the H center and/or to a reaction of other defects which occurs at a similar temperature.

1.3 Role played by the impurity in Eu-doped alkali halides

Absorption and emission spectra of the Europium ions in alkali halide crystals have been extensively studied and the electronic energy level diagram is well known. Absorption and emission spectra are quite sensitive to the surrounding state of the Eu-impurity in the alkali halide matrix and provides a method to evaluate the participation of the different aggregates in luminescence experiments. In this way, the participation of the Eu impurity in the formation of stable F centers and also in the AG and TL phenomena in Eu-doped alkali halide crystals have been studied. The different proposed models could be classified into two groups. In the first group it is considered that the impurity changes its valence state and participates directly as a member of the defect pair during the formation of stable F centers and the recombination in the AG and TL phenomena. In the second group of models, the impurity plays a passive role working as a trap of some of the primary defects and receiving the energy of the recombination during the AG and TL phenomena.

1.3.1 The Europium ion

The Europium is a rare earth ion which usually appears in a crystal in the divalent state. Its electronic configuration is given by $4f^7 5s^2 5p^6$ with the $4f$ electrons shielded by two external electronic shells [Rubio 1991]. When the Eu^{2+} ion is introduced in an alkali halide crystal, it usually enters substitutionally for the alkali cation forming a dipole with a cation vacancy, the latter created to preserve the overall charge neutrality. The impurity-vacancy axis lies along a <110> direction of the alkali halide lattice. The site occupied by the Eu^{2+} ion has been determined to be mainly of a cubic nature with a sixfold coordination besides the presence of the neighboring compensating vacancy (Fig. 1.8). In the ground state of the Eu^{2+} ion there are seven $4f$ electrons. The lowest lying excited states are formed either by states within the $4f^7$ configuration or from states within the $4f^6 5d$ configuration. In the latter configuration, the six f electrons independently give rise to seven levels. The five-fold

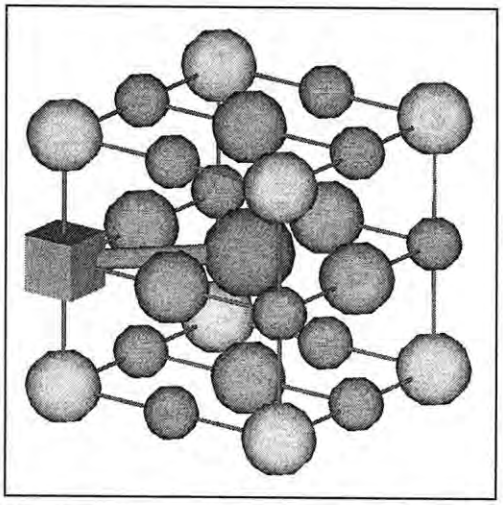

Fig. 1.8. Unit cell of an alkali halide crystal with the NaCl-type structure including an Eu^{2+} impurity ion. The Eu^{2+} ion (violet sphere) has six halide ions (orange spheres) as first neighbors at a distance a/2 in the <100> directions, and twelve alkali ions (blue spheres) as second neighbors at $\sqrt{2}a/2$ in the <110> directions. The Eu^{2+} ion is associated with a vacancy (violet cube) in a <110> direction.

degeneracy of the $5d$ level is split by the cubic crystal field into a doubly-degenerate (E_g) and a threefold degenerate (T_{2g}) energy level. In the sixfold coordination the E_g level is situated at higher energy respect to the T_{2g} one and the separation between them is known as the $10Dq$

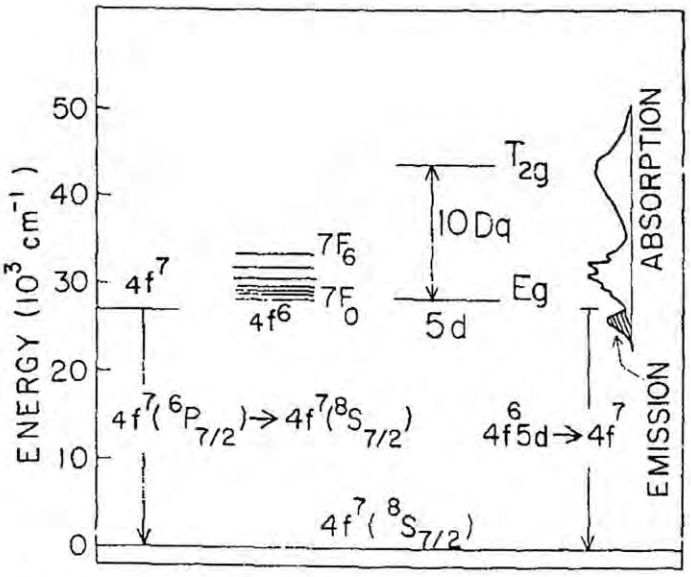

Fig. 1.9. Schematic energy level diagram of the Eu^{2+} ion in a crystalline solid [Fig. 3 in Rubio 1991].

splitting. In the present case, the interaction of the $4f^6$ electron with the $5d$ electron is rather weak and the composite $4f^6 5d$ system retains much of the nature of the uncoupled $4f^6$ and $5d$ levels. Fig. 1.9 shows the energy level diagram.

The absorption spectrum of the Eu impurity is characterized by two broad bands associated to transitions from the ground state to the E_g and T_{2g} states of $4f^6 5d$. Superimposed on the low energy E_g absorption band appears seven narrow bands which evidences the character of the $4f^6$ levels. The emission from the Eu^{2+} ion can be excited by light lying in either of the two broad bands and it is associated with a transition from the excited states of $4f^6 5d$ to the ground state. The emission peak position depends strongly on the type of the host crystal in which the Eu impurity has been incorporated as shown in Table 1.2).

	Centre of gravity of the high-energy absorption band		**Centre of gravity of the low-energy absorption band**		**Peak position of the emission band**			**Stokes shift**	**Life-time**
Host	**(nm)**	**(cm^{-1})**	**(nm)**	**(cm^{-1})**	**(nm)**	**(cm^{-1})**	**10 *Dq* (cm^{-1})**	**(cm^{-1})**	**μs**
NaF	204	49,020	326	30,675	422	23,697	18,345	6978	--
KF	214	46,729	332	30,120	427	23,419	16,609	6701	--
NaCl	240	41,667	347	28,818	427	23,419	12,849	5399	1.08
KCl	243	41,152	343	29,155	419	23,866	11,997	5289	1.20
RbCl	244	40,984	341	29,326	417	23,981	11,658	5345	1.14
NbBr	249	40,161	352	28,409	428	23,364	11,752	5045	1.03
KBr	250	40,000	344	29,070	418	23,923	10,930	5147	1.33
RbBr	252	39,683	340	29,412	416	24,038	10,271	5374	1.02
NaI	261	38,314	361	27,701	439	22,779	10,613	4922	--
KI	262	38,168	349	28,653	427	23,419	9,515	5344	1.23
RbI	262	37,879	347	28,818	426	23,474	9,061	5344	--

Table 1.2. Values for the peak position of the centre of gravity of the broad absorption bands as well as for the emission of the Eu^{2+} in alkali halides at 300 K. Values for the 10 *Dq* splitting, the Stoke shifts and the lifetime are also included [Rubio 1991 and references therein].

1.3.2 Precipitation of the Eu-impurities

Eu-doped alkali halide crystals submitted to several thermal treatments shows different absorption and luminescence spectra which could be associated to several aggregation states of the Eu^{2+} impurity [Lopez 1980, Rubio 1981]. The thermal treatments giving rise to different precipitated phases in KCl:Eu crystals will be detailed below.

The treatment of a crystal at temperatures around 500°C dissolves the impurity in the Eu^{2+}-v_c dipoles (Fig. 1.8). Annealing periods from 0.5 to 2 h are enough to obtain the maximum concentration of dipoles. After heating, a fast quenching from high temperature assures a minimal formation of precipitates. Following this treatment, a KCl:Eu crystal presents an absorption spectrum at RT formed by two broad bands centered at 240 nm and 343 nm, the latter one with a staircase structure to higher wavelength. The emission spectrum is composed of a single band centered at 419 nm and width of 0.15 eV.

A KCl:Eu sample stored for several years at RT without any other thermal treatment presents a slightly different absorption spectra with the high-energy band centered around 244 nm and the lower one displaced to 349 nm. The higher separation between the bands indicates that the crystal field at the site occupied by the impurity is stronger than at the dipole configuration. The emission spectra is also altered changing to a single peak centered at 427 nm and width of 0.17 eV. When the well-aged sample is quenched at increasing temperatures for fix periods, the 427 nm emission band disappears in benefit of the 419 nm band in a narrow range of temperatures around 90 – 150°C. This result was previously described to the dissolution of the Suzuki phase similar to that of Cd^{2+} and Sr^{2+} in NaCl [Garcia 1980], and suggests the assignation of the 427 nm band with this precipitated phase. The Suzuki phase is characterized by a super unit cell eight times greater than that of the host given by an arrangement of impurity divalent cations and cation vacancies as shown in Fig. 1.10.

The aging of a KCl:Eu crystal at 200°C also alters the absorption spectra: the high energy band is centered at 262 nm and the low energy band at 349 nm. In this case, the $10Dq$ splitting is lower than that of the quenched sample and that of the well RT-aged one indicating that in each treatment different precipitated phases are involved. The emission spectrum show

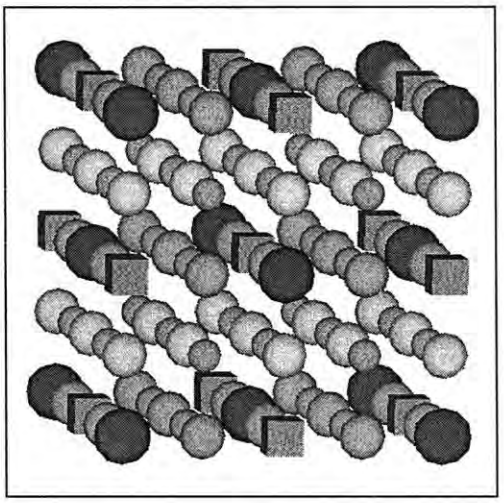

Fig. 1.10. Suzuki precipitate unit cell. Orange and brown spheres represent the halide ions in different layers. Blue and cyan spheres represent the alkali ions. Violet spheres and cubes represent the divalent cation impurities and the cation vacancies, respectively. The stoichoimetry of the Suzuki phase for KCl:Eu would be $EuCl_2$:$(KCl)_6$ [Suzuki 1961].

a more complex structure composed of the previous 419 nm band and three new bands centered at 478 nm, 439 nm and 410 nm. The latter band appears after 200 h of annealing. In view of the similarities of the 439 nm and 478 nm band with similar well-identified bands in the NaCl:Eu crystal, these bands were assigned to the precipitation in two dimensions $EuCl_2$ metastable structures (Fig. 1.11). The 410 nm band was assigned to the stable dihalide $EuCl_2$ due to the correlation with the emission observed in $EuCl_2$ samples.

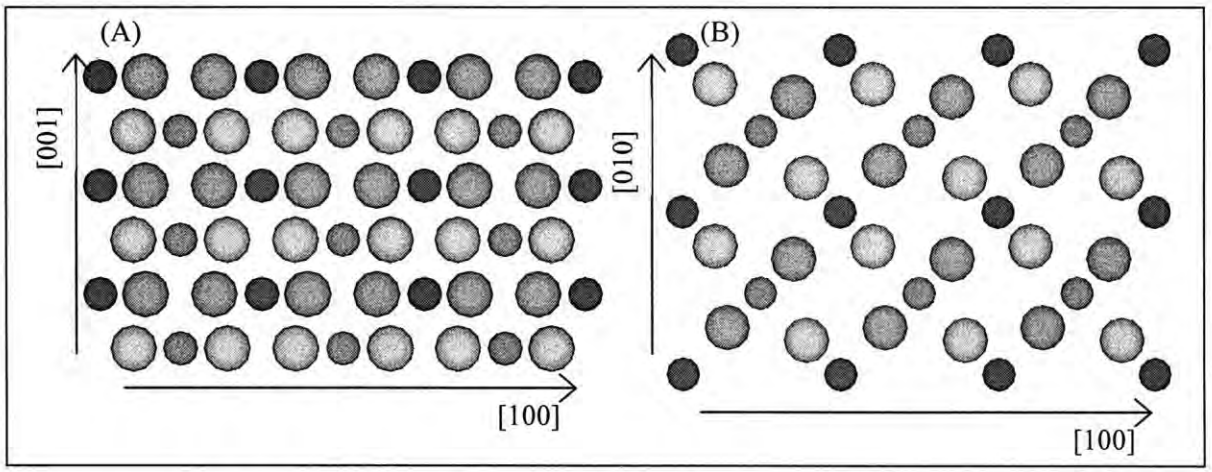

Fig. 1.11. $EuCl_2$ structure. Orange and brown spheres represent the halide ions in alternative layers. Violet spheres represent the Eu^{2+} ions. (A) (010) projection; (B) (001) projection [Suzuki 1955].

1.3.3 Participation of the Eu impurities in the formation of stable radiation defects

Optical absorption, electron paramagnetic resonance (EPR) and ionic thermal current (ITC) studies revealed that the exposition to ionizing radiation of a quenched Eu-doped alkali halide reduces the concentration of Eu^{2+}-v_c dipoles [Chowdari 1971, Kao 1979, Opyrchal 1989]. However, the results and the conclusions reported by the different authors are, in some aspects, contradictories. In general, three independent mechanisms have been proposed: (*i*) radiation-induced aggregation, (*ii*) impurity-ion conversion, and (*iii*) participation in the F-center production.

The presence or not of the different mechanism seems to be related to the concentration of Eu in the alkali halide lattice and the ionizing radiation dose. Radiation-induced aggregation was clearly observed in crystals with high concentration of Eu impurity, being dimers (association of two dipoles) the first product of aggregation [Muñoz 1985]. Impurity ion conversion to the tripositive state (Eu^{3+}) by trapping a hole released by irradiation was only detected after extreme irradiation doses. Furthermore, it was concluded that this process is more efficient in those crystals where the Eu impurity appears as $EuCl_2$ precipitates instead of Eu^{2+}-v_c dipoles [Aguilar 1982].

The participation of the Eu impurity in the F center production is generally accepted. It was observed that the exposition to ionizing radiation decreases the Eu absorption band and increases the F center band. Contradictorily, some authors observed that the Eu^{2+} intensity is partially recovered by illumination in the F-center absorption band [Chowdari 1971, Aguilar 1982], while others assured that the Eu intensity could not be recovery after any optical or thermal annealing [Opyrchal 1986]. In general, it was observed that the concentration of created F centers increases monotonically with the concentration of Eu-impurities, being more efficient when the impurities appear as Eu-v_c dipoles or forming the Suzuki phase than when the impurity appear as $EuCl_2$ precipitates [Rubio 1982].

Three mechanisms were proposed to explain the enhancement of the F center production by the introduction of divalent cation impurities in alkali halides: (*i*) inhibition of the F–H recombination, due to the trapping of the H center by the dipole impurity or by dipole aggregates; (*ii*) generation of new F–H center pairs near the dipole impurity or dipole

aggregates and (*iii*) participation of the impurity as electron- or hole-trap being involved directly in the defect formation.

The trapping of H centers by the Eu impurity (mechanism *i*) was confirmed in X-irradiated crystals at low temperature, where the 340 nm absorption band associated to H centers close to divalent impurities (called H-N centers) has been observed [Chowdari 1971]. Mechanism (*ii*) could explain the presence of F_Z centers (F centers trapped at divalent impurities) because of the generation of F–H pairs close to the impurities followed by the migration of the H centers and their subsequent trapping in some traps. F_Z centers have not been immediately observed in Eu-doped alkali halides exposed to ionizing radiation but following F-light bleaching. However, F_Z centers were effectively created after exposed the Eu-doped alkali halides to non-ionizing UV-light [Aceves 1994]. Finally, mechanism (*iii*) has been successfully used to explain the defect formation in crystals such as KCl:Ag and KCl:Tl where it is known that the impurity changes its valence state [Delbecq 1974]. As it was mentioned above, this mechanism is not probable to occur in Eu-doped alkali halides under non-extreme irradiation conditions.

Actually, it is accepted that mechanism (*i*) explain the enhancement of the F center formation in Eu-doped alkali halides exposed to ionizing radiation: irradiation produces excitons in the perfect alkali halide lattice leading to F–H pairs, then the Eu impurities trap some of the H centers inhibiting the F–H recombination. The presence of F_Z centers in Eu-doped alkali halides under non-ionizing UV-light reveals that in this case, mechanism (*ii*) is working as we will discuss below.

1.3.4 Afterglow and thermoluminescence in Eu-doped alkali halides exposed to ionizing radiation

The photoexcitation of a previously irradiated europium-doped alkali halide crystal produces an afterglow (AG) and a thermoluminescence (TL) with the characteristic Eu emission. It has been proposed that the recombination occurs due to the electron from an F excited center which reaches a hole-trapped center. Two models appear at this point: (*i*) the Eu in the tripositive state acts by itself as the hole-trapped center and then the recombination energy is directly emitted as Eu luminescence during the Eu^{2+} de-excitation [Vassilev 1980] and (*ii*) the hole-trapped center is of the H or V_k -type and the recombination energy is in some way transferred to the Eu impurity which later emits its characteristic luminescence [Opyrchal 1979]. The first model seems most adequate to explain the participation of the Eu impurity in the recombination but there is no experimental evidence showing the presence of the impurity in the Eu^{3+} state. The second model justifies the presence of several TL glow peaks ascribed to different hole-trapped centers being the "low-temperature" one which participates in the AG process but this model does not explain the energy transferring mechanisms to the Eu impurity. Note that both models tend to the band structure approach. The second model, however, is easily translated to an approach based on the excitonic mechanism of defect formation.

In both cases, the decay of the AG was observed as a t^{-1} law after pulsed photoexcitation at low temperature [Opyrchal 1979, Vassilev 1980]. This decay was previously reported in KCl:Ag and KCl:Tl crystals due to the tunneling character of the transition between trapped charges and recombination centers [Delbecq 1974] differing in the pair of centers involved. Because AG decay plays an important role in this thesis, we included a detailed description of the tunneling process in Appendix 1.

1.3.5 Afterglow and thermoluminescence in Eu-doped alkali halides exposed to UV radiation

An afterglow luminescence was also observed in Eu-doped alkali halides which were not previously irradiated with ionizing radiation but exposed to UV light of wavelength higher than 200 nm. This low energy radiation does not produce photoionization of the crystal neither excitation of STE's. Therefore a radiation damage process and hence a mechanism involving color centers was not expected [Aguirre 1988]. The AG creation spectrum was observed as a single peak situated just below the high-energy absorption band of the Eu impurity independently of the alkali halide matrix. The AG emission spectra again correspond to the Eu^{2+} luminescence and decayed like a t^{-1} law (pulsed irradiation). These experimental results were explained by an initial process of ionization of the Eu^{2+} impurity. Then the ionized electron get trapped and the hole remained at the impurity site as Eu^{3+}. The AG decay was ascribed to the tunneling recombination of trapped electrons to the Eu^{3+} ions with the emission of the Eu^{2+} characteristic luminescence during de-excitation.

In a different model, it was assumed that at typical irradiation conditions the Eu^{2+} impurities do not act as electron traps neither as hole traps. Instead of that, STE are effectively created in the vicinity of the Eu impurity by the UV radiation [Babin 2003]. The excitation band for defect formation was assigned to an electron transfer process from the disturbed anion lattice around the Eu^{2+} impurity resulting in the formation of a V_k center in the vicinity of the Eu^{2+} and the ejection of an electron. The V_k-electron relaxation process results in the formation of a trapped exciton close to the impurity whose decay leads to the creation of an F–H center pair. In this model, the F–H center separation necessary for AG and TL was realized by the expulsion of the H center during the STE relaxation. The AG was associated to an electron tunneling mechanism in which the electron tunnels from the F center to the H center.

The latter model for the UV induced defect formation is formulated in terms of an adapted excitonic mechanism. A variant of this model is that UV irradiation immediately leads to an exciton trapped nearby the impurity without the emission of an electron. The final result of both models is the formation of F center nearly the impurity and the expulsion of an H center. In this thesis, the formation of an F center close to the impurity and a "free" H center during UV irradiation is taken as a starting point for discussing our results. For the afterglow,

we developed an alternative model that is not based on tunneling but on random migration of H centers. The development of this model is the topic of the next chapter.

CHAPTER 2:
A MODEL FOR THE AFTERGLOW RECOMBINATION KINETIC

Afterglow is the luminescent emission of a crystal which persists after irradiation. In general, the afterglow is due to those defect centers created during irradiation which are not immediately trapped forming stable defects but which "slowly" recombine exciting the luminescence emission. The study of the time dependency of the afterglow intensity could reveal the kinetic of the recombination mechanisms occurring immediately after irradiation. The term "afterglow" is reserved to the non-thermally processes resulting in the recombination of the products generated by the irradiation. However this luminescence is frequently overlapped with the luminescent emission due to the thermally retrapping of centers. The isothermal decay of the thermally stimulated luminescence follows an exponential law (first order) or a $1/t^2$ law (second order) and strongly depends on the temperature [Chen 1997].

In this thesis, we concentrate on the study of the afterglow produced in Eu-doped alkali halides after UV irradiation. In section 1.3.4 and 1.3.5 we mentioned a model for the afterglow based on tunneling. Here, we present an alternative model based on H center migration and show that a similar AG decay can be obtained without the necessity of tunneling. We develop an analytical approach of the afterglow decay time-dependency from a simple random walk problem in one dimension (section 2.2) [Alvarez-Garcia 2001]. Finally, we present a simulation analysis about the dependency of the AG decay with the probability of recombination (section 2.3) [Piters 2002].

2.1 Proposed model

We assume that UV irradiation of an Eu-doped alkali halide crystal at low temperature creates STEs in the vicinity of the Eu impurity (see section 1.3.4). Then the STE dissociates in an F–H pair by the well-known mechanism occurring in pure alkali halides (see section 1.1.3). We propose that the H center plays the role of the mobile charge. The afterglow would be explained by the F–H recombination due to not yet trapped H centers that after randomly migration return to the origin where they were created. The thermoluminescence would come from the release of H centers trapped at H center traps. At the origin, the H center recombines with the F center and transfers the excess of energy to the Eu impurity leading to the Eu^{2+} luminescence. The natural motion of the H centers in the bulk would be randomly in three dimensions, however, we propose that the H centers would move in one dimension. This model requires the presence of some linear guidelines and we propose that such lines would be dislocation lines (Fig. 2.1). Along dislocation lines the mobility could be much higher than in the bulk which would explain the presumed high mobility of H centers even at a temperature as low as 20 K at which the long-lasting AG luminescence has been observed. Strictly speaking, an H center in a dislocation line is no longer an H center, however, we will ignore this detail and simply denote it as an H center.

2.2 Analytical approach of the AG decay time-dependency

Suppose that at a time $t = \tau$ (with $\tau < 0$) a group of F–H pairs is created at the origin. The F centers remain there but the H centers would migrate along a line either forward or backward from site to site separated by a distance a. The effect of the origin is that when the H center arrives at that position, it recombines with the F center leading to the luminescence emission. We will neglect the presence of H center traps.

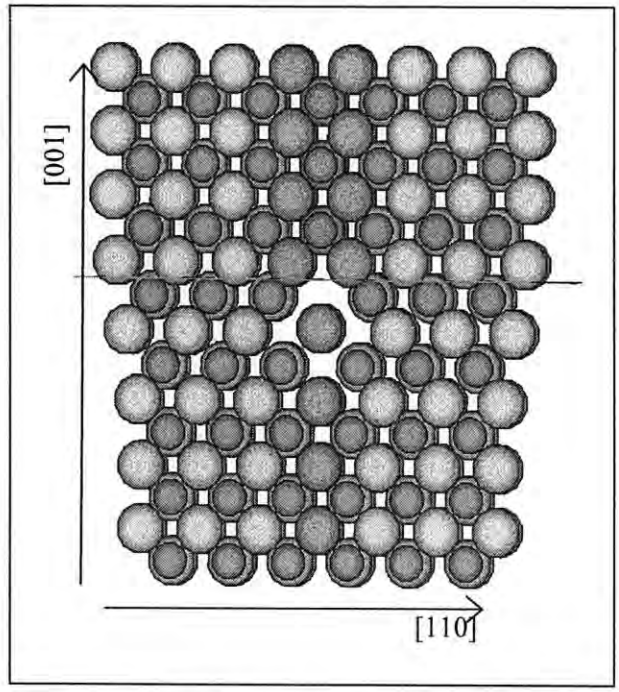

Fig. 2.1 (100) projection of an edge dislocation in a KCl crystal. The Burgers vector is along the [110] direction and the line of the dislocation is along [100]. The slip plane is $(1\bar{1}0)$ [Hirth 1968].

Suppose that the H centers have an initial energy which produces n_0 jumps along a forward direction away from the origin. After these n_0 jumps the forward and backward direction have the same probability. Neglecting the effect of recombination at the origin, the average position $< x >$ and the standard deviation σ of the net displacement of the H center after n jumps are given by a random walk problem:

$$< x > = a\, n_0 \qquad [2.1]$$

$$\sigma = \sqrt{a^2 n} \qquad [2.2]$$

To simplify the problem we assume that for a group of H centers created at the same time, their positions are in the interval 2σ. Further we assume that inside this interval, each site has the same probability to be occupied by an H center.

The increase of the deviation per jump is:

$$\Delta\sigma = \sqrt{a^2(n+1)} - \sqrt{a^2 n} = \sqrt{\sigma^2 + a^2} - \sigma \approx \frac{a^2}{2\sigma} \qquad \text{for } \sigma >> a\,. \qquad [2.3]$$

The number of jumps n may be represented by the time interval during which they occur: $t = n/\Gamma$, where Γ is the jumping frequency:

$$\Gamma = \Gamma_0 \exp(-E_m/kT) \qquad [2.4]$$

with $\Gamma_0 = 10^{12} - 10^{14} s^{-1}$ around the lattice vibrational frequency and $E_m = 0.03 - 0.13\, eV$ around the energy of H center diffusion in alkali halides.

For short time intervals Δt, the increase of the deviation $\Delta\sigma$ between t and $t + \Delta t$ can be written as:

$$\Delta\sigma(t) = \frac{a^2 \Gamma \Delta t}{2\sigma(t)}. \qquad [2.5]$$

We suppose that the group of H centers which were created at $t = \tau$, are at a distance $x_0 = an_0$ from the origin at time $t_0 + \tau$ and then the random migration starts. This supposition helps us to start up the development of the theory of AG decay but could be finally relaxed without altering the shape of the decay curve. The AG yield, however, is affected by relaxing this assumption as will be discussed in section 2.3.

Initially the width of the distribution grows like in eq. [2.3], but after $t > \tau + t_1$ with $t_1 = t_0 + x_0/(a\Gamma)$, some of the H centers reach the origin and recombine. In the interval $(t, t + \Delta t)$ with $t > \tau + t_1$, the fraction of centers that recombine and survive will be respectively:

$$R(t, t + \Delta t) = \frac{a^2 \Gamma}{2\sigma(t)} \Delta t \qquad [2.6]$$

$$S(t, t + \Delta t) = 2\sigma(t) + \frac{a^2 \Gamma}{2\sigma(t)} \Delta t \qquad [2.7]$$

So the expansion of the distribution of survived H centers takes place at one side of the distribution resulting in a displacement of the average position away from the origin (see Fig. 2.2). The increase of the deviation at the next Δt interval will be calculated with respect to this new average position and it is given by:

$$\Delta\sigma = \frac{a^2 \Gamma}{4\sigma(t)} \Delta t \qquad [2.8]$$

If the Δt interval could be considered as a differential, the eq. [2.8] can be integrated to obtain $\sigma(t)$:

$$\sigma(t)=\sqrt{\frac{a^2\Gamma}{2}(t-t_1-\tau)+{\sigma_0}^2} \qquad [2.9]$$

with ${\sigma_0}^2 = {x_0}^2$ the deviation at time $t \geq t_1+\tau$.

The probability that an H center created at $t=\tau$ recombines after Γdt jumps will be:

$$p_r(\tau,t)=\frac{R(t,t+dt)}{R(t,t+dt)+S(t,t+dt)}\approx\frac{a^2\,\Gamma dt}{4\sigma^2(t)} \qquad [2.10]$$

Then, the probability of recombination per jump will be:

$$p_r(\tau,t)=\frac{a^2}{4\sigma^2(t)}=\frac{1}{2\,\Gamma(t-t_1-\tau)+4{\sigma_0}^2/a^2} \qquad [2.11]$$

The contribution of the H centers created at time τ to the AG signal in the interval $(t,t+\Delta t)$ is proportional to the probability $P_r(\tau,t)$ that the H center created at τ survives until t and recombine before time $t+\Delta t$. This probability is equal to:

$$P_r(\tau,t)=P_s(\tau,t)p_r(\tau,t) \qquad [2.12]$$

where $P_s(\tau,t)$ is equal to the product of the probabilities to survive each individual jump between the beginning of the random migration at $(t_1+\tau)$ and the final time t:

$$P_s(\tau,t)=\prod_{t_1+\tau}^{t}(p_s(\tau,t'))^{\Gamma\Delta t}=\prod_{t_1+\tau}^{t}(1-p_r(\tau,t'))^{\Gamma\Delta t} \qquad [2.13]$$

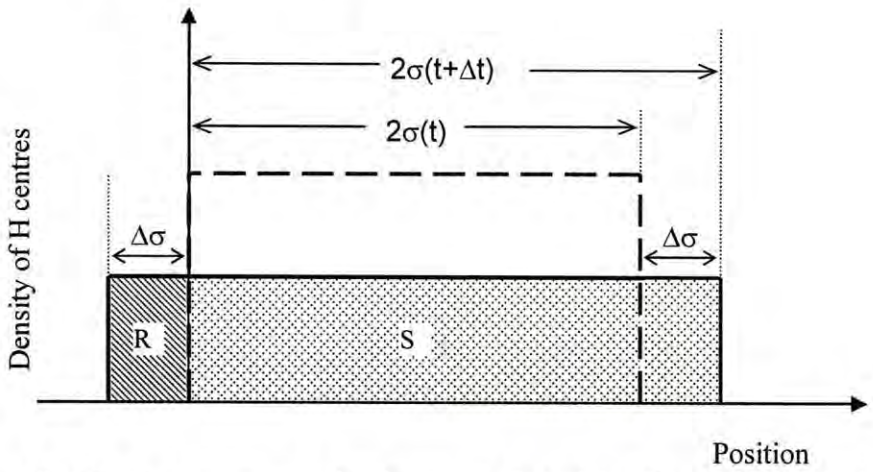

Fig. 2.2 The presence of the F center at the origin affects the broadening of the H centers distribution because of the recombination of the H centers that arrive at that site. After $\Gamma\Delta t$ jumps the width of the distribution tends to grow as indicated by $\Delta\sigma$ but only the H centers in the $2\sigma(t+\Delta t)$ interval, survive.

The terms in the product group together all the jumps in the Δt interval for which we suppose that the probability of recombination is practically constant.

To approximate the product in eq. [2.13] we use:

$$\prod_{x=x_1}^{x_2}(1-f(x))^{\Gamma dx} \approx \exp\left(-\Gamma\int_{x_1}^{x_2} f(x)dx\right) \qquad [2.14]$$

which is valid for small $f(x)$ and large difference $(x_2 - x_1)$. Applying eq. [2.14] to [2.13] and substituting eq. [2.11] and [2.13] into [2.12] gives:

$$P_r(\tau,t) = \frac{2\sigma_0/a}{\left[2\Gamma(t-t_1-\tau)+4{\sigma_0}^2/a^2\right]^{3/2}} \qquad \text{if } t > t_1+\tau \qquad [2.15]$$

The contribution of the H centers produced at τ to the luminescence at t is:

$$I(\tau,t)\,d\tau = \Gamma\, P_r(\tau,t)\,\xi\,d\tau \qquad [2.16]$$

where ξ is the production rate of H centers during the irradiation. Therefore, in the AG experiment after irradiation with short-pulses, the AG decay is expected to follow a $1/t^{3/2}$ law. In the AG experiments under continuous irradiation from $t=-t_r$ to $t=0$, the AG measurement starts after $t=0$. So the total luminescence at a time $t>0$ is thus the sum of the contributions of the H centers recombination that were created at each τ; integrating eq. [2.16] from $\tau=-t_r$ to $\tau=0$ we get:

$$I_{AG}(t) = \xi\frac{2\sigma_0/a}{\sqrt{2\,\Gamma(t-t_1)+4{\sigma_0}^2/a^2}} - \xi\frac{2\sigma_0/a}{\sqrt{2\,\Gamma(t-t_1+t_r)+4{\sigma_0}^2/a^2}} \qquad [2.17]$$

Note that for $t=t_1$ (the initial time where all the H centers contribute to the AG, including that created at time $\tau=0$) and $t_r >> t_1$, eq. [2.17] gives that the luminescence intensity is proportional to the production rate of H centers as expected.

If we assume that $t >> t_1$ and $t_r >> t$ then eq. [2.17] can be approximated by:

$$I_{AG}(t) = \frac{\xi A}{\sqrt{2\Gamma t}} \qquad [2.18]$$

and the AG decay can be approximated to a $1/t^{1/2}$ law.

2.3 Simulation of the H-center migration along dislocation lines

In the previous analysis it was assumed that the H centers reaching the F center position recombines with a probability $p=1$ deriving into an expression of the afterglow decay as $I = I_0\, t^{-\alpha}$, with $\alpha = 3/2$ for pulsed irradiation and $\alpha = 1/2$ for long irradiation times. However, if the start up assumption that migration initiates at a distance x_0 is relaxed, thus $x_0 = 0$, then the AG yield would be zero since all H centers recombine at the start of the migration process. For values of p lower than 1, the yield would increase but it is not clear how the α exponent would be altered. Considering p values less than 1 complicates the analytical approach to estimate the AG decay time-dependency. Therefore, we develop an algorithm to simulate the AG decay numerically which allow us to study the behavior of the AG decay at different recombination probabilities.

2.3.1 Computer program and algorithm

Basically the program repeats a cycle containing the creation, migration and recombination of an H center. The simulation should start with the exciton ground state. From there it can decay (recombine) with a probability p to the ground state of the crystal leading to the luminescence, or dissociate into an F and H center. In the program however, the cycle starts with the H center placed one site away from the origin where the F center is located. Thus the program ignores the cycles in which recombination occurs before migration. It is easy to correct this: if m is the number of cycles used by the program then the corrected number would be $m/(1-p)$. This correction has no effect on the shape of the AG decay.

Sufficiently far from the origin, the H center migrates according to a random walk where the probability to move k sites after n jumps is given by a binomial distribution. This distribution can be numerically generated by a standard routine $BNLDEV(p,n)$ which returns an integer value that is a random deviate drawn from a binomial distribution of n trials each of

probability p [Press, 1990]. The program repeatedly calls this routine with the number of jumps n equal to the number of sites that separate the F and the H center.

When the H center reaches the F center the lattice configuration returns to the exciton state. From there it is possible to recombine or to generate again an F–H center pair. To account for the regeneration, the program compares p with the random generator *RND*. If $RND > p$ the program lets the H center jump one site away from the F center and the migration continues. If $RND < p$, the array element associated with the interval corresponding to the total number of jumps of the cycle is increased by one and a new cycle is started.

The program returns the number of jumps given by the H center before recombination. The number of jumps falls into one of a set of prefixed intervals. In the program these intervals are association with array elements and after each cycle the corresponding array element is increased by one. Then a new array with the number of recombining H centers as a function of the number of jumps is constructed. This corresponds to the AG luminescence as a function of time.

2.3.2 Simulation results

To fit the data of the simulation of the AG decay, we propose a function like:

$$I(n) = \frac{I_0}{(n_0 + n)^{\alpha}} \qquad [2.19]$$

where I is the number of recombination events per jump, n is the number of jumps after F–H pair creation, and n_0 is an offset to prevent a discontinuity at $n = 0$. Note that for $n >> n_0$ this function is proportional to $n^{-\alpha}$.

Normalizing to N the total number of recombining F–H center pairs (or total amount of AG) by the integration of $I(n)$ from n_0 to the maximum number of steps n_f and assuming that $n_0 << n_f$, the fitting function is given as:

$$I(n) = \frac{N(\alpha - 1)n_0^{\alpha - 1}}{(n_0 + n)^{\alpha}} \qquad [2.20]$$

This new expression allows to introduce N as a fitting parameter and could be used satisfactorily for $\alpha > 1$.

Figure 2.3A shows the results of simulations with 1.25×10^7-H centers at different values of the recombination probability (p). The data could be fitted by the function of eq. [2.20] in the range $n=\left(5\times10^3, 4.99\times10^5\right)$ with n_0 taken as 1 and, N and α as fitting parameters. For $p=1$, the exponent is $\alpha=1.49$ being very close to $\alpha=3/2$ expected by the analytical estimation of eq. [2.15]. The exponent is almost constant for lower recombination probabilities except for $p<0.2$ where it decreases and reaches the value $\alpha=0.5$ at $p=0$ (Fig. 2.3B). The latter value has been obtained from the consideration that for $p=0$ the H center distribution changes according to that of a random walk (which is Gaussian) whose width grows like $n^{1/2}$ and the height like $n^{-1/2}$. Then, the top of the distribution is at the origin and the recombination rate would be proportional to the height of the distribution.

This results means that the shape of the AG decay remains constant and the AG signal is simply scaled down along the signal axis which should corresponds to a non-constant value of parameter n_0. The fitting of the simulation data fails at short p values because eq. [2.19] is not valid for $\alpha<1$. This problem could probably be solved if a non-constant value of

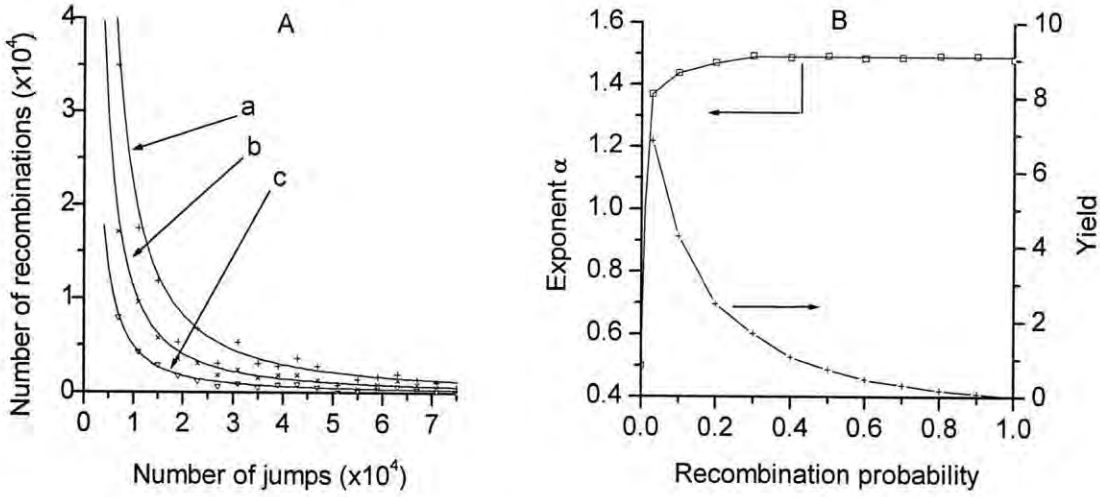

Fig. 2.3. Results of fitting equation [2.19] to the simulations of AG with different recombination probabilities. (A) shows the AG curves for (a) p = 0.2, (b) p = 0.4 and (c) p = 0.9. (B) shows the AG yield and the exponent α as function of recombination probability.

the n_0 parameter is taken, however the analysis would be more difficult.

From the simulation data, the AG yield could be calculated as the ratio between the total recombining F–H center pairs (N) and the total number of created excitons (m):

$$Y = \frac{(1-p)N}{m} \qquad [2.21]$$

The factor $(1-p)$ is included to correct for the created excitons that never form F–H center pairs. For $p=1$ the yield is zero since all the F–H center pairs already recombine before the first jump. For smaller p the yield grows even higher than 1. The reason for this is that for smaller values of p the decay curve tends to shift to the origin corresponding to an increase of n_0. In a range far from $n=0$, this is almost not noticeable. So a fit with n_0 fixed at 1 still gives a good result however with an increased N to compensate for the too small value of n_0. This causes the yield to grow to values higher than 1.

In conclusion, we see from Fig. 2.3B that the proposed mechanism for AG leads to a $t^{-3/2}$ decay and to significant yield for a wide range of p values.

CHAPTER 3:
AG/TL RESEARCH FACILITY

Eu-doped alkali halide crystals exposed to UV irradiation at low temperatures will be studied by three phenomena: (*i*) the luminescence emitted during irradiation (photoluminescence, PL), (*ii*) the luminescence remaining after end irradiation (afterglow, AG) and, (*iii*) the luminescence during heating at constant rate after end irradiation (thermoluminescence, TL). For a systematic study of the three luminescences under different irradiation conditions, an experimental system in which all these functions could be automatically executed without alterations of the sample orientation would be very useful. Such a system would improve the reproducibility and the efficiency of the experiments.

In this chapter, a research facility designed to perform systematic studies of PL, AG and TL after irradiation with UV-visible light at temperatures from 20 to 300 K is described. The main advantage of this system is the automation of the operational functions allowing to perform a complete series of experiments. Section 3.1 describe the experimental setup. Section 3.2 presents the control mechanisms which allow the complete automation of the measurement. Finally, section 3.3 presents the different corrections which should be perform in the experimental data before their analysis.

3.1 Experimental setup

The experimental setup is basically an Helium cryostat to cool down the sample temperature to 20 K combined with a spectrofluorometer to irradiate the sample with UV-visible light and register the sample luminescence by a computer. The main adaptations to perform our experiments are: (*i*) a heating system attached to the cold finger of the refrigerator which allows to control the sample temperature up to room temperature, and (*ii*) an external irradiation system which provides a higher light intensity than the internal lamp of the spectrofluorometer. A detailed drawing of the complete setup is shown in Fig. 3.1. The experimental setup can be divided in a section that controls the sample-temperature and a section that controls the irradiation and emission detection system.

3.1.1 Sample-temperature setup

The main component of the temperature system is a two-stage cryogenic Helium refrigerator (APD, model DE-202). The refrigerator is supplied with oil-free helium gas by a single stage rotatory compressor (APD, model HC-2D) which is cooled by a water flow supplied by a circulator (APD, model CP-4). The cold end of the helium refrigerator is protected by a shield equipped with four quartz windows for optical access to the sample. To minimize the thermal conductivity between the cold finger and the exterior, a vacuum atmosphere inside the shield is created with a mechanical vacuum pump (ALCATEL, model 2010). The vacuum pressure is measured with a vacuum gauge head (EDWARDS, model PR25-K) places close to the pump output and at about 1 meter far from the refrigerator input. In this configuration the working pressure measured with a vacuum-meter (EDWARDS, model Pirani-14) is around 1-2 x 10^{-2} mbar. This vacuum pressure results enough to down the cold finger temperature slightly below 20 K. Lower temperatures around 11 – 12 K could be reached if a second envelope is assembled to the cold finger. However, this second shield difficult the alignment of the sample.

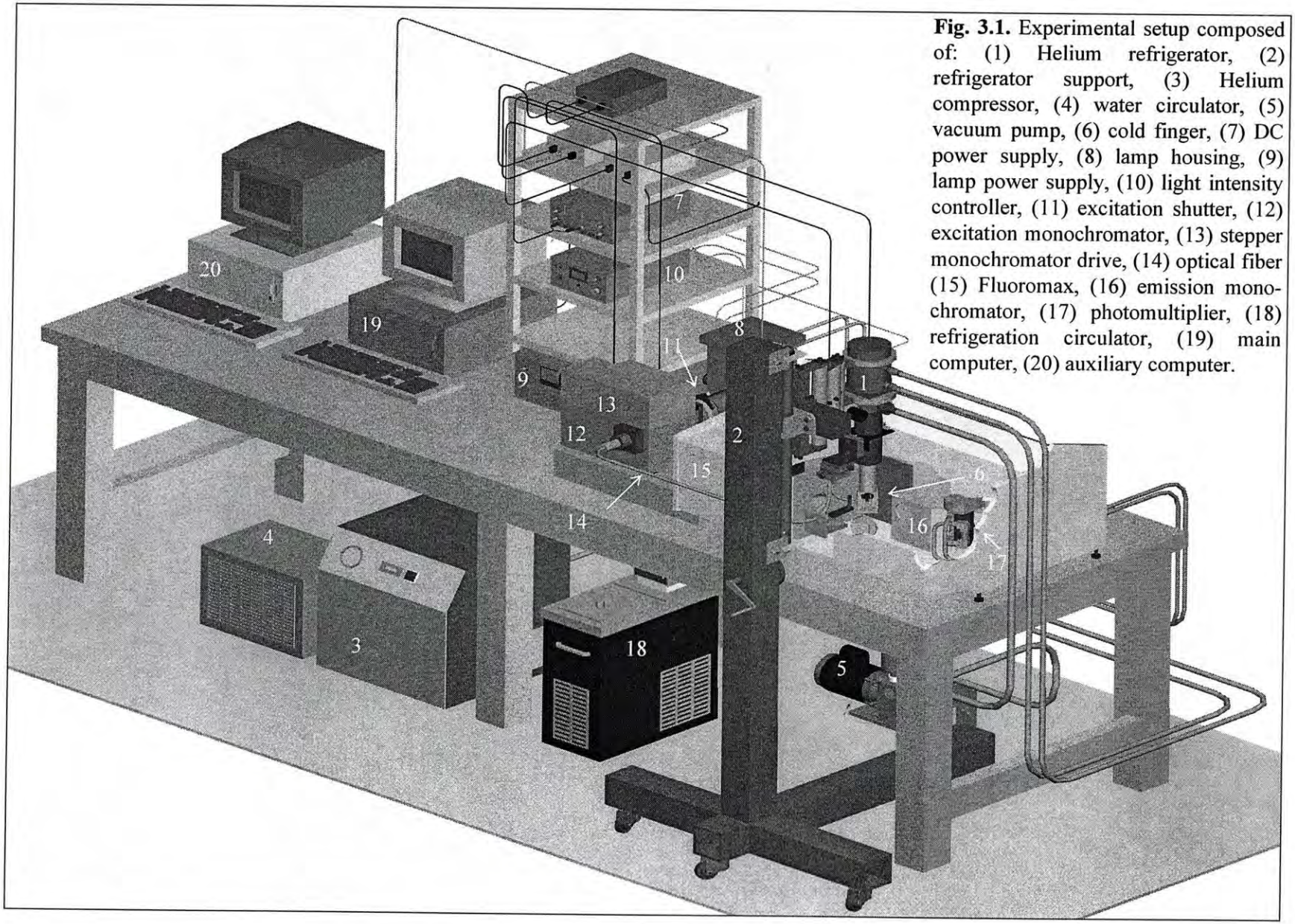

Fig. 3.1. Experimental setup composed of: (1) Helium refrigerator, (2) refrigerator support, (3) Helium compressor, (4) water circulator, (5) vacuum pump, (6) cold finger, (7) DC power supply, (8) lamp housing, (9) lamp power supply, (10) light intensity controller, (11) excitation shutter, (12) excitation monochromator, (13) stepper monochromator drive, (14) optical fiber (15) Fluoromax, (16) emission monochromator, (17) photomultiplier, (18) refrigeration circulator, (19) main computer, (20) auxiliary computer.

Fig. 3.2. Detail of the cold finger: (1) cold finger (2) copper piece, (3) sample, (4) heating resistors, (5),thermocouple (6) external shield, (7) quartz windows.

At the cold finger, a home-made copper piece is assembled which was designed to hold the sample, two resistors and an Au-Constantan thermocouple (detail in Fig. 3.2). The two resistors are connected to a DC power supply (HP, model 6205B) controlled by a computer.

The sample is pressed by a thin wire over a flat vertical wall. In this way, we avoid the use of a paste compound, such as vacuum grease, from which we have observed a persistent luminescence emission in the same wavelength range as that of the sample emission. Although during illumination, this luminescence was negligible because the intense PL emission of the sample, it interfered significantly with the AG emission of the sample. Furthermore the emission spectrum of the paste compound observed by the detector was not constant due to the absorption of the sample situated in front of it. In a previous work, these spectra were erroneous interpreted as an AG signal that decayed quickly during the first seconds after irradiation with an emission slightly different in each sample [Alvarez-Garcia 2003].

3.1.2 Irradiation-emission setup

The irradiation source is an 450 W Xe arc lamp (ORIEL, model 6262) located inside an universal housing (ORIEL, model 66921) and connected to a highly regulated power supply (ORIEL, model 68920). The lamp radiation is constantly measured with a light intensity controller (ORIEL, model 68850) which compares it to a reference level and cancels any difference by adjusting the power supply output. In this way, a long-term stable output for the arc lamp is ensured. The irradiation light is dispersed by a monochromator (KRATOS, model GM252) equipped with a 0.33 nm/mm dispersion grating. The monochromator is controlled by a stepper motor drive (KRATOS, model GMA301) which allows to select the wavelength with an 0.1 nm/step resolution.

Before crossing through the monochromator, the light is blocked by a home-made shutter controlled by a stepper motor (Fig. 3.3). This shutter was designed to assemble the lamp housing output and the monochromator fixing the alignment between them. The shutter is controlled by a stepper motor connected also to the parallel port of the computer. From the monochromator output, the light is guided through a high-grade fused silica fiber (Oriel, model 77578). The end of the optical fiber is fixed and aligned using a home-made support

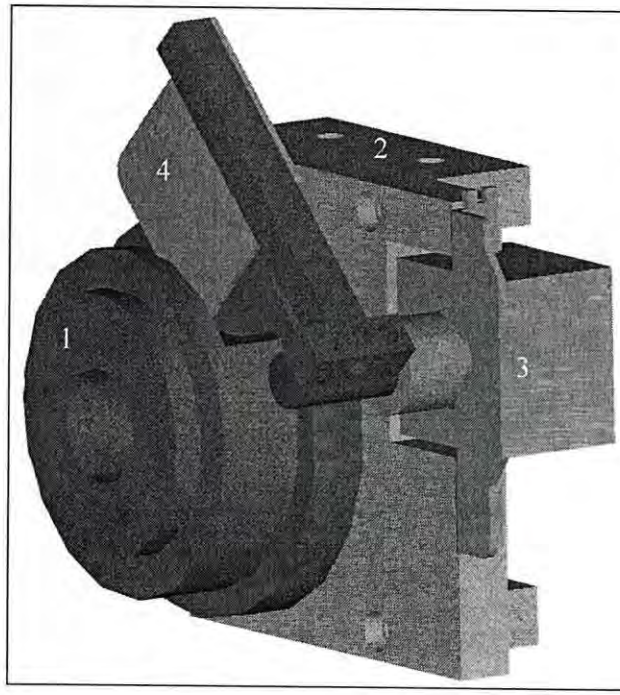

Fig. 3.3. Detail of the excitation shutter: (1) piece to assemble to the lamp housing, (2) piece to assemble to the monochromator, (3) stepper motor, (4) mobile shutter.

assembled to the sample compartment of a spectrofluorometer (SPEX, model Fluoromax).

The sample mounted inside the refrigerator is introduced into the sample compartment of the Fluoromax. To make easy the alignment of the sample a home-made two-axis positioning system fixed to the cold finger shield is used. Additionally the refrigerator is supported by a home-made three-axis arm which allows its free movement. The luminescent light emitted by the sample is collected by the Fluoromax emission channel and dispersed by the emission spectrometer with a 4.25 nm/mm dispersion. The emission light is registered by a photomultiplier tube (HAMAMATSU, model R928) operating in the photon-counting mode. To reduce the fluctuation of the background signal, the photomultiplier temperature is kept constant with an external water circuit at 15°C supplied by a refrigerating circulator (POLYSCIENCE, model 1160-A).

3.2 Experiment control

The automation of the experiment is carried out by two interconnected computers. The Fluoromax is connected to the serial port of the main computer (PC1) from which the operational functions are controlled by a software (SPEX, model DM3000F). A second computer (PC2) is connected to PC1 via the serial port and control the sample temperature system. The monochromator and the excitation shutter are connected through the parallel port to PC1. The excitation shutter and the monochromator are moved using an stepper motor and the control programs are designed in QBasic language. A schematic diagram of the experiment connections is showed in Fig. 3.4.

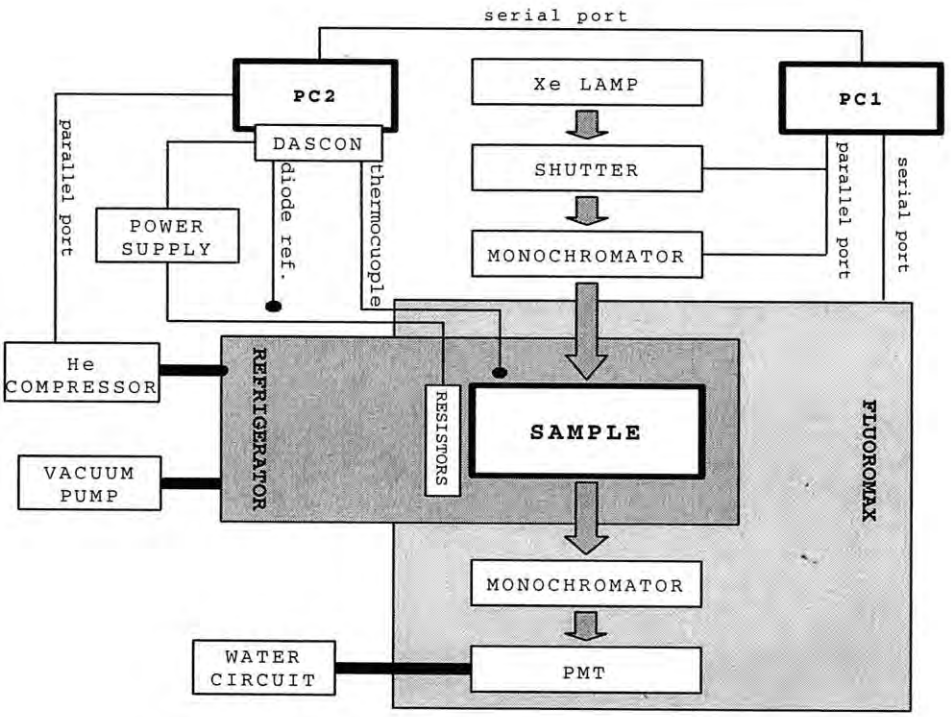

Fig. 3.4. Schematic diagram of experimental setup.

3.2.1 Temperature control

The temperature of the sample is controlled by a personal computer (PC2) using the resistors and the thermocouple located close to the sample, a diode located outside the cryostat and the power supply of the resistors. The communication between the computer and the elements is through a multifunction analog/digital I/O expansion board (KEITHLEY, model Dascon-1). A home-designed control program calculates the sample temperature by comparing the thermocouple signal with that of the diode working as reference level at room temperature. This diode was previously calibrated using a water bath. The response of the thermocouple was taken from the manufacturer data. The cold finger temperature is cooled down at around 18 – 19 K by the refrigerator and could be raised by increasing the current through the resistors. The control program allows two main tasks: (*i*) to stabilize the sample temperature to any value in the range 20 – 300 K, with an error of around 1 K and, (*ii*) to raise the temperature at a constant rate of 0.1 K/s, from 20 to 300 K. In the last case, a predefined

temperature profile is followed by the program and any deviation is cancelled by adjusting the current through the resistors. Higher temperatures up to 400 K could be reached if the helium refrigerator is previously turned off and the cold finger is warmed up to RT.

3.2.2 Experiment automation

The experiment is automated using the DM3000F software which controls the Fluoromax from computer PC1. This software is based on a sequence of menus that guide the user to control manually the spectrofluorometer, specify the experiment parameters, acquire data, display data, manage files, etc. A specific task can be automated by storing in a file the keystrokes necessary to execute it (move through the menus, insert parameters, etc). A single *keystroke procedure* can be used to execute similar tasks (for example, emission spectra with different excitation wavelengths) by saving the experimental parameters in registers and changing their values before running the *procedure*. There are available 100 registers (00-99) which could be stored in files in groups of 10 registers. The content of a register could be called at any time being possible to make basic operations with them (+, -, *, /).While a *keystroke procedure* is running, predefined *windows* can be used to ask inputs to the user. A *window* contains a maximum of ten prompts defined by the programmer to ask parameters and to save them in registers. The DM3000F software also allows to leave temporally the program and to run a DOS order like a QBasic program.

Using the tools of the DM3000F software, we designed a methodology to automate complex experiments. The *experiment program* is contained in a set of 100 registers saved in 10 files identified with the same prefix and a number. As an example, Appendix 2 shows the *experiment program* designed to run emission scans during AG and TL after irradiation at different temperatures, wavelengths and times. The registers 21 to 70 contain a list of individual *keystroke procedures* designed to execute specific tasks. The rest of registers store parameters that will be used for more than one *procedure.* Registers 90 to 98 are used as erasable registers. The experiment is initiated by calling the *keystroke procedure* "start" which loads the files containing the registers of the *experiment program* and initiates to execute the *procedure* in register 21. When this *procedure* is finished, it calls to execute the *procedure* "continue" (in register 99) which calls the next *procedure* in the list. The *procedure*

"progloop" initiates a loop in the *program* (a maximum of 4 loops are allowed). When the procedure "endloop" is executed, the program returns to the register position of the "progloop" (saved in registers 81 to 84). At each loop, a parameter of the experiment could be changed like the irradiation temperature. This parameter is calculated from the initial data of the loop (registers 1-12) and the number of loops resting (registers 71 to 74) which is subtracted by an unity each time that the "endloop" is executed. The "endloop" *procedure* stops looping when the number of loops resting is null. The *program* continues executing until the register with the *procedure* "end" is reached and then the experiment is finished.

3.3 Data corrections

In general, the data obtained in a luminescence experiment does not correspond with the intensity emitted by the sample. There are several factors inherent in the experimental system involved in the measurement process which modify the registered intensities. These factors are mainly the background signal, the response of the detection system and the spectrum of the excitation light. During the data analysis some of these factors could be ignored but in general they should be taken into account as correction factors to the experimental data. Each correction factor will be analyzed below. Furthermore, the conversion of the emission spectra from the wavelength scale to the energy one is included. This conversion is necessary for the analysis of the emission spectra shape.

3.3.1 Background

The photomultiplier (PMT) has a non null signal when it is in dark. In our experiment, the dark signal is kept almost constant by holding the PMT at a constant temperature around 15°C. The resulting background signal is around 600 – 700 counts per second (cps). The experimental data could be corrected for the background signal by subtracting the mean of several data points from a section of the emission spectrum outside the wavelength range where the sample emits.

3.3.2 Detection system response

The response of the detection system is due to aberrations of the lens, diffraction in the monochromator grating and efficiency of the detector. The response of the detection system of the Fluoromax was calibrated by the manufacturer which supplied a correction spectrum. However, in our experiments the original PMT tube (Hamamatsu, model R1527P) was replaced by another one with a large detection range (Hamamatsu, model R928) so that the supplied correction spectrum is not applicable. To calculate the new correction spectrum, we compare the emission spectra registered by both PMT detectors of a quartz cell filled with distillate water. Then the correction spectrum is calculated from the data of the original PMT multiplied by the ratio between the water emission spectra measured by the original PMT and by the new one. Fig 3.5 shows the detector response normalized to unity at the lower value. Finally, the correction of the emission spectra is calculated by multiplying the data by the correction spectrum.

3.3.3 Excitation light

The excitation spectra should be corrected by the wavelength dependence of the light source, the excitation monochromator and the absorption of the optical fiber. To generate the correction curve, it is necessary to determine the relative light reaching the sample compartment of the spectrofluorometer at each wavelength. To do that, we measured the excitation spectra of a quartz cell filled with Rhodamine (5 g/l in ethylene glycol). The Rhodamine is characterized by an absorption almost constant over a wide wavelength range producing the emission of a luminescence peak centered at around 660 nm. Then the excitation-correction spectrum is obtained by measuring the light intensity emitted by the Rhodamine after irradiation at different wavelengths in the range 200 – 600 nm. The correction spectrum changes due to ageing of the lamp and should be measured periodically (Fig. 3.5). Then, the experimental data at different irradiation wavelengths would be corrected by multiplying by the excitation-correction spectrum.

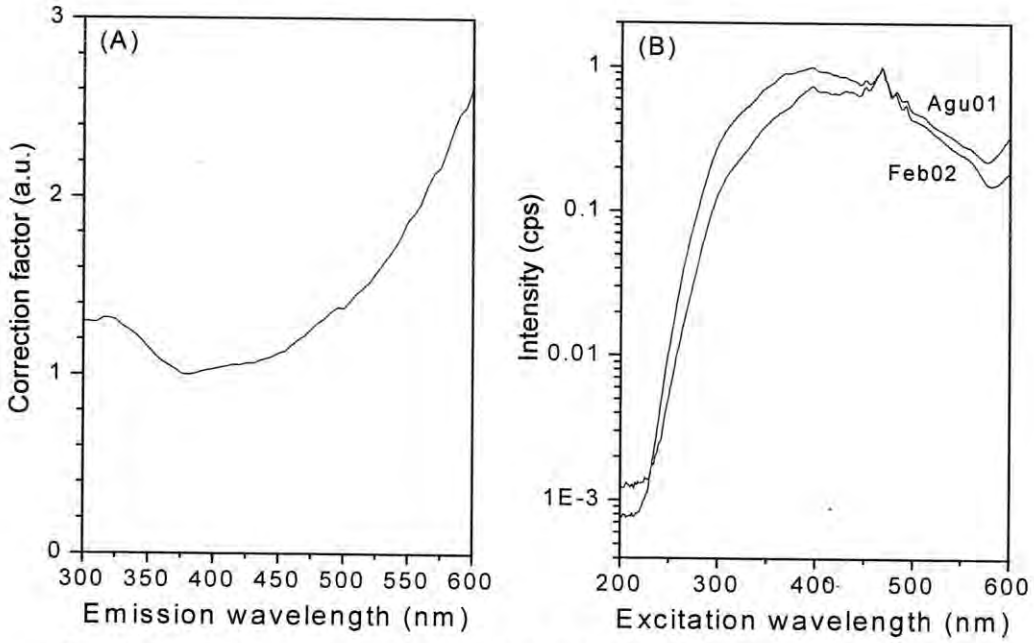

Fig. 3.5. (A) Spectrum of the correction by the response of the detection system. (B) Spectra of the correction by the excitation light.

3.3.4 Conversion from wavelength to energy

The emission spectra are registered as the intensity reaching the detector at different wavelengths selected with the emission monochromator. However, the monochromator has a bandpass which depends on the slit width and the wavelength dispersion in the grating (4.25 nm/mm). Therefore an emission spectrum corresponds to the intensity $I(\lambda)d\lambda$ registered in a wavelength interval around the selected wavelength λ.

The change of an emission spectrum to the energy scale implies the conversion of the x-axis given by the relation

$$E = \frac{hc}{\lambda} \qquad [3.1]$$

and also the conversion of the y-axis:

$$I(E)\,dE = \left|\frac{\partial E}{\partial \lambda}\right| I(\lambda)\,d\lambda = \left(\frac{hc}{\lambda^2}\right) I(\lambda)\,d\lambda \qquad [3.2]$$

Therefore the intensity registered at each wavelength λ should be multiplied by a factor (hc/λ^2).

CHAPTER 4:

AFTERGLOW AND THERMOLUMINESCENCE IN Eu DOPED ALKALI HALIDES UV-IRRADIATED AT 20 K

In this chapter, the afterglow (AG) and thermoluminescence (TL) of some Eu-doped alkali halide crystals exposed to low-energy UV-light at temperatures below RT is presented. The measurements are performed with the research facility of chapter 3. Both phenomena are analyzed and discussed according to existing models mentioned previously (section 1.3.5 and chapter 2).

Three different experiments are presented in Eu-doped alkali halide crystals: AG and TL emission spectra after irradiation with different UV-light wavelengths at 20 K (section 4.1); time scan experiments of the AG decay after irradiation at fixed wavelength at 20 K for different irradiation times (section 4.2) and; TL experiments at fixed irradiation wavelength and time for different irradiation temperatures in the range 20 – 300 K (section 4.3). The results of the first experiment are reported for three alkali halides: NaBr:Eu, KBr:Eu and KCl:Eu; the two later experiments imply a detailed analysis of the experimental data and therefore they are reported only for the KCl:Eu crystal.

4.1 AG and TL emission and creation spectra under UV irradiation at 20 K

Crystals of KCl, KBr and NaBr doped with 0.1 wt. %Eu were grown at the *Instituto de Física de la Universidad Nacional Autónoma de México* by the Czochralski method. The crystals were cleaved in samples of about 7 x 5 x 1.5 mm. Then, they were wrapped in Al foil and place into a pre-heated furnace (THERMOLYNE, model 1310). After remaining there at 500°C for 30 min, they were quickly cooled down by pressing them onto a copper block at RT. Samples were stored in darkness before measurement. Irradiation was performed during 900 s with an UV 450 W Xe arc-lamp at around 20 K. After blocking the irradiation light, 20 emission spectra were registered during the AG decay. After AG decayed, 75 TL emission spectra were registered during heating at a rate of 0.1 K/s. Both AG and TL emission spectra were detected with a resolution of 8 nm. After each AG/TL measurement, the sample was cooled down to 20 K and the procedure was repeated to the next irradiation wavelength in the 400 – 200 nm range at 5 nm intervals in descending order. The spectra were not corrected by the response of the detection system neither the wavelength dependence of the irradiation channel.

In Figure 4.1 the excitation-emission spectra of the AG intensity integrated to decay-times up to 100 s and the TL intensity integrated at the full temperature range are shown. The emission spectra of the AG and the TL are similar in each of the Eu-doped alkali halide crystals. The main band is centered around 430 nm in NaBr:Eu and around 420 nm in KBr:Eu and KCl:Eu samples. These central emissions correspond to the characteristic emission of the Eu impurity reported at around 428 nm, 418 nm, and 419 nm in quenched NaBr:Eu, KBr:Eu and KCl:Eu crystals at RT, respectively (see Table 1.2). In KBr:Eu and KCl:Eu crystals, the emission spectra also present a less intense band at higher wavelength extending to around 500 nm. These bands could be related to some Eu-precipitates which were not dissolved by quenching.

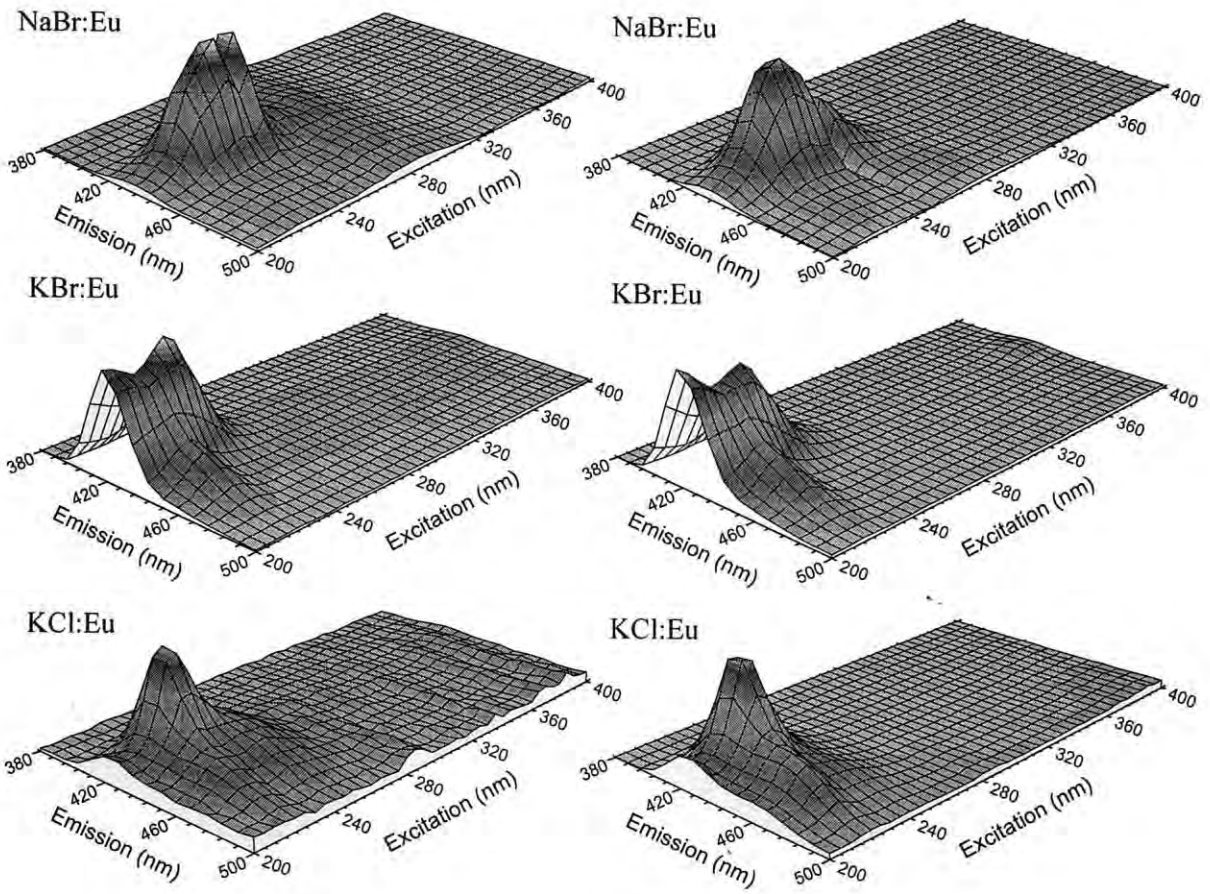

Fig. 4.1. Excitation – emission spectra of the integrated AG and the integrated TL in NaBr:Eu, KBr:Eu and KCl:Eu.

In NaBr:Eu, the excitation spectra of the AG and the TL are formed by a band around 235 nm. The appearance of two excitation peaks in Fig. 4.1 is caused by an experimental error in the 245 nm measurement. In KBr:Eu the excitation spectrum of the main emission band is composed of two bands, one centered below 200 nm and the other one around 230 nm. Additionally an excitation band around 220 nm for a weaker emission band at higher wavelengths is observed. In KCl:Eu, the excitation of both emission bands is composed of a main band around 230 nm and another band extending to 250 nm. All the excitation spectra are in the high-energy absorption region of the Eu impurity, agreeing with the data reported to the AG emission at RT by Aguirre *et al* [Aguirre 1988].

The similarity between the TL and AG creation spectra as observed, would be expected considering either a model of tunneling recombination or a model based on migrating H centers. In the first model, the TL traps would be the same from which electrons

tunnel during the AG. In the second model, the AG would be explained by the F–H recombination due to not yet trapped H centers that after randomly migration return to the origin where they were created. In the latter case the TL would come from the release of H centers trapped at H center traps. So one expect the same excitation and emission spectrum for AG and TL [Alvarez-Garcia 2001].

4.2 Analysis of the AG decay in UV-irradiated KCl:Eu at 20K

For the analysis of the AG decay, we used a KCl:Eu crystal which was previously annealed at 500°C. The sample was placed in the setup described in Chapter 3 and cooled down to 20 K. The irradiation was performed with light at 225 nm during different times (t_r) from 10 to 2010 s. After the irradiation period, the light was blocked and the AG signal at fixed emission (at 422 nm) was continuously measured for a period of 700 s. The time between the end of irradiation and the first AG measurement was around 4 – 5 s. After that, the thermoluminescence at 422 nm emission was measured during heating at a rate of 0.1 K/s until RT. Then the samples was cooled down to 20 K to start a new cycle of measurement. In this way, it was expected that the defects formed during the irradiation were completely bleached and the conditions before each measurement were similar. The AG and TL curves were corrected for the background level obtained by averaging 100 emission data points measured during the cooling down after the TL measurement.

When the irradiation period is increased, the integrated AG intensity grows quickly at short irradiation periods and approximates to a constant value for long periods (Fig. 4.2). The integrated TL intensity increases linearly with the irradiation time. The dependence of the AG intensity with the irradiation time could be explained as follows. The recombination rate would depend on the concentration of created defects. Since the number of created defects grows with increasing irradiation time, the AG recombination also increases leading to an initial rise of the integrated AG intensity with increasing irradiation time. The AG recombination rate continuous to increase until it is balanced by the creation rate. Then the

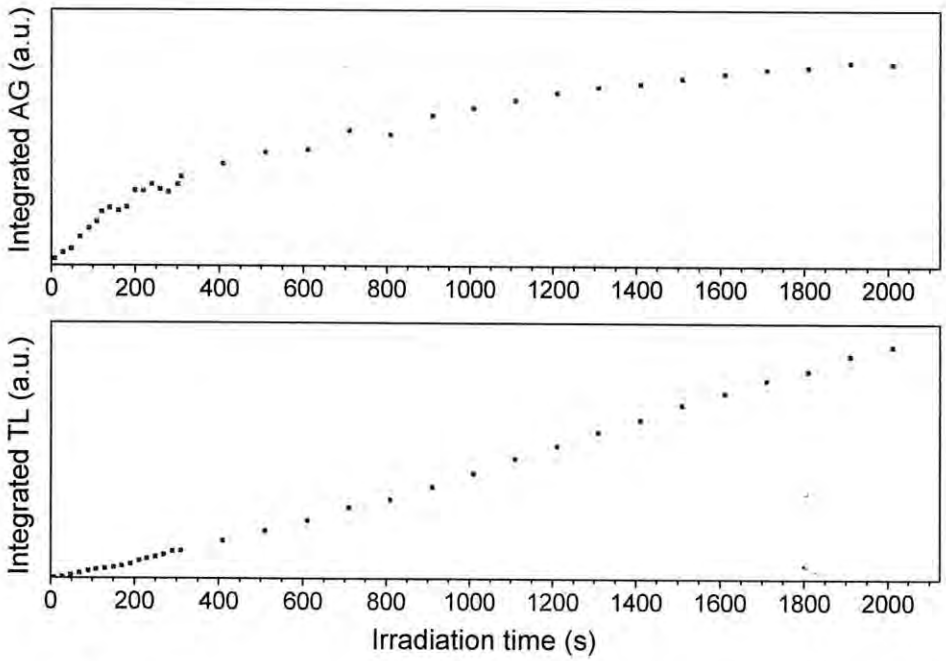

Fig. 4.2. Integrated AG decay curve and TL glow curve for KCl:Eu irradiated at 20 K for different irradiation times.

concentration of available created defects does not increases any more, resulting in a constant AG signal for long irradiation times. The linear increase of the TL intensity could be explained as follows. A small fraction of the created defects is trapped in TL active traps. As long as the number of available traps does not decreases too much, the filling rate remains constant resulting in a linear increase of the TL signal with irradiation time.

The experimental data reveals that the curvature of the AG decay curve decreases monotonically as the irradiation time is increased (Fig. 4.3). This result implies that the AG process is not due to any uncorrelated recombination of an uniform distribution of centers such as second order isothermal decay. In that case, one would have expected that the curvature of the AG decay curve is independent of irradiation time. The change of curvature with increasing irradiation time suggests that the AG decay is given by the integration of many independent recombinations between correlated pairs.

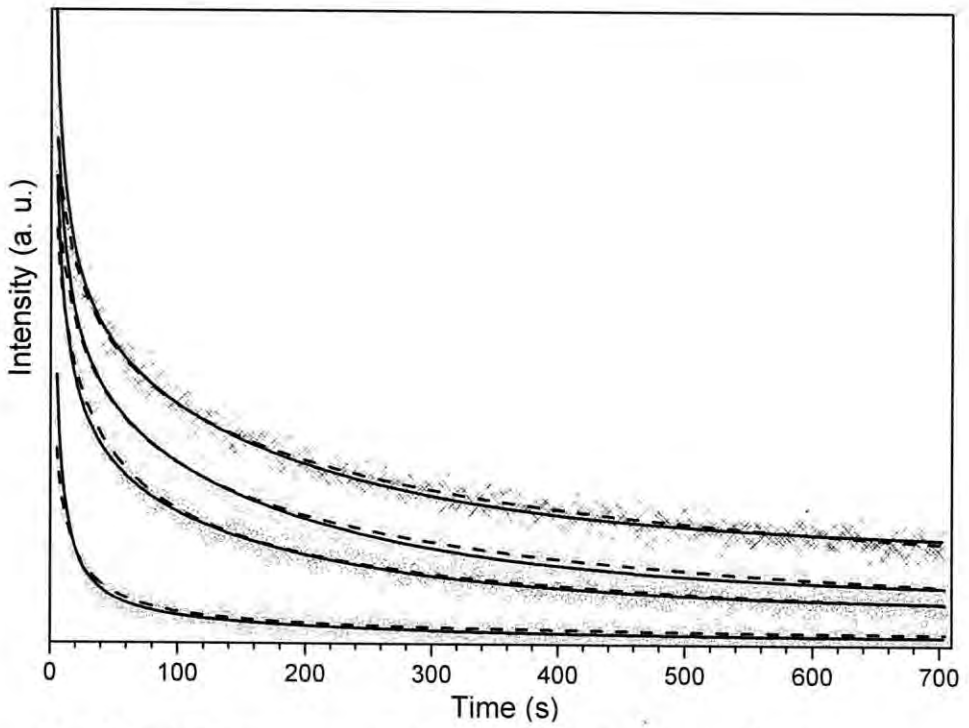

Fig. 4.3. AG decay curve at different irradiation times: 27 s (squares), 210 s (circles), 509 s (triangles) and 910 s (crosses) for the KCl:Eu irradiated at 20 K. The simulated curves according to the tunneling model (dashed lines) and to the corrected migration model (continuous lines) are also included.

4.2.1 Analysis of the AG according to a tunneling mechanism

AG decay in KCl:Eu has been observed to follow a t^{-1} function after pulsed irradiation which was associated to a tunneling decay due to a continuous distribution of electron traps (see section 1.3.4 and Appendix 1). Here, we analyze the AG decay assuming a continuous distribution of traps and then we evaluate how realistic this assumption is.

For long irradiation times, as in our measurements, the t^{-1} function should be integrated as:

$$I(t) = \int_{t'=0}^{t'=t_r} \frac{A}{t+t'}\, dt' \qquad [4.1]$$

which results in

$$I(t) = A \ln\left[1+\frac{t_r}{t}\right] \qquad [4.2]$$

with I the AG intensity, t the time after the end of irradiation, t_r the irradiation time and A the amplitude.

The fitting of eq. [4.2] to our experimental data with t_r fixed at the irradiation time and with A as the adjustable parameter resulted in good fitting for all curves (Fig. 4.3). The parameter A remains almost constant around 610 with small fluctuations which could be due to the error in the calculated background signal. We again fitted eq. [4.2] with A as a shared parameter for all curves and including an additional parameter (I_0) representing the error in the background signal. The result shows that I_0 decreases systematically for longer irradiation periods which we can not account for. However the decrease is small compared to the extent of the background signal (Fig. 4.4).

The fitting function [4.2] is valid for a continuous distribution of recombination pairs. The main contribution to the AG intensity comes from pairs separated by a distance close to the so-called frontier radius which is increasing while the measurement proceeds. The separation distance of the recombination pairs which are participating in the AG at time t could be estimated from eq. [A1.5], being the larger distance for the pairs created at the

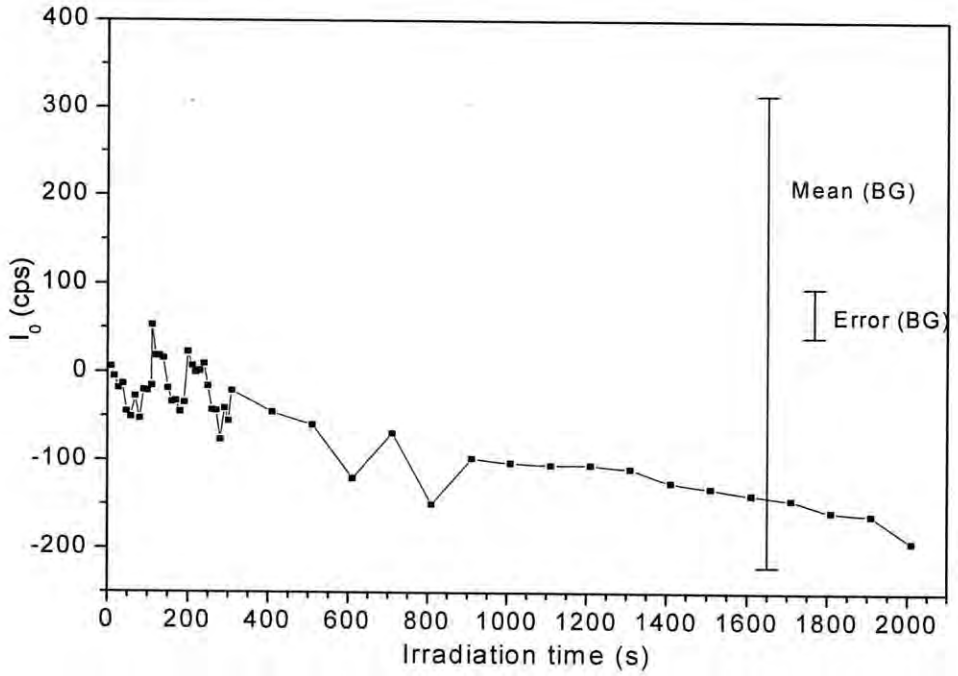

Fig. 4.4. Dependence of the I_0 parameter with the irradiation time to the fitting to a tunneling mechanisms with A = 610. The extension of the mean value of the BG at different irradiation times, and the error in BG is also shown.

beginning of irradiation ($t = -t_r$) and the shorter distance for those created at the end of irradiation ($t = 0$). The numerical values of parameters in eq. [A1.5] have been calculated by a quantum mechanical treatment of the F–H center tunneling recombination in KCl [Shluger 1981] resulting that the separation of a defect pair which recombines at time t is given by:

$$R(t) \approx \frac{1}{2\alpha} \ln\left(\frac{t}{\tau}\right) = 0.5 \ln\left(10^{13} t\right) \qquad \text{(in Å)} \qquad [4.3]$$

Fig. 4.5 shows the distances R corresponding to t and $t + t_r$ at different irradiation times. It can be observed that the interval of separation distances of pairs participating in the recombination is only several Angstroms. To verify the supposed continuous distribution of traps, the distances at which the Cl-Cl pairs appears in a KCl lattice (lattice parameter of 6.29 Å) were calculated and plotted in Fig. 4.5. We only found two of them inside the recombination region (Fig. 4.5, horizontal bars). Then, the AG would be expected to decay exponentially for short irradiation times and bi-exponentially for the longer ones. Therefore, if tunneling is the

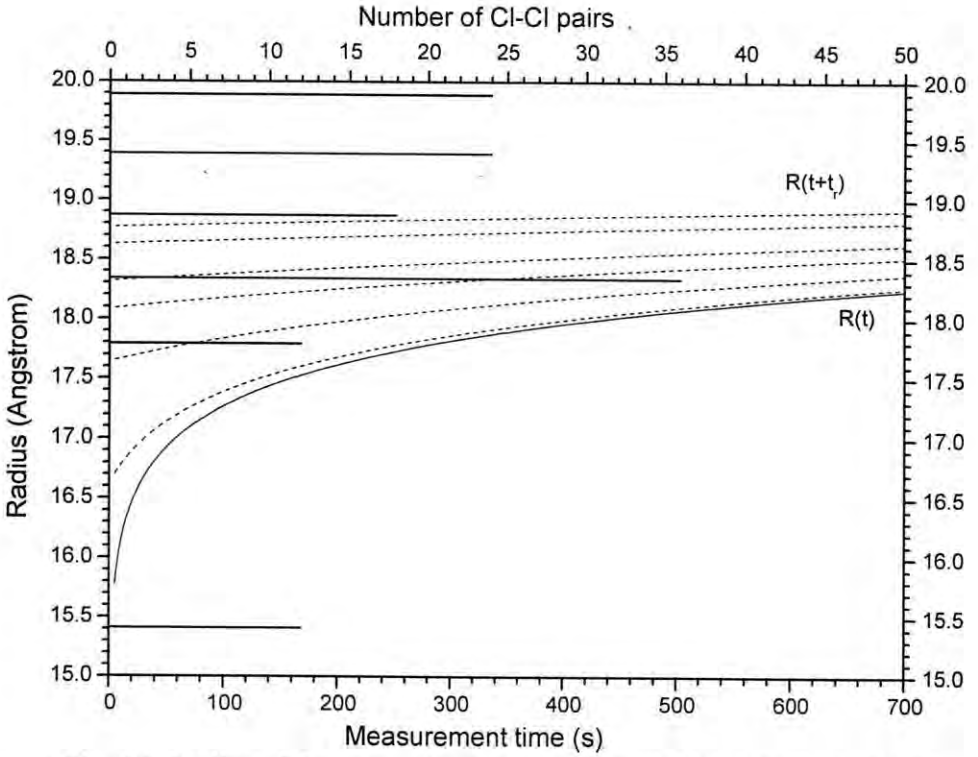

Fig. 4.5. Radius of the recombinant pairs at time t (solid line) and at time $t + t_r$ at t_r = 27, 210, 509, 809, 1509, 2010 s (dashed lines). The distance of the Cl-Cl pairs in a KCl lattice are show as horizontal bars. The length of the bar is given by the number of Cl-Cl pairs at that distance.

underlying mechanism of AG, we must assume that the parameters in eq. [4.3] are slightly higher than expected from the Shluger's calculations. An increase of one order of magnitude in the τ^{-1} value or a 10% increase in the $1/2\alpha$ value would be enough to displace the $R(t)$ and $R(t+t_r)$ curves to longer radius covering at least four Cl-Cl separation distances. In conclusion, the supposition of tunneling recombination by a continuous distribution of trap leads to very acceptable fittings with the experimental data.

4.2.2 Analysis of the AG according to a model of migration along a line

The model developed in Chapter 2 predicts an AG decay as:

$$I(t)=\frac{A}{(t)^c}-\frac{A}{(t+t_r)^c} \qquad [4.4]$$

with A the amplitude and t_r the irradiation time. The exponent is expected at $c \approx 0.5$.

Taking t_r fixed at the irradiation time, the fitting curves approximate to the experimental data quite acceptably at different irradiation times except at $t_r < 300\,s$ where the fitting fails. However the parameters are not as the expected values with $c \approx 0.055$.

A first correction to the model could include the participation of some thermally assisted process presented at the irradiation temperature (20 K). Then, the isothermal decay of a thermoluminescence peak could disturb the AG decay.

The participation of the TL signal would be given by the following rate equations:

$$\frac{dn_{TL}}{dt}=k-\alpha n_{TL} \qquad [4.5]$$

$$\frac{dn_{TL}}{dt}=-\alpha n_{TL} \qquad [4.6]$$

where k is the creation rate which is constant during irradiation and null after irradiation, and α is the recombination rate constant. Eq. [4.5] applies to the period during irradiation and eq. [4.6] to the period after irradiation. Integration of eq. [4.6] results in an exponential decay whose proportionality constant, the initial TL intensity, results from the integration of eq. [4.5] during the period of irradiation $(0, t_r)$. Then the contribution of the TL decay is given by:

$$I_{TL}(t)=B\left[1-\exp(-\alpha t_r)\right]\exp(-\alpha t) \qquad [4.7]$$

and the new fitting function of the AG decay will be

$$I(t) = I_0 + \frac{A}{(t)^c} - \frac{A}{(t+t_r)^c} + B[1-\exp(-\alpha t_r)]\exp(-\alpha t) \qquad [4.8]$$

with c fixed at 0.5. In eq. [4.8] the parameter I_0 was included to consider the errors in the measured background signal.

Good fitting results were obtained using eq. [4.8] in the simultaneous fitting of several decay curves with different irradiation periods: t_r = 27, 210, 509, 910 s. The parameters found where A = 5351; B = 877.4, $\alpha = 5.027\times10^{-3}$ (Fig. 4.6). Parameter I_0 was allowed to vary freely and was plotted in Fig. 4.7 as function of t_r. From this figure, it can be observed that I_0 increases quite linearly with increasing irradiation period. Although small, the increase of I_0 is significant and the participation of a high temperature TL may be suspected, since the intensity of this TL peak increases linearly with the irradiation time.

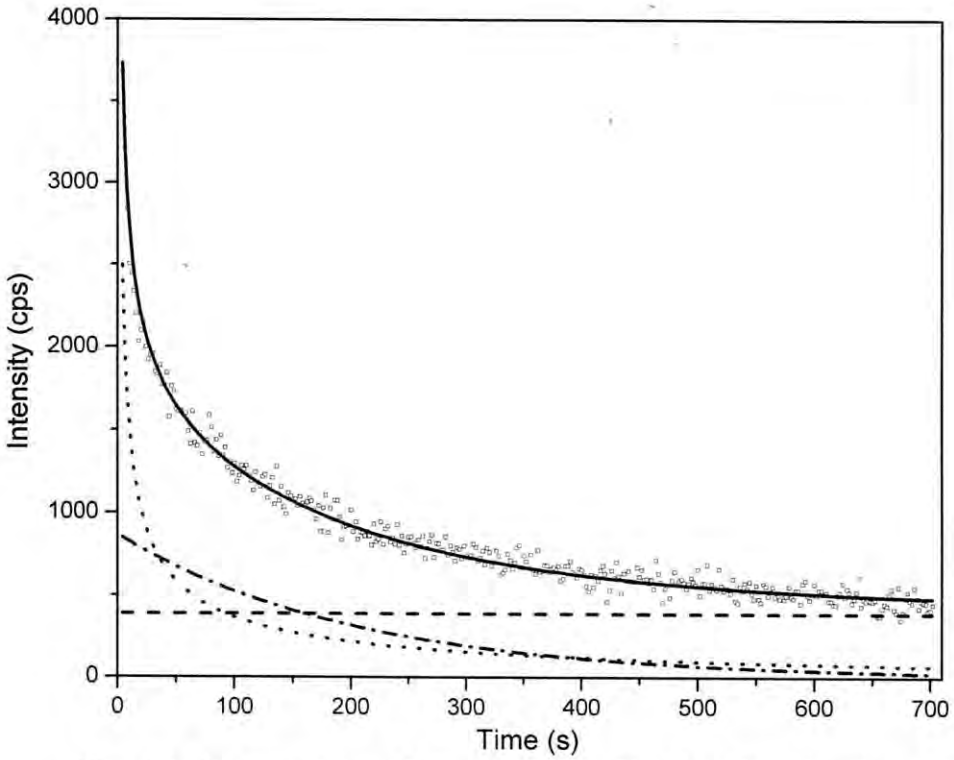

Fig. 4.6. Fitting of the AG decay to t_r = 910 s to the migration AG corrected by the decay of a TL peak (eq. 4.8). The fitting curve (continuous line) fit quite acceptably to the experimental data (points). The contribution of each term in the decay is included: the background (dashed line), the AG decay (dotted line) and the TL decay (dash-dotted line).

To confirm the possible contribution of TL isothermal decays to the AG, the TL glow curve measured immediately following the AG with different irradiation periods could be analyzed. The TL glow curves show a symmetric TL peak centered around 34 K overlapping with the initial rise of a most intense peak centered up to 100 K (Fig. 4.8 A).

To an approximated analysis, we fitted the glow curve in the range 20 – 75 K to the following function:

$$I(T) = I_0 + A_1 \exp\left(\frac{T}{T_1}\right) + A_2 \exp\left(-\frac{1}{2}\frac{(T-T_c)^2}{w^2}\right) \qquad [4.9]$$

where the initial rise of the intense peak is approximated to an exponential growth and the TL peak centered around 34 K to a Gaussian function. The simultaneous fitting of the TL glow curves measured at different irradiation times was possible with the parameters $T_1 = 12.1$; $T_c = 34$, $w = 2.62$, and I_0, A_1 and A_2 as free (see Fig. 4.8). The dependence of parameter A_2 corresponding to the TL intensity of the lowest TL peak, as a function of the irradiation time is shown in Fig. 4.8B. It is clear that the intensity of this TL peak increases linearly with irradiation time, however it does not present the saturated behaviour as expected from eq. [4.7]

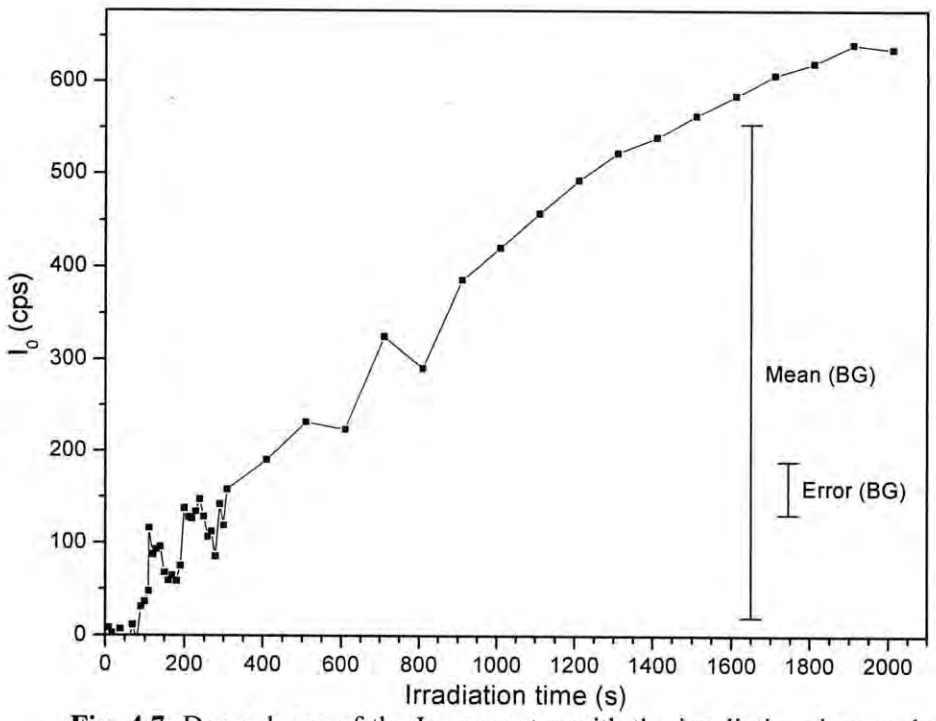

Fig. 4.7. Dependence of the I_0 parameter with the irradiation time to the fitting to a migration mechanisms. The extension of the mean value of the BG at different irradiation times, and the error in BG is also shown.

to a peak that decays appreciably at 20 K. From the A_1 values, the contribution of the exponential term of eq. [4.9] to the AG at 20 K results in a constant value which increases linearly with the irradiation time but 20 times less intense than that showed in Fig. 4.7. Finally, the y_0 parameter was expected as a constant value, however it increases linearly with the irradiation period but with less intensity of that in Fig. 4.7. Possibly, y_0 is due to the contribution of another TL peak at higher temperature.

Therefore, the linear dependence of the I_0 parameter in the AG decay at different irradiation times could be explained by the contribution of the initial rise of several TL peaks centered up to 100 K. However The TL decay overlapping with the AG decay does not correspond to the decay of the TL peak centered around 34 K. If we assume that the mechanism behind AG is from migration of H centers through dislocation lines, then the deviation of the experimental decay curves could not be explained by a TL contribution. Other sources worthwhile to investigate is the effect of the escape of H centers from the dislocation

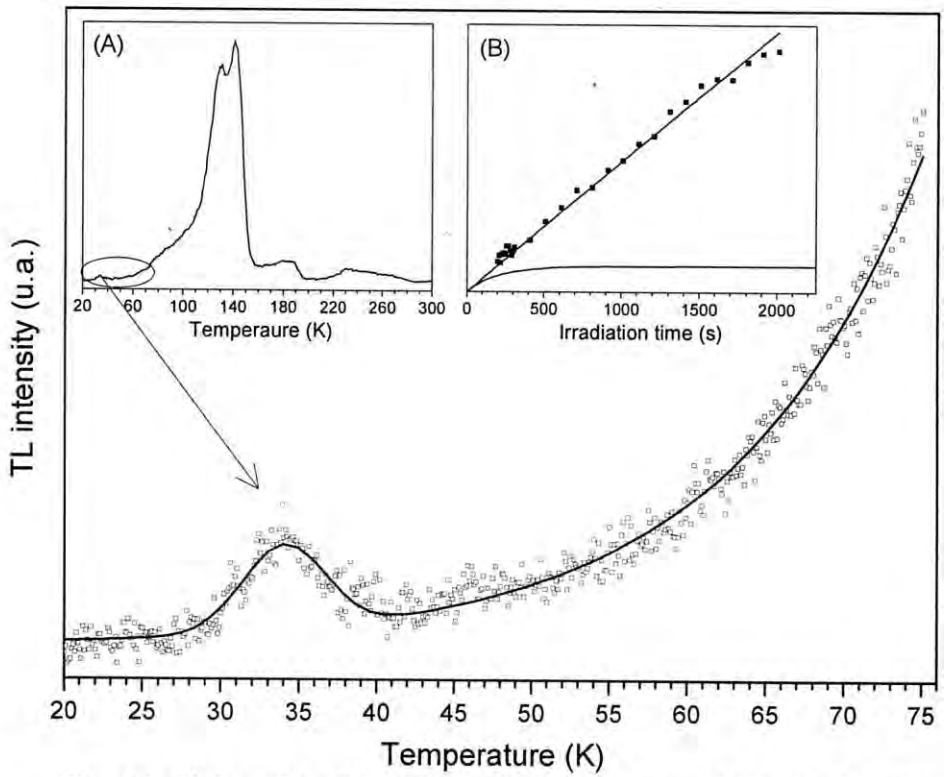

Fig. 4.8. Fitting of the TL timescan in the range 20 – 75 K to the function [4.9] at t_r = 1809 s. The fitting curve (continuous line) fit quite acceptably to the experimental data (points). In (A) the glow curve is shown. In (B) the linear dependence of the fitted parameter A_2 with the irradiation time is compared with the expected dependence given by eq. [4.7].

line.

4.3 Analysis of the TL glow curve in UV-irradiated KCl:Eu at 20 K

A KCl:Eu sample was annealed at 500°C for 30 min and then quickly cooled down to RT. The sample was placed in the setup described in Chapter 3 and irradiated with 225 nm light during 900 s at 20 K. Then the light was blocked and 20 emission spectra were registered during AG decay at the irradiation temperature. After that, the TL emission spectra were registered by heating at 0.1 K/s constant rate until RT taking around 75 emission spectra. The experiment was repeated at different irradiation temperatures in the range 20 – 290 K at 10 K intervals. Before each TL measurement, the sample temperature was cooled down to 20 K. The time for registering each spectra was around 40 s but the non-zero intensity were registered in around 10 s which corresponds to a temperature change of around 1 K.

The TL of UV-irradiated KCl:Eu shows a complex glow curve in the range 20 – 300 K with main bands around 120, 140, 170 and 250 K (Fig. 4.9). The glow curve at different irradiation temperatures were simultaneous fitted by the approximation

$$I(T) = A\, s\, e^{-E/kT} \exp\left[\frac{-s}{\beta}\frac{kT^2}{E} e^{-E/kT}\left(0.9920 - 1.620\frac{kT}{E}\right)\right] \qquad [4.10]$$

where β = 0.1 the heating rate, A the amplitude, E the activation energy and the pre-exponential factor $ln\ s$ (see Appendix 3 for details). The glow curve in the temperature range 100 – 300 K was decomposed in 9 peaks (Table 4.1). At temperatures below 100 K, the TL intensity increases monotonically without any peak structure being difficult to isolated the different participating peaks.

The approximation [4.10] was initially proposed to the analysis of the glow curves at temperatures higher than RT and not at low temperatures. To verify the correct application of this approximation at low temperatures, the activation energies E obtained by the glow curve fitting method were compared to that obtained by the "initial rise method". The latter method

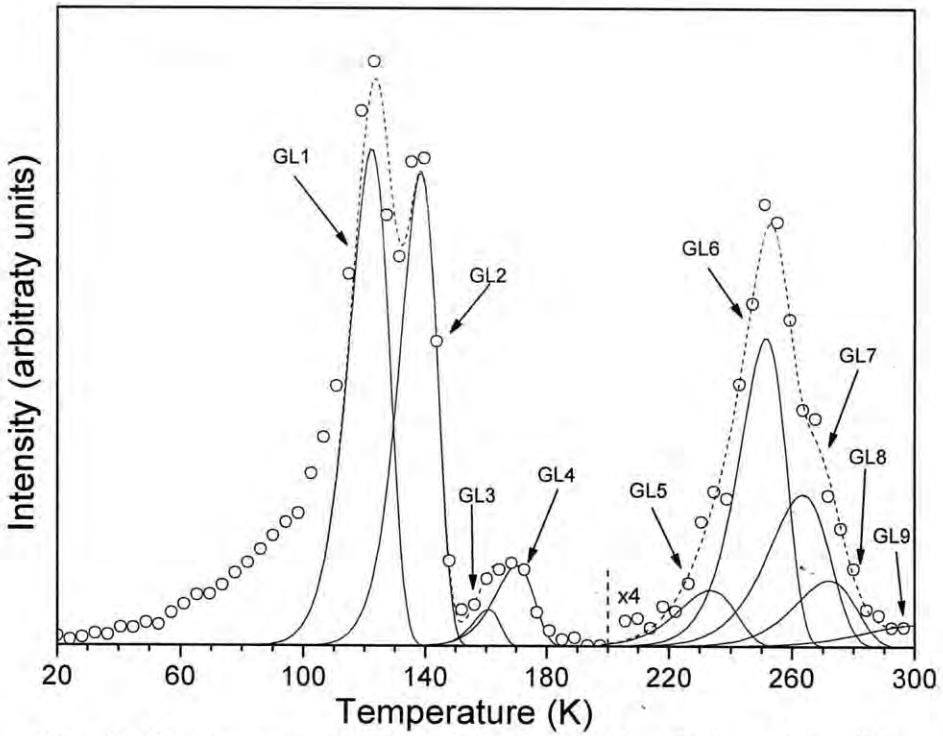

Fig. 4.9. TL glow curve of a KCl:Eu crystal irradiated with 225 nm light at 20 K (open circles). The fitting to 9 glow peaks in the range 100 – 300 K is also shown (continuous line to the single peaks and dashed line to the convolution curve). The curves are scaled by a factor x4 to temperatures up to 200 K.

is based on the assumption that at the low temperature side of a TL peak the intensity increases exponentially with the temperature:

$$I(T) = C \exp[-E/kT] \qquad [4.11]$$

Then, the graph of *ln I* versus $1/T$ would be a straight line of slope $-E/kT$ from which the activation energy E could be found. This method can be effectively used when the glow curve initiates as a single peak and not as the overlapping of several peaks. Exploring our glow curves at different irradiation temperatures, we found that this method can only be applicable in the glow curve after irradiation at 120 K where the initial peak corresponds to GL2. Then, the linear fitting of *ln I* vs *1/T* results in an activation energy $E = 0.2687 \pm 0.0090$ eV. This value is closed to that observed in the fitting of peak GL2 (table 4.1). No more "initial rise curves" at different irradiation temperatures could be related to a single glow peak, however the results to GL2 suggests that the approximation [4.11] could be useful to estimate the peak parameters also at temperatures below RT.

A tentative assignment of the different TL peaks could be proposed by comparing the maximum temperature of the peaks with that previously reported in TL experiments (at 0.14 K/s) in X-ray irradiated KCl crystals [Jimenez 1979]. TL peaks centered at 100, 112, 155, 170, 207 and 250 K were associated to electrons released from some trap and a peak at 195 K to hole released from V_k centers. TL peaks at 100, 120, 165, 200, 220, 230, 275 and 290 K had associated a F center annealing step and they were assigned to the recombination with F centers of mobile interstitial halogen atoms thermally released from traps. Then, some of the TL glow peaks that we found could be related to the thermally release of interstitial halogen atoms and other ones to released electrons (table 4.1). It will be useful to complement the TL experiments with Thermally Stimulated Current data to confirm the previous assignment. At TL temperatures below 100 K, we could not deconvolute the TL glow curve however, we found that at irradiation temperatures from 20 to 60 K the glow curve in this region does not change significantly. This result suggests that only a single phenomena is involved and not a

Glow peak	***E* (eV)**	***ln s***	**T_M (K)**	**Mobile entity thermally released from trap**
GL1	0.1891	13.71	120	interstitial halogen atoms
GL2	0.2618	17.79	137	---
GL3	0.4939	31.84	162	interstitial halogen atoms
GL4	0.3801	21.73	171	electrons
GL5	0.4861	19.60	234	interstitial halogen atoms
GL6	0.7041	28.15	251	electrons
GL7	0.5827	21.04	263	---
GL8	0.6275	22.16	272	interstitial halogen atoms
GL9	0.4936	14.09	300	----

Table 4.1. Parameters of the fitted glow peaks: activation energy (E) and pre-exponential factor ($ln\ s$). The maximum temperature of each peak (T_M) was estimated from Fig. 4.9. The table includes the tentative assignment related to the mobile entity releases at each peak [Jimenez 1974].

collection of single peaks. A more detailed study in this region of temperatures will be necessary to confirm this hypothesis.

Thus, the tentative assignment of the TL peaks confirms the formation of stable color centers in KCl:Eu crystals irradiated with low energy UV light of low energy. The recombination of these centers is satisfactorily explained by the H center migration model where the H center thermally released at different temperatures, migrate until the F center position. Once at the F center position, the F and H center recombine. This recombination could be direct or through a tunneling process of the electron from the F center to the H center. In pure KCl, F–H tunneling followed by α–I recombination is a non-radiative process [Shluger 1981] however, the presence of the impurity in the vicinity could possible assists in a radiative recombination.

4.4 Conclusions

In this chapter we analyzed the AG and TL considering two possible models for the F–H center recombination. In one model the recombination is through a tunneling process of the electron of the F center to the H center followed by a α–I recombination. Although this kind of recombination does not lead to luminescence in pure KCl, it is assumed that in the presence of the Eu impurity this process could be luminescent. The kinetics of the afterglow is assumed to be due to the tunneling of electrons of the F center to a nearby H center. The α–I center recombination is assumed to be too fast to contribute to the kinetics. A detailed analysis of the decay according to this model shows that good fits are possible if one neglects any contribution of isothermal decay from the broad TL feature between 50 K and 100 K. Furthermore one has to adapt the tunnel parameters as calculated by Shluger. The weak point in this model is the assumption of a radiative α–I recombination in the presence of the Eu impurity. No extra evidence for this exists. For example there exists no evidence for TL in the temperature range of α–I recombination for KCl:Eu.

In our model of migrating H centers through dislocation lines, the tunneling does not contribute to the AG decay kinetics and hence no assumption about the radiative character of α–I recombination has to be made since one may assume direct F–H center recombination.

The analysis of the AG decay according to this model reveals two additional components. One of them is constant and could be reasonably accounted for by isothermal decay of the complex TL feature between 50 and 100K. The other component was during the analysis supposed to be due to an isothermal decay of a low temperature TL peak. Measurements of TL, however, could not confirm this. Maybe this component is due to that the H center has a possibility to escape from the dislocation line during its migration. When the H center escapes from the dislocation line it would be removed from the AG process leading to a faster AG decay. Apart from these details the most questionable aspect of our model is the necessary participation of dislocations in the AG decay kinetics. The following chapters are dedicated to the validity of this concept.

CHAPTER 5:

PARTICIPATION OF THE Eu PRECIPITATES IN THE PL, AG AND TL IN UV-IRRADIATED KCl:Eu AT 20 K

In the previous chapter, we showed the existence of a similarity between the emission-excitation spectra of the AG and the TL in Eu-doped alkali halides which were heated at 500°C for around 30 min following a fast cooling at RT. However, it is known that the emission spectra in Eu-doped alkali halides depends strongly on the thermal treatment. This fact has been related to the presence of different precipitated states of the Eu impurity. At this moment, there is little attention paid to the role played by the different Eu precipitates in the AG and TL phenomena [Aguirre 1988]. For this reason, we dedicated this chapter to the study of the photoluminescence (PL), AG and TL in KCl:Eu crystals submitted to different thermal treatments which are known to produce several Eu precipitates. In section 5.1, we reproduce the reported absorption spectra of a KCl:Eu sample after different thermal treatments. In section 5.2, we analyze the reported study about the deconvolution of the emission spectra at RT. A better discrimination of the participating emission peaks would be obtained if the PL experiments were run at low temperature. For this reason, we present a detailed analysis of the decomposition of the emission spectra at 20 K. In section 5.3 we study the participation of the different emission bands in the AG and TL of a KCl:Eu sample submitted to different thermal treatments. The creation spectra of the AG and TL of each of the emission bands are presented. The AG decay and the TL glow curve of the different bands are also included. Finally, section 5.4 is dedicated to the discussion of the experimental results. Some of the results presented here were published elsewhere [Alvarez-Garcia 2005].

5.1 Optical absorption at RT

A KCl:Eu crystal was cleaved in samples of about 7 x 5 x 1.5 mm and submitted to different thermal treatments: (A) stored at RT for several years, (B) heated at 500°C for 1 h followed by a fast-cooling to RT and (C) aged at 200°C for about 300 h. After each thermal treatment, the RT optical absorption spectrum was measured in a spectrometer (PERKIN ELMER, Model Lambda 19). Fig. 5.1 shows that the high-energy absorption band of spectra (A) and (B) are in the same position but the low-energy band of (A) is slightly shifted to lower energy giving a large value of the 10 *Dq* splitting respect to (B). In this way, López *et al* [Lopez 1980] argued that the precipitated phase of Eu^{2+} in KCl, is stronger than that at the site occupied by the impurity ion after quenching from high temperature, being the expected behavior for a precipitated Suzuki phase. After aging at 200°C the high-energy absorption band moves to low energy and the low-band keep in position, resulting in a smaller 10 *Dq* value for (C) than that for (A). Rubio *et al* [Rubio 1981] argued that this result indicates that the structure of the precipitated phase which nucleates at 200°C is different to that precipitated after long aging at RT.

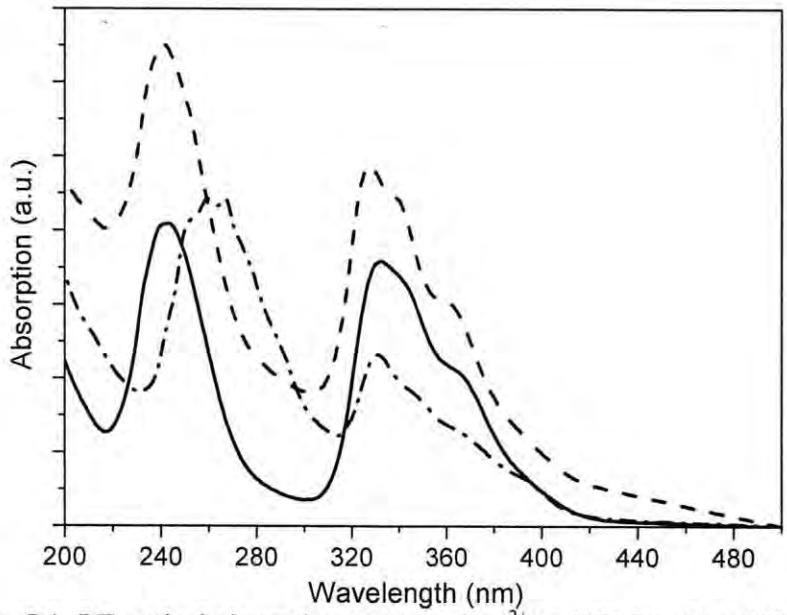

Fig. 5.1. RT optical absorption spectra of Eu^{2+} in KCl:Eu after different annealing processes: (A) at RT for several years (solid curve), (B) at 500°C for 1 hour (dashed curve), and (C) at 200°C for about 300 hours (dash-dotted curve).

5.2 Photoluminescence at different thermal annealings

In the previous section it has been shown that the absorption spectrum of a KCl:Eu crystal depends on the thermal treatment of the sample. In this way, it has been reported that the emission spectra at RT is also altered by the thermal treatment. In this section, we analyze the different emission spectra observed in KCl:Eu samples after different thermal annealing. We decompose the emission spectra in a series of Gaussian peaks each one presumable given by a different precipitated state of the Eu impurity. The analysis is initiated at room temperature but we realize that a better discrimination of the different peaks under the emission spectrum is achieved if the experiment temperature is down at 20 K.

5.2.1 PL emission at RT

The PL excited with UV-visible light was measured at RT for a KCl:Eu sample after it was exposed to the previous thermal treatments (A, B and C). For comparison, the PL for another sample which was stored at RT for years and aged at 200°C for around 850 h, was also included (D). The typical emission spectrum observed for each treatment is shown in Fig. 5.2. These spectra can be compared with those reported by López *et al* and Rubio *et al* [Lopez 1980, Rubio 1981]] for a KCl:Eu crystal exposed to similar thermal treatments. The parameters of their peaks are summarized in Table 5.1. The peak assignment proposed by the authors and the thermal treatment in which they participated are also included. The peak widths which were not reported for the KCl:Eu crystal, are taken from the peaks assigned to similar Eu-configurations in the NaCl:Eu system.

Exploring the emission spectra at different irradiation wavelengths, they seems to be formed by a fixed number of emission bands which participate with different intensity. To find the emission bands composing the emission spectra, the non-linear square fitting option of commercial software (Origin 7.0) is used to fit the spectra to a set of Gaussian bands. The fitting program is based on the Levenberg-Marquardt algorithm and enabled a full control of the fitting process. The function used for individual bands is:

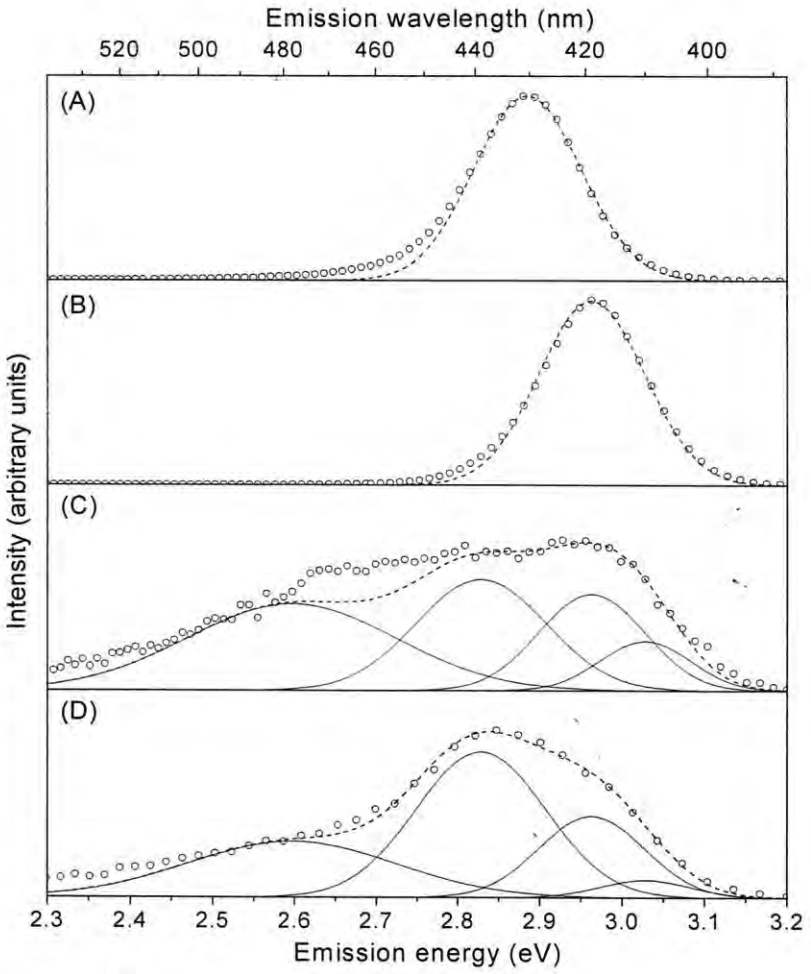

Fig. 5.2. RT emission spectra of Eu^{2+} in KCl:Eu irradiated with 325 nm light in the different thermal treatments (A), (B), (C) and (D). Open circles represent the experimental data; continuous lines the Gaussian peaks and dashed lines the convolution fitting curve.

$$y(x) = y_0 + A\exp\left[-\frac{(x-x_c)^2}{w^2}\right] \qquad [5.1]$$

where x is the emission energy, y the intensity, y_0 the offset intensity, A the peak amplitude, x_c the peak center position and w is related to the Full-Width at Half Maximum (FWHM) of the peak by

$$FWHM = 2\sqrt{\ln 4}\, w \qquad [5.2]$$

For convenience, we defined the peak intensity as:

$$I_i = (A_i - y_0) \times w_i \qquad [5.3]$$

To determine the position and width of the emission Gaussian peaks, those peaks which were more easily identified in some spectrum are fitted first. Then, different spectra with intensities of the same order are fitted simultaneously allowing small variations of the previously identified peaks and looking for additional peaks. After checking that most spectra were fitted by the selected Gaussian peaks, their positions and widths were fixed. Then, each spectrum was fitted apart to find its peak maximum intensity and its background level. Sometimes, extra peaks were necessary, however they were not taken into account because they were too weak or too close to another peak to be fitted. In any case, small variations of the peak centers or widths did not change significantly their intensities.

The decomposition into Gaussian peaks of our emission spectra was initiated with the reported data (Table 5.1). In treatment (A), the emission was reported as a single peak with its center at 427 nm and a width of 0.17 eV while our experimental data fitted to a peak centered at 431 nm and 0.16 eV wide. By comparing the experimental data and the best fitting curve, it can be observed that the emission was slightly antisymmetric at the low-energy side (Fig. 5.2A). This mismatching could also be observed in the previously reported spectra; however the authors did not discuss it [Lopez 1980]. In treatment (B), the reported emission was a peak at 419 nm and 0.15 eV wide which coincided with the parameters of our fitting. In this case,

Center (nm)	**FWHM (eV)**	**Assignment**	**Thermal treatment**
478	0.30*	Metastable precipitated $EuCl_2$-like plate zones parallel to {310} plane of the matrix lattice	(C)
439	0.22*	Metastable precipitated $EuCl_2$-like plate zones parallel to {111} plane of the matrix lattice	(C)
427	0.17	Suzuki precipitated phase	(A)
419	0.15	Isolated Eu^{2+}-v_c dipoles and initial products of aggregation (dimers)	(B), (C)
410	0.13*	Stable dihalide phase $EuCl_2$	(C)

Table 5.1. Emission peaks reported for the RT photoluminescence for KCl:Eu (*data reported for NaCl:Eu) [Lopez 1980, Rubio 1981].

the non-symmetry of the curve was less evident. In (C), the reported emission was composed of the previous peak at 419 nm and three peaks at 410 nm, 439 nm and 478 nm. Beginning with the widths reported for the NaCl:Eu system: 0.13 eV, 0.22 eV and 0.30 eV, respectively, the fitting was improved by allowing small variations of the widths to 0.19 eV, 0.20 eV and 0.32 eV. The latter width laid to higher values, because of the presence of an extra peak at the low-energy side of the spectrum. It was clear that an extra peak around 460 nm should be included to obtain a good fit. In treatment (D), the spectra were similar to that in (C), with a better definition of the peak at 439 nm and without including the extra peak around 460 nm.

This analysis demonstrates a small disagreement between the reported emission spectra and our experimental data except for treatment (B). This may be due to slightly different thermal conditions during the aging at RT (A) or at 200°C (C, D). In any cases, the mismatching of the fitted band in (A) indicates that the peak decomposition implies more peaks which were not previously identified.

5.2.2 PL emission at 20 K

A single sample is submitted to the thermal treatments previously mentioned and then mounted in the experimental setup described in Chapter 3. The sample was irradiated with UV-visible light in the range 400 – 200 nm in descending order and then the emission spectrum was registered. Before the analysis of the spectra, the data were corrected as mentioned in section 3.3.

Typical emission spectra for each thermal treatment at 20 K are shown in Fig. 5.3. These spectra were measured for the same samples used in the PL experiment at RT. Unlike spectrum (A) at RT, the spectrum (A) at 20 K shows a main band around 429 nm and a shoulder around 416 nm. Furthermore, the long tail at lower energy implies the participation of more bands. Spectrum (B) presents a dominating band around 416 nm and some other peaks at lower energy which gives a non-symmetric character to the curve. Spectrum (C) shows two bands around 416 nm and 441 nm, possibly another band between them and at least one more at low energy. Spectrum (D) shows the same bands as (C) but with a higher intensity of bands around 416 nm and 441 nm.

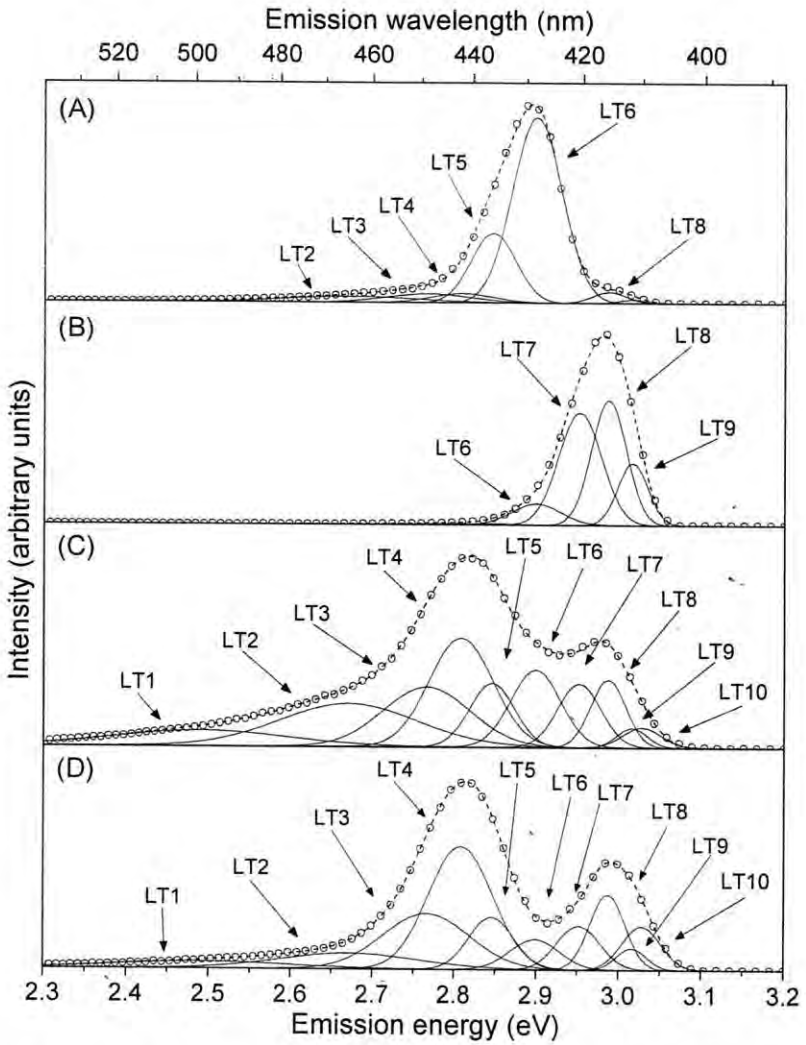

Fig. 5.3. Emission spectra at 20 K in KCl:Eu irradiated with 325 nm light in different thermal treatments (A), (B), (C) and (D). Open circles represent the experimental data, continuous lines the Gaussian peaks and dashed lines the convolution fitting curve. The decomposition into 10 Gaussian peaks was included.

The identification of the Gaussian peaks which fit the emission spectra was initiated by analyzing the bands which dominates in each thermal treatment. The Gaussian peaks were labeled by the characters "LT" from "low temperature" and a number increasing with the central peaks energy. Then the non-symmetric band around 429 nm in (A) was split in two peaks: LT5 and LT6. In (B), the band around 416 nm was fitted by three peaks: LT7, LT8 and LT9. In (C), the band in the low energy tail was decomposed in two widen peaks: LT1 and LT2. In (D), the main non-symmetric band around 441 nm was fitted by two peaks LT3 and

Band	Peak	x_c (eV)	w (eV)	A
BD1	LT1	2.490 ± 0.050	0.103 ± 0.018	0.430
	LT2	2.670 ± 0.030	0.084 ± 0.020	0.895
BD2	LT3	2.766 ± 0.024	0.053 ± 0.003	0.377
	LT4	2.8076 ± 0.0018	0.039 ± 0.004	0.708
BD3	LT5	2.846 ± 0.018	0.027 ± 0.007	1
BD4	LT6	2.899 ± 0.009	0.030 ± 0.006	1
BD5	LT7	2.952 ± 0.018	0.026 ± 0.020	0.549
	LT8	2.987 ± 0.066	0.021 ± 0.005	0.692
	LT9	3.0164 ± 0.0016	0.018 ± 0.001	0.263
BD6	LT10	3.028 ± 0.020	0.023 ± 0.015	1

Table 5.2. Fitting parameters of the Gaussian peaks of the PL emission at 20 K in KCl:Eu. Peak parameters x_c and w are defined by the fitting Gaussian function: $y(x) = A \exp(-(x-x_c)^2/2w^2)$ where x is the photon energy in eV. The grouping of the 10 Gaussian peaks into 6 emission bands is included. The amplitude A of each peak (LT) is taken such that the convoluted band amplitude (BD) is unity.

LT4. Finally, in (C) and (D) a peak at the high energy side was included (LT10). Therefore, the fitting was completed with 10 Gaussian which were all essential during the fitting of the spectra observed in 200 excitation wavelengths (200 – 400 nm) for the four thermal treatments. Peak parameters are listed in Table 5.2.

During the fitting procedure, it was appreciated that some peaks seem to keep a constant ratio for the different spectra corresponding to a treatment. This fact could be interpreted as an excessive spectra deconvolution. Possibly some peaks were not completely independent and constitute a more complex emission band. To verify this, the intensities of two adjacent peaks were compared at different excitation wavelengths for each thermal treatment. The results are shown in Fig. 5.4.

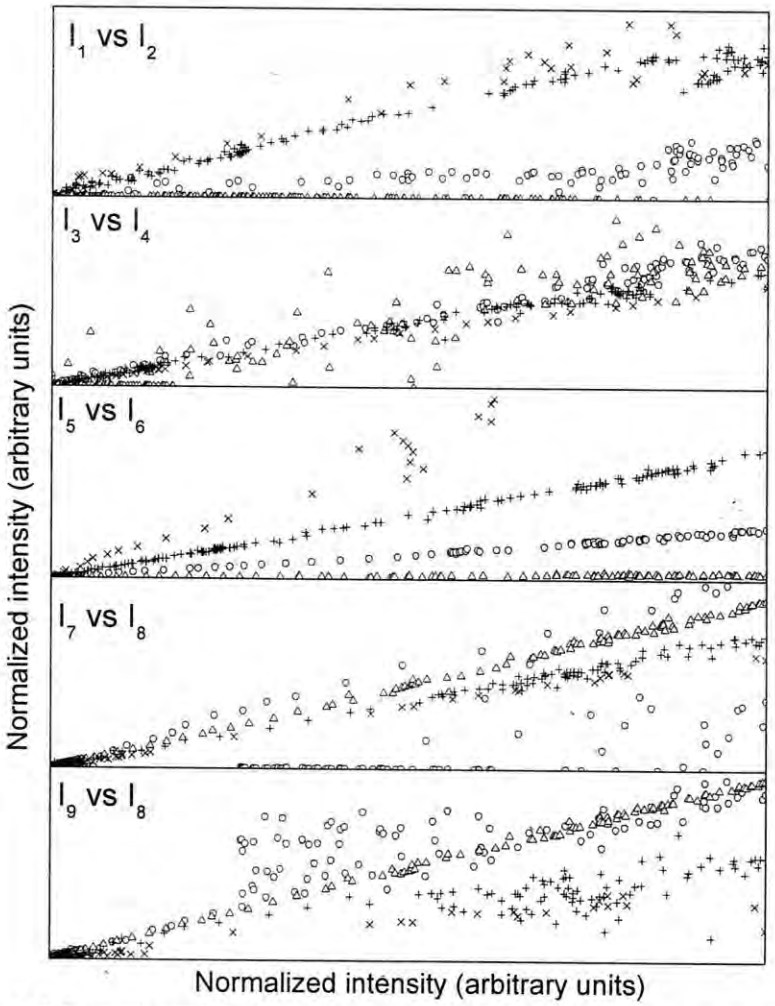

Fig. 5.4. Intensity ratio between two neighbor peaks fitted independently. Each point is for a different excitation wavelength. For each of the thermal treatments a different symbol is used: open circle for (A), open triangle for (B), vertical cross for (C), and oblique cross for (D).

Intensity I_1 was clearly linear with intensity I_2 for treatment (C), where these peaks dominated the spectra and also in (D) but with higher dispersion of the points. In (A) the linear relation had a lower slope. Intensities I_3 and I_4 presented the same linear relation for all treatments. In (B) the points were more dispersed due to fitting troubles by the overlapping with more intense peaks (LT5 and LT6). Intensity I_5 was linear with I_6 for all treatments; although in (D) the data were highly dispersed. However, the proportionality relation between these intensities was different for each thermal treatment. Intensity I_7 is clearly linear with intensity I_8 in treatment (B), where the peaks dominated, and it was also linear in the other treatments, but with higher dispersion. In treatment (A) this dispersion was high due to the

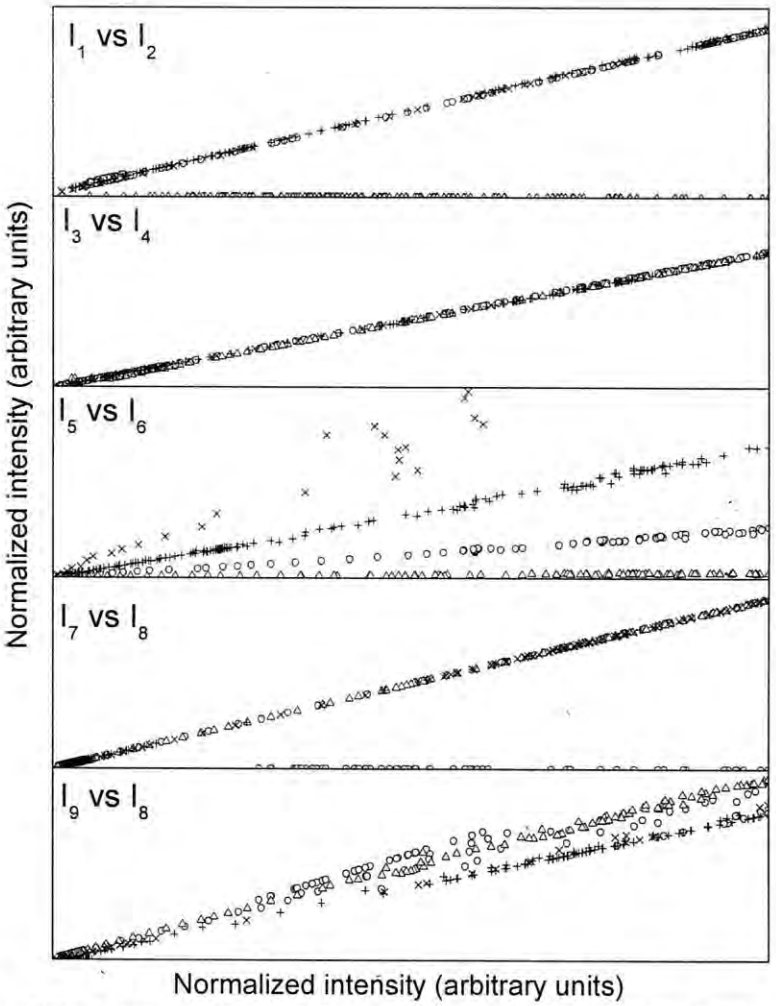

Fig. 5.5. Intensity ratio between two neighbor peaks fitted with dependent intensities. Each point is for a different excitation wavelength. For each of the thermal treatments a different symbol is used: open circle for (A), open triangle for (B), vertical cross for (C), and oblique cross for (D).

overlapping with the high-energy tail of peak LT6. Intensity I_9 was linear with intensity I_8 in (B) and more dispersedly in the other treatments. Again, the dispersion in (A) was due to the overlapping with peak LT6, and in (C) and (D) to the presence of peak LT10.

The dispersion of the points from the linearity could be due to a non-perfect fitting of the peaks which not dominate in a thermal treatment and are disturbed by the overlapping with other more intense ones. To confirm this, the fitting process was done again using the same parameters but introducing a proportionality constrain between the intensities I_1 vs. I_2, I_3 vs. I_4, I_7 vs. I_8 and I_9 vs. I_8. In cases where the convolution fitting curve deviated too much from the

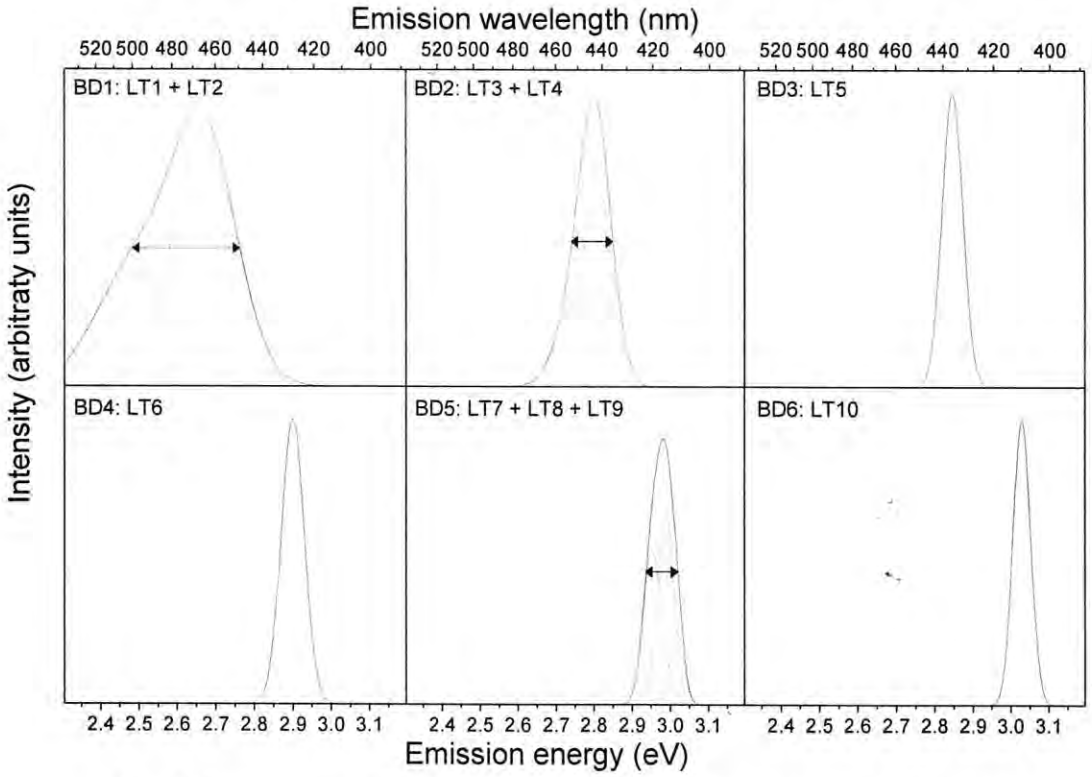

Fig. 5.6. Grouping of the ten Gaussian peaks into six emission bands. Line with arrows represents the estimated FWHM for the non-Gaussian bands.

experimental data, the condition causing the effect was disabled. The new relations are shown in Fig. 5.5.

For the $I_1 - I_2$, $I_3 - I_4$ and $I_7 - I_8$ pairs, the proportionality condition was kept in most of the emission spectra for the four thermal treatments. For the $I_9 - I_8$ pair, the fitting of these intensities was disturbed by the presence of peak LT10 which overlapped with peak LT9 in treatments (C) and (D) and in treatment (A) by the distortion of the intense peak LT6 (see Fig. 5.3). Therefore, we conclude that peaks LT1 – LT2, LT3 – LT4, LT7 – LT8, and possibly LT9 – LT8 are not independent peaks and can be grouped together forming complex emission band. Then, the emission spectra are composed of six independent bands of which some of them are formed by two or more Gaussian peak (Fig. 5.6). The grouping of the 10 Gaussian peaks in six emission bands is resumed in table 5.2. The table also includes the amplitude A of each peak (LT) to construct the convoluted band (BD) with amplitude equal unity. Peaks LT5 and LT6 are not completely independent but keep a different relation in each thermal treatment which we can not account for.

5.2.3 PL excitation at 20 K

The excitation spectra of the PL was obtained after fitting 200 emission spectra at different excitation wavelengths (range 200 – 400 nm) and then following the intensity of each emission band (Fig. 5.7, solid line). To demonstrate the reproducibility of the curves, the excitation spectra for a different set of samples which were used in the AG/TL experiment are also included (Fig. 5.7, open circles). The excitation spectra of a particular emission present slightly variations for the different thermal treatments because the overlapping of nearby peaks slightly alters the fitting process. Therefore, the PL excitation spectra of each emission band showed in Fig. 5.7 are for the treatment where the emission has a predominant role.

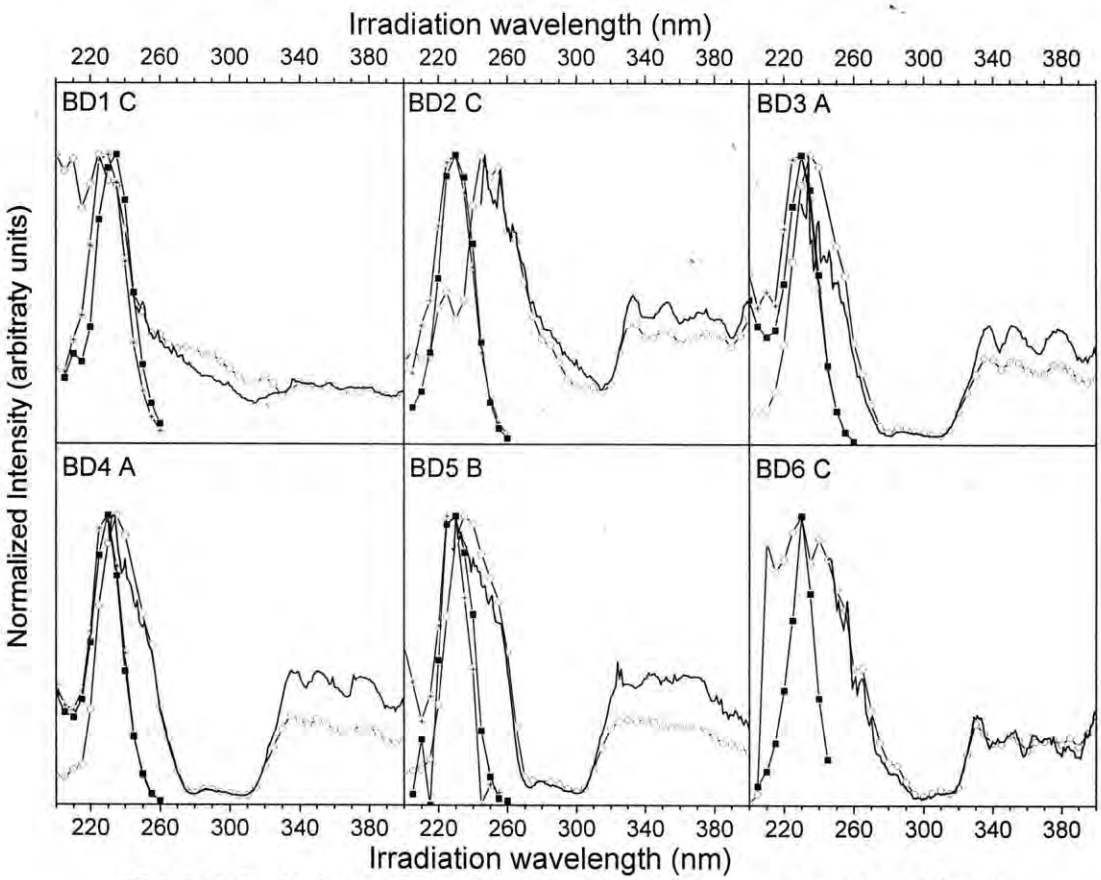

Fig. 5.7. Excitation spectra of the PL and creation spectra of the AG and TL after exposed to UV-visible light at 20 K for the six emission bands in the thermal treatment where they dominate. Open circles represent the PL, solid square the AG and stars the TL for the same sample. Solid line represents the PL in a different sample for comparison. The excitation spectra were corrected by the emission of the irradiation lamp and the response of the detection system.

The PL excitation spectra of almost all emission bands shown in Fig 5.7 present the two well-known bands related to transitions between the ground state and the excited states E_g (200 – 270 nm) and T_{2g} (320 – 400 nm) of the Eu^{2+} ion in a cubic crystal field. The high energy band in the excitation spectra seems to be composed of at least two peaks around 230 nm and 260 nm. However, the excitation spectrum of BD1 only presents the 230 nm peak suggesting that this peak as well as BD1 is not related to the Eu^{2+} ion but possibly to a nearby structural defect. Therefore we suppose that only the 260 nm peak corresponds to the excitation to the T_{2g} state. Emission BD2 was clearly identified in treatment (C) and according to the conclusions of Rubio *et al* [Rubio 1981] would be assigned to the metastable precipitated $EuCl_2$ phase. Emission bands BD3 and BD4 dominate in (A). Band BD3 has a central position close to one of the metastable $EuCl_2$ precipitated phases previously reported, but its width is too narrow. In any case, the relative great separation of the Eu excitation bands suggests an assignment to some Eu precipitate. Based on its central position, width and dominating presence in the well-aged crystal at RT, it is tempting to assign band BD4 to the Suzuki precipitated phase. However the thermal solvation of this phase occurs at temperatures lower than 150°C [Lopez 1980] which contradicts the presence of band BD4 after treatments (B) and (C). A possible explanation for this is that band BD4 in treatments (B) and (C) is associated with trimers of which the emission is similar to that of the Suzuki phase as suggested by Martinaga *et al* [Martinaga 1988]. Although trimers are also unstable at temperatures around 150 – 200°C, they could be formed from dipoles and dimers during the not too-fast cooling down to RT because trimers are formed considerably faster than the Suzuki phase. Emission band BD5 dominates in treatment (B) where it is known that the Eu impurities are in the Eu-v_c dipole configuration, clearly giving the assignment of the band. It also appears in other treatments indicating that the dipoles configuration was not completely lost by ageing. Emission band BD6 appears in (C) and its central position around 410 nm suggests its association with a stable $EuCl_2$ phase. Table 5.3 compares our data and assignments of the PL emission bands at 20 K with that of the PL emission bands at RT previously reported.

In conclusion, the study of the PL at 20 K reveals more details about the changes occurring in the Eu-impurities during the different thermal treatments than the study of the PL at RT as in previously reported works (see section 1.3.2).

Band	Center		FWHM (eV)	Dominate in treatment	Tentative assignment	Ref.
	(nm)	(eV)				
BD1	468	2.654	0.282	C	Structural defect nearby Eu ion	This work
	478	2.597	0.30*	C	Metastable $EuCl_2$ phase	Rubio 1981
BD2	443	2.80	0.109	C	Metastable $EuCl_2$ phase	This work
	439	2.83	0.22*	C		Rubio 1981
BD3	436	2.846	0.064	A	Some Eu phase	This work
BD4	428	2.899	0.071	A	Suzuki phase and / or Eu–v_c trimers	This work
	427	2.908	0.17	A	Suzuki phase	Lopez 1980
BD5	417	2.981	0.083	B	Eu–v_c dipoles and dimers	This work
	419	2.963	0.15	B		Lopez 1980
BD6	410	3.028	0.054	C	Stable $EuCl_2$ phase	This work
	410	3.028	0.13*	C		Rubio 1981

Table 5.3. Assignment of the 6 emission bands of KCl:Eu at 20 K. Band centre in eV- and nm-units and the FWHM value are shown for each band. The thermal treatment in which each band dominates are included (A: several years at RT, B: 1 h at 500°C and C: 300 h at 200°C). Previously reported data for the PL at RT are included for comparison (*widths not reported for the KCl:Eu crystal where taken from similar identified peaks in the NaCl:Eu).

5.3 AG and TL after UV-irradiation at 20 K at different thermal annealings

After the previous detailed analysis about the different bands composing the PL emission spectra of a KCl:Eu crystal submitted to different thermal treatments, in this section we search the participation of the different emission bands in the spectra of afterglow and thermoluminescence. Then, after submission to each of the thermal annealing treatments, a KCl:Eu sample was mounted in the setup previously described (Chapter 3) and irradiated with monochromatic light at 20 K for around 900 s. Then the irradiation light was turned off and 20 AG emission spectra were registered (one per 32 s). After waiting 300 s to complete the decay of the AG, the sample was heated at constant rate (0.1 K/s) until 300 K recording 74 TL emission spectra (one per 3.8 K). The experiment was repeated for different excitation wavelengths observing that the AG and TL were only produced in the 200 – 260 nm range. At longer irradiation wavelengths it was not observed an AG neither TL signal.

5.3.1 Emission of AG and TL

Fig. 5.8 compares the emission spectra of the PL, AG and TL observed in a KCl:Eu sample submitted to the treatments (A), (B) and (C). The fitting of the AG and the TL spectra was possible with the 10 Gaussian peaks identified in the PL with the proportionality conditions between the paired peak intensities. Some spectra of TL in treatments (C) did not fit correctly with the 10 Gaussian peaks for a small number of temperatures around the maximum at 130 K. To obtain satisfactory fits in this region an extra peaks below peak LT1 and one between peaks LT2 and LT4 would be necessary. For the sake of simplicity this detail is ignored in the present analysis. Figure 5.8 includes the decomposition of the AG and TL spectra in the six emission bands.

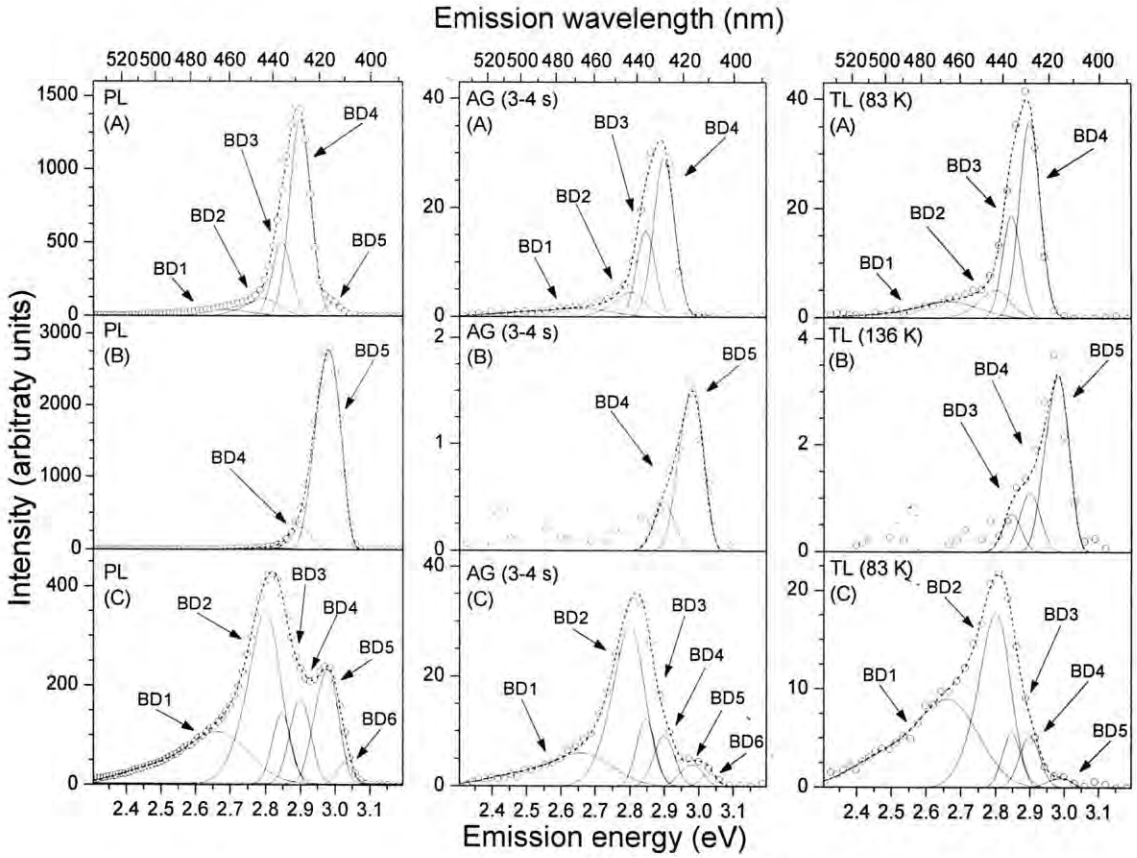

Fig. 5.8. Emission spectra at 20 K of PL exposed to 325 nm light, and of AG and TL induced by 235 nm light in KCl:Eu after different thermal treatments (A: several years at RT, B: 1 h at 500ºC and C: 300 h at 200ºC). The AG spectra correspond to 3 – 4 s after the end of the irradiation and TL spectra to an intermediate temperature during the heating at constant rate to RT. Open circles represent the experimental data, continuous lines the individual emission bands and dashed lines the convoluted fitting curve.

Therefore, the six bands identified in the recombination of the PL also take part in the recombination of the AG and the TL. The relative intensities of the different bands are almost similar in the three luminescences in treatments (A) and (B) but not in treatment (C). In general, AG emission is much more intense after treatments (A) and (C) than after treatment (B). This is partly due to that the AG production is more efficient around aggregates than around dipoles. However also the efficiency of AG production around dipoles seems to increase during the ageing at 200ºC as can be seen as follows. The AG intensity of a band divided by its PL intensity can be taken as a relative measure of the efficiency of AG production. Using this measure it can be calculated that the AG generation of BD5 is about 30

times more efficient after treatment (C) than after treatment (B). The band intensities in the TL emission spectra behave almost similar as those in the AG with respect to the different thermal treatments. However, spectra after treatment (C) show that the contribution of Eu-precipitate bands relative to that of the dipole band is higher in the TL than in the AG.

5.3.2 Excitation of AG and TL

Following the intensity of each emission band at different irradiation wavelengths, the "creation" spectra of the AG and TL were generated (Fig. 5.7). For comparison, each emission band was analyzed at the same thermal treatment used above for the PL, except in emission BD5 where the weakness of the AG and TL signals did not allow a correct fitting in treatment (B) and the data in treatment (C) were used.

Figure 5.7 shows that the "creation" spectra of the AG and the TL are quite similar for the six emission bands and are composed by a single peak centered at 230 nm. The spectra shape is not completely real because the monochromator slit was opened at maximum during irradiation to get enough AG signal, giving a light dispersion around 20 nm which shifted the spectrum to slightly longer wavelengths. In spite of that, the independence of the AG/TL "creation" spectra and the PL one is clear. Therefore, we conclude that the creation of the "stable" defects responsible for the AG and TL luminescence is independent of the excitation of the impurity.

5.3.3 AG time decay curve

The decay curves of the AG emission bands were constructed by following the intensity of each emission at different decaying times. It was observed that the decay curve is identical for all the emission bands in the different annealing treatments and irradiation wavelengths. Fig. 5.9 shows as an example the decay curves of emissions BD1, BD2, BD5 and BD6 in treatment (D) and emissions BD3 and BD4 in (A) after irradiation at 235 nm. Therefore, we conclude that the dynamic of the recombination mechanism is independent of the nature of the emission bands and therefore of the recombination centers.

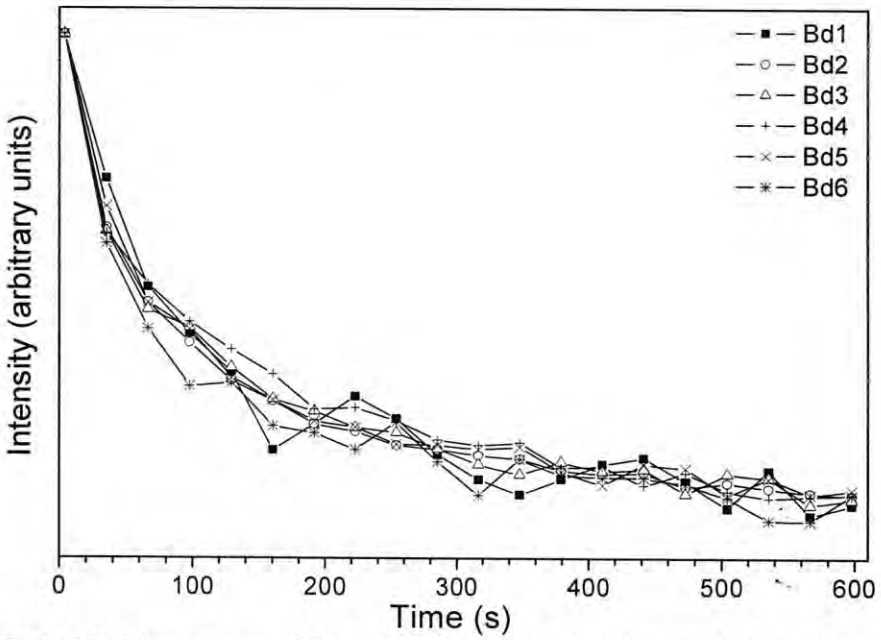

Fig. 5.9. Time decay of the AG emission bands after irradiation at 235 nm. Bands BD1, BD2, BD5 and BD6 in treatment (D) and bands BD3 and BD4 in treatment (A).

5.3.4 TL glow curve

Following the intensity of each band in the emission spectra during the heating ramp, the TL glow curves were constructed. As an example, Fig. 5.10 shows the glow curve of each band in treatment (D) and irradiation at 235 nm. Bands BD5 and BD6 were not included because they were too weak to be fitted. In treatments (A) and (C) the glow curves are slightly different to that in Fig. 5.10 but the changes are common to all emission bands. We conclude that the TL is composed of a continuous set of peaks without preferential recombination in any of the emission bands.

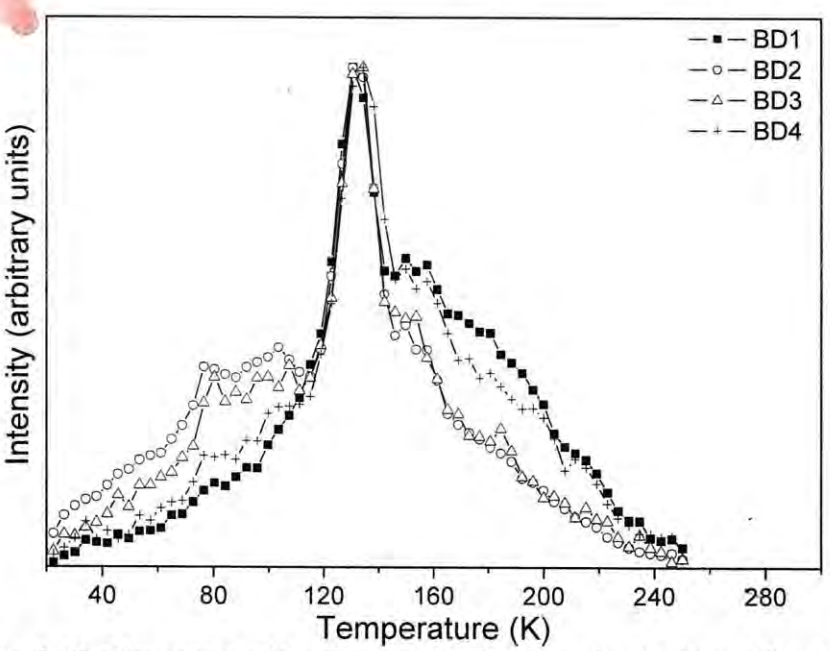

Fig. 5.10. Glow curve of the TL emission bands during heating at 0.1 K/s constant rate after irradiation at 235 nm in treatment (D).

5.4 Discussion

Both AG and TL phenomena imply the migration of the H centre from the creation site. Following the proposed model of Chapter 2, we assume that dislocation lines act as guides for migration, then the defects close to dislocation lines would be more efficient in the production of AG and TL. In view of this, the increase of AG and TL production efficiency around dipoles after aging at 200°C suggests that dislocation lines trap dipoles at that temperature. Furthermore the higher efficiency of aggregates than that of free dipoles suggests that aggregation takes mainly place along dislocation lines. This can be understood if we assume that the trapped dipoles are still free to move along the dislocation lines allowing the aggregation to occur.

The relative higher efficiency of aggregates in TL than in AG compared to the dipoles one could be explained by a difference in the recombination probability. Although the connection between both AG and TL yield and recombination probability is not completely clear, it seems reasonable to assume that lower recombination probability results in relative

higher TL yield because the H centers which do not recombine during AG will contribute to TL. This suggests that the F–H recombination in the presence of an aggregate is lower than in the presence of a dipole. The explanation could be that the initial process of F–H center formation, similar for all Eu-phases, is followed by a relaxation of the "F center"–"impurity defect"–"dislocation line" complex to a different configuration for each Eu-phase presenting different F–H recombination probabilities. The shape of the AG decay is not much affected by changes in the recombination probabilities (see simulation results in section 2.3.2), therefore the observed similarity of the AG decay of each band does not contradict this idea.

In summary, we arise to the following picture of the process responsible for the impurity precipitation and the mechanism of AG and TL: dipoles are trapped by dislocation lines but remain mobile along them. Consequently, the formation of aggregates takes place mainly in dislocation lines. The initial process for the creation of F and H pairs (responsible for AG and TL) is the same for all aggregates and not related to a transition on the Eu^{2+} ion but to one on a nearby structural defect. After the initial process, the H center migrates randomly through the dislocation lines while the F center, the Eu-phase and the dislocation line relax to a configuration, dependent of the Eu-phase involved. The H center may return to the F center and recombine (AG) or may trap at some defect located near or at the dislocation line (leading to TL). The recombination probability of an F–H centers pair is lower in a Eu-configuration of aggregates than of dipoles. This causes a relative lower AG production efficiency for aggregates.

CHAPTER 6:

AG AND TL IN KCl:Eu AFTER DIFFERENT THERMAL AND DEFORMATION TREATMENTS

The experiments in Chapter 5 suggest that aggregation occurs mainly in dislocation lines. This suggestion emerged from our point of view that AG is due to migration of H centers through dislocation lines. Up to now, we have not yet demonstrated the participation of dislocation lines directly. The purpose of this chapter is to search for more direct evidence about the participation of dislocations in the AG as well as in the aggregation process. This is done by increasing the number of dislocations present in the crystal by means of deformation and then performing similar experiments as in Chapter 5.

6.1 Relation between deformation and dislocations

Plastic deformation of a crystal is related to the migration of dislocation lines and the formation of new dislocations [Hull, 1989].

In general, plastic deformation results in the formation of slip steps in the surface of the crystal. The slip is due to the successive displacement of one plane of atoms over another plane. The experimental shear stress for slip is many times lower than that theoretically predicted. This low value could be explained by taken into account the migration of dislocations. This mechanism is illustrated in Fig. 6.1 to an edge dislocation. A small shift of atom 1 relative to atoms 2 and 3 (a) effectively moves the extra half plane from *x* to *y* (b), and this process is repeated as the dislocation continues to glide (c, d). The slip direction is always parallel to the Burgers vector of the dislocation responsible for slip.

The large plastic strain that can be produced in crystals implies that multiplication of dislocations occurs. One of the main mechanisms of multiplication is the "Frank-Read type sources". In an irregular array, some dislocations lie partly in their slip planes and partly in other planes. Consider a dislocation line DD' which lies in a slip plane and it is held at both ends by an unspecified barrier, which may be dislocation intersections, nodes, precipitates, etc (Fig. 6.2). An applied shear stress tends to make the dislocation bow out with a radius of

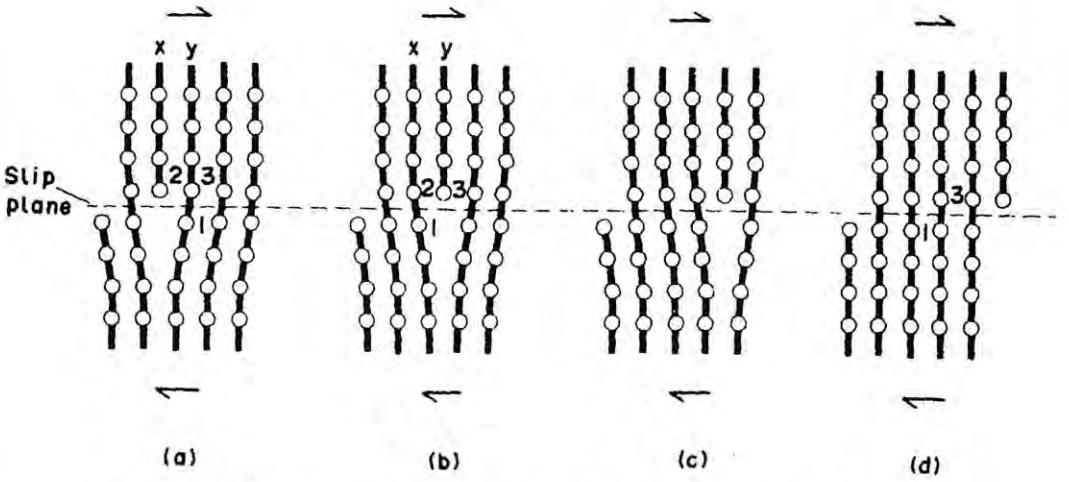

Fig. 6.1. Migration of an edge dislocation: the arrows indicate the direction of the applied shear stress [Fig. 3.4 in Hull 1989].

curvature which depends on the stress. Thus as higher stress, the radius is lower and the line bends until a minimum value is reached (Fig. 6.2b). As the line continues to expand at fixed stress, the radius increases and the dislocation becomes unstable. The subsequent events are shown in Fig. 6.2(c)-(e). The dislocation forms a large kidney-shaped loop. And the segments *m* and *n* annihilate on meeting. This occurs because *m* and *n*, which moves in opposite directions under the same stress, have the same Burgers vector but opposite line sense. The result is a large outer loop, which continues to expand and a regenerated dislocation DD', which repeats the process. Therefore the applied stress produces a high increment in the total length of dislocations in the crystal. In this work, the uniaxial deformation of crystals is used to increase the total length of dislocation lines.

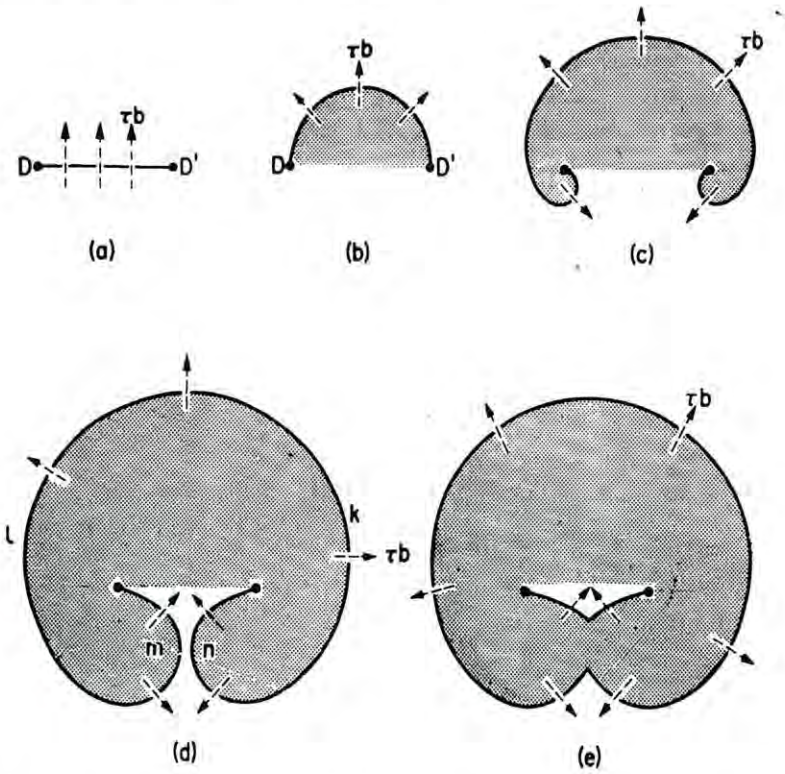

Fig. 6.2. Diagrammatic representation of the dislocation movement in the Frank-Read source [Fig. 8.6 in Hull 1989].

6.2 Experimental procedure

A single crystal of KCl:Eu with a nominal Eu-concentration of 200 ppm was cleaved in samples of typical size around 5 x 5 x 1 mm. PL, AG, TL experiments and thermal treatments at temperatures below 100°C were performed in the setup described in Chapter 3.

The uniaxial plastic deformation was performed with a home-made hydraulic press described in Fig. 6.3. The force acting on the sample could be increased almost linearly at constant rate about 0.1 N/s. The stress is applied along a <100> direction deriving in a shear stress in a {110} slip plane. The deformation is measured as the decrease of the sample thickness along the a direction of the stress using a home-made displacement detector: one end of the a stainless steel bar is resting on a reference point from which the displacement will be measured; the other end is inserted halfway into a coil which form part of an oscillating circuit. The oscillating frequency of the circuit depends on the position of the bar in the coil. Then the oscillating frequency is compared with the frequency of a reference oscillator and the frequency of the interference signal is used as a measure of the displacement of the bar.

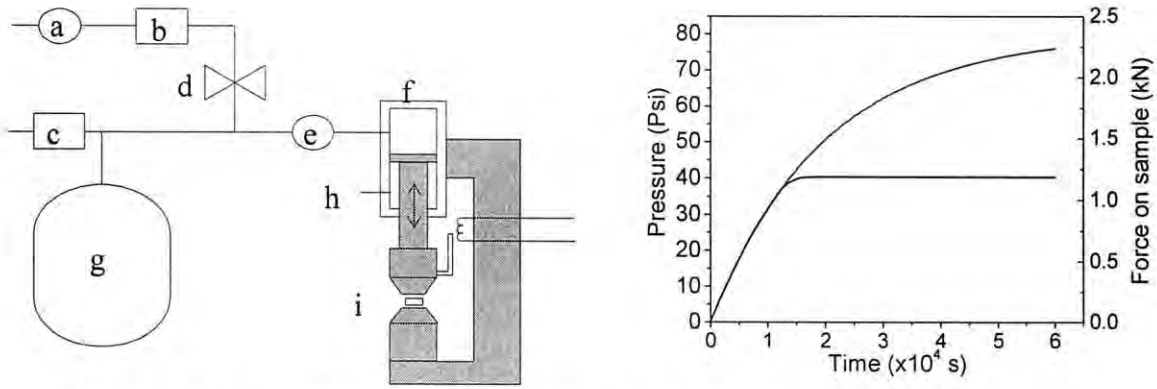

Fig. 6.3. Diagram of the press used to deform the samples. The different parts are: (a) 80 Psi regulator; (b) and (c) electromagnetic valves; (d) pressure rate regulation valve; (e) 40 Psi regulator; (f) piston; (g) 20 l buffer tank; (h) vents; (i) sample and (h) displacement detector. The graph shows the pressure changes in the piston during the deformation cycle which starts with opening valve (b) and ends after a period by closing valve (b). The force applied on the sample depends on the duration of the deformation cycle. The pressure in the buffer (g) is also shown.

6.3 Results

In this investigation, the ageing procedure is at a temperature of 100°C over relative short times up to a maximum of 10 h. During the ageing of previously quenched samples (heated at 500°C for 1 h and then fast cooling to RT) we observed the conversion of the 419 nm band associated with dipoles and dimers to the 427 nm band associated with Suzuki phase and trimers. We suspected that the aggregates formed in our experiment are probably trimers. This fact was confirmed by measuring the temperature at which the 427 nm band disappears during linear heating at a rate of 0.1 K/s. For the Suzuki phase this would be expected in the temperature range 363 – 423 K, however in our case the emission band disappears in the temperature range from 430 – 460 K corresponding to trimers as it was pointed out by Martinaga [Martinaga 1988].

Fig. 6.4A shows the emission spectra of PL, AG and TL at different ageing times at 100°C. The PL emission spectra measured during 360 nm excitation, show clearly the increase of the aggregate band around 427 nm with increasing ageing time at the cost of the dipole emission band at 419 nm. In the AG and TL emission spectra a strong increase of intensity and shift from dipoles to aggregates is also observed. This result suggests that the production of F and H centers responsible for the observed AG and TL is more efficient in the vicinity of aggregates than in the vicinity of dipoles. Furthermore, it is observed that aggregates are relative more efficient in TL than in AG. Within the TL, aggregates are more efficient in the high temperature peaks (around 220 K) than in the low temperature peaks (around 120 K).

Fig 6.4B shows similar measurements of luminescence but now for a sample which was 5% plastically deformed before the ageing procedures. The time to perform the deformation was about 1 h, which was not sufficient long to prevent crack formation. Nevertheless the sample remained in one piece. In this sample appears that the participation of the aggregates in the TL and AG is much less pronounced than in the undeformed sample. Before the ageing process, AG immediately after the deformation increases significantly with respect to that of the AG of the undeformed sample. Furthermore the emission spectrum of the AG is dominated by the dipole emission around 419 nm. After ageing, however, the intensity

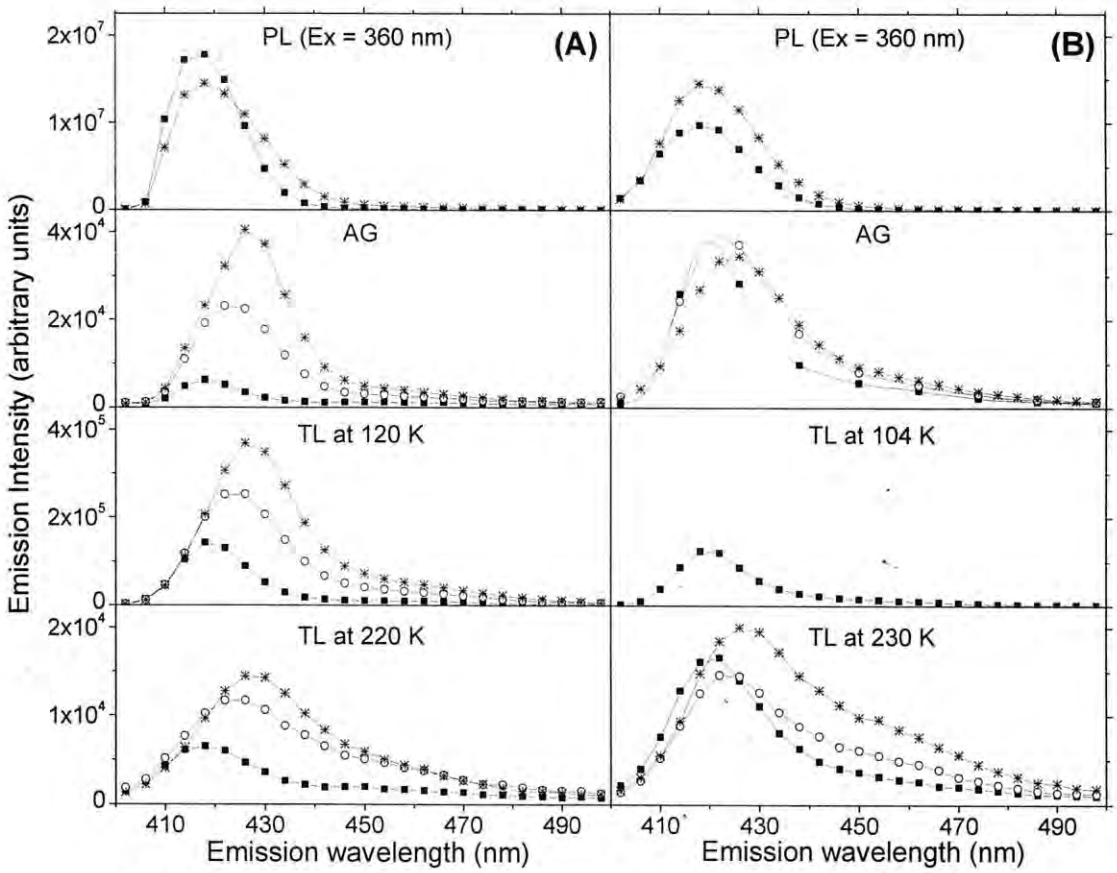

Fig. 6.4. Emission spectra of PL, AG and TL of a KCl:Eu sample ageing at 100°C for different periods: 0 h (squares), 5 h (open circles) and 10 h (stars). (A) for an undeformed same and (B) for a 5% deformed sample. In both cases, the sample was previously annealed at 500°C for 1 h.

of AG and TL does not change significantly but the participation of aggregates becomes more evident.

In another sample, also about 5% deformed but during a much shorter period (only a few seconds provoking the formation of cracks and that the sample broke into two parts) we observed no contribution of aggregates at all in none of the emission spectra. In the latter sample we expect a larger content of dislocation lines than in the slowly deformed sample, suggesting that the aggregation depend on the dislocation content. The TL glow curves change significantly after deformation, nevertheless one can identify two temperature ranges in which thermoluminescence occurs: the first one at 50 – 150 K and the second one at 200 – 280 K. After ageing, the TL of the lower temperature region disappears except for some luminescence at the beginning of the readout which is probably a residue of the AG signal (Fig. 6.5A).

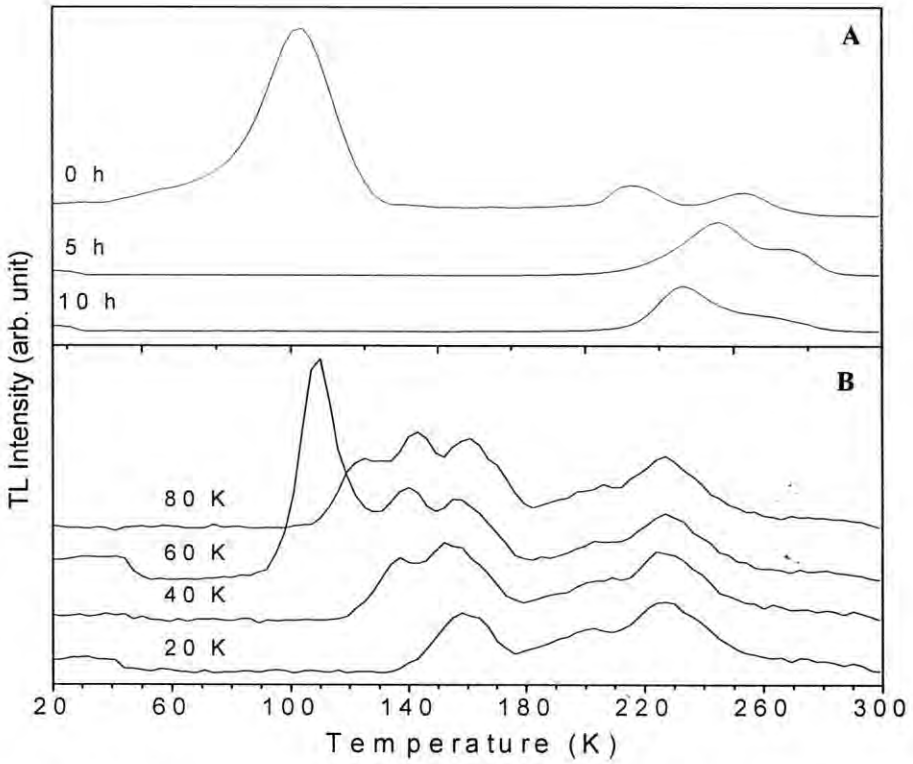

Fig. 6.5. TL glow curves of deformed samples for different ageing periods at 100°C (A) and different irradiation temperatures (B). The sample of (B) was aged in total 10 h at 100°C and stores for several days at RT.

For the rapidly deformed sample the AG and TL were measured at different irradiation temperatures (Fig. 6.5B). The AG was measured at the same temperature as that of irradiation while for the TL measurement the sample was cooled down to 20 K before the TL readout started. In this series of measurement we observed an extra TL peak around 160 K for the 20 K irradiation which was not present in the previous measurements after different ageing times. This is probably the result of storing the sample at room temperature for several days. At increasing radiation temperature appears several new TL peaks in the low temperature region of the TL curve. Further we observe the emission at the beginning of the TL measurement for irradiation temperatures lower than 60 K. This is notable since the temperature at which this emission occurs is lower than the irradiation showing that a thermal stimulated mechanism for the emission seems to be excluded.

The AG decay curves depend much on the irradiation temperature and behave like an exponential decay for an irradiation temperature of 40 K and higher (Fig. 6.6). We see also an

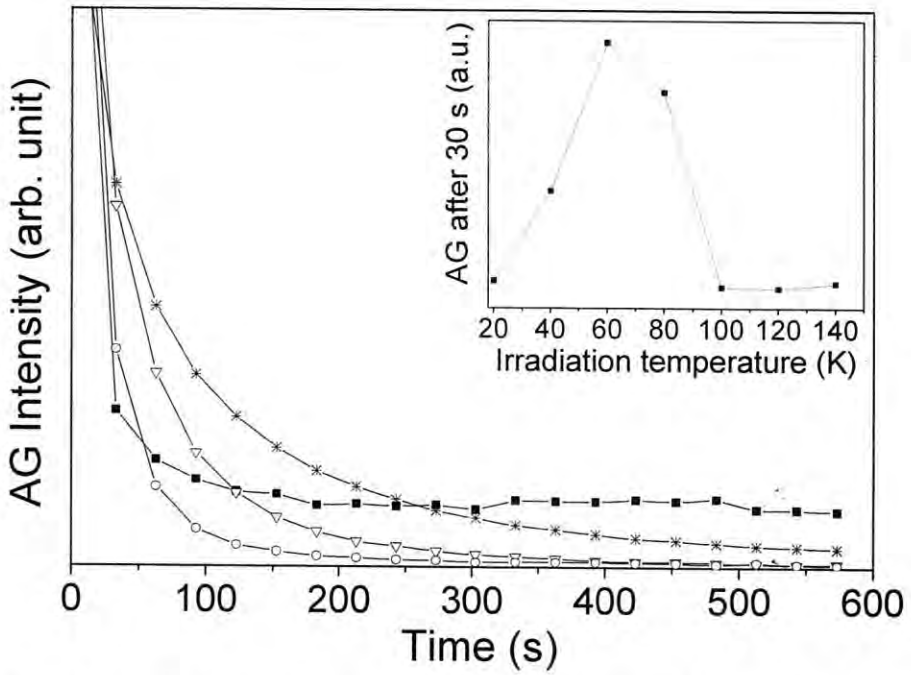

Fig. 6.6. AG decay curves of a 5% deformed sample measured at different irradiation temperatures: 20 K (squares), 40 K (open circles), 60 K (stars) and 80 K (open triangles). The intensity is scaled such that the shape of the decay curves could be compared. The insert shows the intensity of the AG after 31 s as a function of the irradiation temperature.

increase of AG around 60 K. This behaviour indicates the existence of a TL trap with peak temperature around 60 K. The fact that we can not detect this TL peak in the glow curves suggests that this peak is also generated around 60 K.

6.4 Discussion and conclusions

The results show several interesting features of the deformed samples (with many dislocation lines). On the one hand, the formation of aggregates during the ageing process is strongly reduced with respect to undeformed samples (with few dislocation lines). The aggregation reaction may be represented by the following reaction equation:

$$nX \leftrightarrow X_n \qquad [6.1]$$

The equilibrium of this reaction depends on temperature, volume, and number of dipoles. If the temperature or the volume are increased, or the number of dipoles is decreased the equilibrium shifts to the left of eq. [6.1]. Since the temperature of the compared samples is equal we must conclude that either the volume in which the reaction takes place is increased or that the number of dipoles in the reaction volume is decreased. Thus the created dislocation lines serve either as the reaction volume or as traps for Eu-v_c dipoles. In both cases the number of dipoles in dislocation lines grows so that the observed increase of AG in the dipole band in the deformed samples is consistent with the alternative model proposed in Chapter 3.

On the other hand we see also that the aggregates have a relative high AG response with respect to dipoles in not deformed samples. If the reason for this is that aggregates are at dislocation lines then it is tempting to assume that the reaction volume is formed by dislocation lines. With this assumption the mechanism for the formation of small aggregates would thus be that dipoles migrate first to dislocation lines. That this reaction is more likely than the reaction with other dipoles is a reasonable assumption because of the large reaction cross-section of dislocation lines. Once in the dislocation lines they migrate relatively fast and may react with other dipoles in the dislocation lines to form aggregates. Dipoles and aggregates in dislocation lines show AG but dipoles in the bulk do not.

GENERAL CONCLUSIONS AND PERSPECTIVES

The goal of the work described in this thesis was to get a better understanding of the mechanisms involved in UV induced afterglow and thermoluminescence at low temperature. An important step in the development of the thesis was that we changed our approach to the treatment of defect formation in alkali halides. Instead of the electron being the mobile entity in the processes of afterglow and thermoluminescence we considered the H center as the mobile entity. Electron and hole recombination was replaced by F–H center recombination. Rigorously applying this approach led us to a model for afterglow based on migration of H centers through dislocation lines and subsequent recombination with F centers. Taking this model as a working hypothesis we studied the afterglow and thermoluminescence phenomena experimentally and theoretically. The main experimental results and the conclusion deriving from them, are summarized below:

- A similar creation-emission spectra between AG and TL has been observed in different materials showing the correlation of both phenomena. The creation spectra lies around the high energy absorption band ascribed to the Eu impurity and the emission spectra corresponds to the characteristic Eu luminescence. This correlation means that the mechanism of formation of defects is common for both phenomena. The AG recombination is due to the non-trapped H centers which return to the F center position. The TL is due to those H centers thermally released from their traps which randomly migrate to the origin and recombine. In both cases, the energy of the F–H recombination is transferred, in some way, to the Eu impurity which emits its luminescence.
- The curvature of the AG decay decreases monotonically as the irradiation time is increased. This fact shows that the AG is given by the integration of many independent recombination processes between correlated pairs activated at different instants between

the beginning and ending of the irradiation period. The decay curve fit to the migration model with some deviations which initially were assigned to the participation of some thermally activated process.

- The TL glow curve in the temperature range 20 – 300 K confirms the formation of stable interstitial halogen atoms by the UV irradiation. However, some of the TL peaks observed after UV irradiation coincide with peaks that were earlier associated with electron traps.
- It was confirmed that the PL emission spectra at RT changes significantly after different thermal treatments in a KCl:Eu crystal. However a better discrimination of the bands was obtained in the PL spectra at low temperatures around 20 K. In this way, it was possible to identify at least six independent emission bands of which some of them are formed by two or more Gaussian peaks. This emission bands were tentatively assigned to different phases of the Eu impurity.
- The emission spectra of the AG and TL presents the emission bands identified in the PL with different relative ratios. A detailed analysis allows to establish the different participation of the Eu phase in the AG and TL phenomena: dipoles are more efficient to the production of the AG and TL when the crystals was submitted to a long thermal treatment at 200°C than after quenching from 500°C; the impurity aggregated phases are in general more efficient than dipoles.
- The creation spectra of the AG and TL to the different emission bands were almost similar and independent of the excitation spectra of the PL. This fact motivated us to conclude that the initial process in the creation of stable defects in Eu-doped alkali halides is not related to a transition on the Eu^{2+} impurity but in the lattice around it.
- Experiments in which we introduced extra dislocation lines by deforming the material show that the AG increases significantly with respect to that measured before the deformation. Furthermore, the emission spectra is dominated by the dipole emission band showing a less pronounced participation of aggregates.

From these investigations we can formulate the following hypothesis:

1. Aggregation of impurity ions occurs mainly near dislocations because, firstly, impurity ions migrate faster along dislocation lines causing the aggregation rate to increase and

secondly the impurity ions are trapped into dislocations where they remain mobile along the dislocation.

2. Radiation induced defect formation at low temperature occurs mainly around dislocations because they may serve as guiding lines for the H centers to separate from the F center to form stable F–H center pairs. Here it is again assumed that the migration of H centers in dislocation lines is fast compared to the migration in the bulk at temperatures too low to allow the H-center migration through the bulk.

To continue this line of investigation, we proposed some experiments which could be actually performed in our laboratory:

- The combination of thermal and deformation treatments produces significant changes in the AG and TL phenomena. The work present in Chapter 6 is a preliminary study and a deeper analysis of the process involved would be necessary.
- In the tunneling recombination, the F–H pair leads to an α–I pair which recombines not radiatively in pure alkali halides. However in Eu-doped alkali halides it could be possible that the recombination energy is transferred to the Eu impurity leading its characteristic luminescence. To investigate this point, we proposed to study the TL process at temperatures below 20 K where the presence of stable α–I pairs is expected.
- In X-irradiated alkali halides, the production of stable defect centers occurs mainly in the perfect lattice. We proposed to extend our study of AG/TL to X-irradiated Eu-doped alkali halides at low temperature. In this conditions, the Eu luminescence was only observed after F-light illumination of the crystal, however, there are some discrepancies about the mechanisms involved which we would clarify with our experiments.
- In our experiments under continuous UV-illumination, the trapped defects are accumulated leading to an intense TL signal. This fact difficult the analysis of the AG process at increasing temperature. Therefore, we proposed to study the AG luminescence after irradiation with a pulsed lamp at different irradiation temperatures. In this way, we expected to minimize the contribution of the thermally assisted process in the AG decay. Furthermore, the UV intensity of a pulsed lamp is higher than that of a continuous lamp which will increase the rate of created defects.

- In some Eu-doped alkali halides like KBr:Eu, the exciton absorption band lies just above 200 nm. Then, we proposed the detailed study of these materials under UV irradiation to clarify if the recombination mechanism also involves the Eu impurity.

Finally, the importance of the work also lies in the possible application in the production of nanowires using dislocations as seeds. Indeed a following-up project has been proposed to investigate the mechanism and the kinetics of the aggregation process in alkali halides taking the above mentioned points as a working hypothesis. Part of that project will be dedicated to develop and improve methods to distinguish defects and another part to the fabrication and characterization of nanowires fabricated by dislocation lines.

REFERENCES

Aceves R, Pérez-Salas R, Barboza-Flores M, *J. Phys.: Condens. Matter* **6**, 10397, 1994.

Aguilar G M, García-Solé J, Murrieta H S, Rubio J O, *Phys. Rev. B* **26**, 4507, 1982.

Aguirre de Cárcer I, Cussó F, Jaque F, *Phys. Rev. B* **38**, 10812, 1988.

Aguirre de Cárcer I, *PhD Thesis*, Madrid, 1989.

Alvarez-Garcia S, Piters T M, Barboza-Flores M, *Radiat. Meas.* **33**, 813, 2001.

Alvarez-Garcia S, Piters T M, *Radiat. Eff. Defects Solids* **158**, 281, 2003

Alvarez-Garcia S, Piters T M, *J. Phys.: Condens. Matter* **17**, 181, 2005.

Babin V, Krasnikov A, Zazubovich S, *Radiat. Eff. Defects Solids* **158**, 227, 2003.

Behr A, Peisl H, Waidelich W, *Phys. Lett.* **24A**, 379, 1967.

Chen R, McKeever S W S, *Theory of Thermoluminescence and Related Phenomena* (Singapore, World Scientifc), 1997.

Chowdari B V R, Itoh N, *Phys. Status Solidi B* **46**, 549, 1971.

Delbecq C J, Toyozawa Y, Yuster P H, *Phys. Rev. B* **9**, 4497, 1974.

García J M, Hernández J A, Carrillo E H, Rubio J O, *Phys. Rev. B* **21**, 5012, 1980.

Hesse S, Seggern H v, *J. Phys. D* **37**, 863, 2004.

Hirth J P, Lothe J, *Theory of dislocations* (USA, McGrawn-Hill), 1968.

Horowitz Y S, Yossian D, *Computerised glow curve deconvolution: application to thermoluminescence dosimetry* (England, Nuclear Technology Publishing), 1995.

Hull D, Bacon D J, *Introduction to dislocations* (Pergamon Press), 1989.

Ikezawa M, Kojima T. *J. Phys. Soc. Jpn.* 27, 1551, 1969.

Jiménez de Castro M, Álvarez-Rivas J L, *Phys. Rev. B* **19**, 6484, 1979.

Kao K J, Perlman M M, *Phys. Rev. B* **19**, 1196, 1979.

Kayanuma Y, *Defect Processes Induced by Electronic Excitation in Insulators*, ed. Itoh N (Singapore, World Scientific) Chapter 2, 1989.

Kimura T, Inabe K, *Jpn. J. Appl. Phys.* **37**, 2670, 1998.

Kotomin E, Popov A, Hirai M, *J. Phys. Soc. Jpn.* **63**, 2602, 1994.

Larios-Cota, A S *Graduated Thesis*, Universidad de Sonora, 1980.

López F J, Murrieta H S, Hernández J A, Rubio J O, *Phys. Rev. B* **22**, 6428, 1980.

Lushchick A Ch, Lushchick B Ch, *Proc. Russ. Acad. Sci.* **56**, 88, 1992 [cited by Kotomin 1994]

Martinaga F M, Nunes L A O, Zilio S C, Castro J C, *Phys. Rev. B* **37**, 993, 1988.

Muñoz A F, Cabrera E B, Riveros H R, Patrón M, Rubio O J, *Phys. Rev. B* **31**, 8196, 1985.

Nanto H, Endo F, Hirai Y, Nasu S, Taniguchi S, Takeushi N, *J. Appl. Phys.* **75**, 7493, 1994.

Nensel B, Thielemann P, Decker G, *J. Appl. Phys.* **83**, 2276, 1998.

Opyrchal H, Nierzewski K D, *Phys. Status Solidi B* **95**, 251, 1979.

Opyrchal H, Nierzewski K D, Macalik B, Mladenova M, *Phys. Status Solidi B* **135**, 141, 1986.

Opyrchal H, Nierzewski K D, Macalik B, *Solid State Commum.* **71**, 783, 1989.

Piters T M, *PhD Thesis*, Delft, 1993.

Piters T M, Alvarez-Garcia S, *Radiat. Eff. Defects Solids* **157**, 705, 2002

Press W H, Flannery B P, Tekolski S A, Vetterling, *Numerial Recipes: FORTRAN version* (New York , Cambridge University Press), 1990.

Purdy A E, Murray R B, *Solid State Commum.* **16**, 1293, 1975.

Rubio J O, Murrieta H S, Hernández J A, López F J, *Phys. Rev. B* **24**, 4847, 1981.

Rubio J O, Flores M C, Murrieta H S, Hernández J A, Jaque F, López F J, *Phys. Rev. B* **26**, 2199, 1982.

Rubio J O, *J. Phys. Chem. Solids* **52**, 101, 1991.

Rüter H H, Seggern H v, Reininger R, Saile V, *Phys. Rev Lett* **65**, 2438, 1990.

Schlapp M, Seggern H v, Massalovitch S, Ioffe A, Conrad H, Brueckel T, *Appl. Phys. A* **74**, S109, 2002.

Schlapp M, Conrad M, Seggern H v, *J. Phys. D* **37**, 2607, 2004.

Seggern H v, *Brazilian Journal of Physics* **29**, 254, 1999.

Shluger A L, *PhD Thesis*, Moscow, 1981 [cited by Kotomin 1994].

Song K S, Williams R T, *Self-Trapped Excitions* (Berlin, Springer), Chapters 1, 5, 6, 1996.

Suzuki K, *J. Phys. Soc. Jpn.* **10**, 794, 1955.

Suzuki K, *J. Phys. Soc. Jpn.* **16**, 67, 1961.

Tanimura K, Fujiwara M, Okada T, Suita T, *Phys. Lett.* **50A**, 301, 1974.

Tanimura K, Okada T, *Phys. Rev. B* **21**, 1690, 1980.

Tashiro T, Takeuchi S, Saidoh M, Itoh N, *Phys. Status Solidi B* **92**, 611, 1979.

Toyozawa Y, *Physica* **117B/118B**, 23, 1983 [cited by Kayanuma 1989].

Vassilev Y, Karamikhailova M, Mladenova M, Georgiev M, *Phys. Status Solidi B* **100**, 463, 1980.

Appendix 1:

Afterglow luminescence by tunneling recombination

The time dependency of the AG decay by a tunneling mechanism was analyzed by several authors to explain: (*i*) the AG recombination in KCl:Ag and KCl:Tl crystals due to tunneling between impurity atoms (Ag^0 or Tl^0) and V_k centers [Delbecq 1974; Tashiro 1979] and (*ii*) the photostimulated AG of previously irradiated KCl:Eu associated to tunneling between F* centers and Eu^{3+} ions [Vassilev 1980].

The probability per second $p(R)$, of the radiative tunneling recombination between a defect pair separated by a distance R is given by

$$p(R)=\frac{1}{\tau}\exp(-2\alpha R) \qquad \text{[A1.1]}$$

at least within a small range ΔR ($<< R$).

For simplicity, it was assumed that just after irradiation, the recombination pairs are distributed completely at random with concentration N_0. Then the concentration of pairs having a separation in the interval $(R, R+dR)$ is given by

$$n(R)=N_0^2 4\pi R^2 dR \qquad \text{[A1.2]}$$

as long as $N_0R^3 << 1$.

The concentration of pairs surviving at time t is then given by

$$n(R,t)=N_0^2\exp[-p(R)t]4\pi R^2 dR \qquad \text{[A1.3]}$$

For large t ($>>\tau$), this equation has a sharp step at $R = R_c(t)$ defined by

$$p(R_c)t=1 \qquad \text{[A1.4]}$$

which results in

$$R_c(t)\approx\frac{1}{2\alpha}\ln\left(\frac{t}{\tau}\right) \qquad \text{[A1.5]}$$

where the width of the step α^{-1} is much smaller than R_c.

This means that the recombinant pairs proceeds with a well-defined frontier $R_c(t)$ as times goes on. This frontier radius moves forward very rapidly in the initial stage but more and more slowly as times goes on.

The intensity of the afterglow per unit volume $I(t)$, is proportional to

$$\int\left(-\frac{dn(R,t)}{dt}\right)=N_0^2\exp[-p(R)t]4\pi R^2dR \qquad \text{[A1.6]}$$

The main contribution comes from a narrow region around $R=R_c(t)$. Then, the slowly varying factors can be extracted outside the integral, to get

$$I(t)=t^{-1}A\left[4\pi R^2N_o^2\left(\frac{d}{dR}\ln p(R)\right)^{-1}\right]_{R=Rc(t)}$$

$$=t^{-1}A\left[8\pi R^2N_0^2\alpha\right]_{R=Rc(t)} \qquad \text{[A1.7]}$$

In this way, $I(t)$ follows a t^{-1} decay function with an amplitude which depends on the frontier radius R_c.

Appendix 2:

Example of experimental program

Experiment program designed to run emission scans during AG and TL after irradiation at different temperatures, wavelengths and times. Column "content" shows the content of each register, being a "parameter description" when *cursive* and a "keystroke procedure name" when *bold.*

	Register number	Content	Description
LOOP DATA	1	*Start Irr Tem (K)*	Initial irradiation temperature
	2	*Incr Irr Tem (K)*	Increment between irradiation temperatures
	3	*Num Irr Tem's*	Number of irradiation temperatures
	4	*Start Ex (nm)*	Initial irradiation wavelength
	5	*Incr Ex (nm)*	Increment between irradiation wavelengths
	6	*Num Ex's*	Number of irradiation wavelengths
	7	*Start Irr Tim (s)*	Initial irradiation time
	8	*Incr Irr Tim (s)*	Increment between irradiation times
	9	*Num irr Tim's*	Number of irradiation times
	10	*1*	
	11	*1*	
	12	*Num loops TL:*	Number of TL spectra
	...		
	19	*Keys-running*	Store the name of the *keystroke procedure* is running
	20	*Reg-running*	Store the register number of the *keystroke procedure* is running
	21	**shuterxm cl-cl**	Close excitation and emission shutters
	22	**initkrat**	Run *kratoss.exe* to check the actual wavelength of the excitation monochromator

EXPERIMENT PROGRAM			
	23	**loadprg**	Run *talk.exe* to load the heating program in PC2
	24	**dataexp**	Run a *window* asking the irradiation data and save them in registers 1-12. Also ask the file name where the experiment data will be saved (*Name01.spt*, *Name02.spt*…) and save them in registers 79-80
	25	**delfiles**	Run *delfiles.exe* to check if the files with the previous names exist and delete them
	26	**daemsc**	Run a *window* asking the parameters of the emission spectra and save the experiment file with the name in register 89
	27	**progloop 01tem**	Initiate loop of irradiation temperatures
	28	**progloop 02wav**	Initiate loop of irradiation wavelengths
	29	**progloop 03tim**	Initiate loop of irradiation times
	30	**shuterxm cl-cl**	Close excitation and emission shutters
	31	**setirtem**	Set the irradiation temperature corresponding to this loop (01) and run the *tstab.exe* program in PC2 to stabilize the temperature
	32	**setirwav**	Set the irradiation wavelength corresponding to this loop (02) and run the *kratoss.exe* program to change the excitation monochromator wavelength
	33	**setirtim**	Set the irradiation time corresponding to this loop (03) and irradiate the sample during that time
	34	**ag20**	Close the excitation monochromator and run 20 emission spectra during AG decay
	35	**checktem**	Check the irradiation temperature, if it is 20 K, then wait 300 s, otherwise run the *tstab.exe* program in PC2 to stabilize the temperature at 20 K
	36	**commandd rpf**	Run *talk2.exe* to communicate to PC2 that initiates the heating ramp
	37	**progloop 04tl**	Initiate loop of TL scans
	38	**runexp**	Run a emission scan
	39	**endsloop 04**	Return to the beginning of loop04
	40	**saveloop**	Save the loop parameters
	41	**endsloop 03**	Return to the beginning of loop03
	42	**endsloop 02**	Return to the beginning of loop02
	43	**endsloop 01**	Return to the beginning of loop01
	44	**end**	End the program
	…		

	70		Last register to keystroke procedures in the program
PARAMETERS	71	*Loops01 rest*	Number of loops01 are resting
	72	*Loops02 rest*	Number of loops02 are resting
	73	*Loops03 rest*	Number of loops03 are resting
	74	*Loops04-rest*	Number of loops04 are resting
	..		
	76	*Irrad. temp*	Actual irradiation temperature to be read by the program *tstab.exe*
	..		
	79	*Name spt-file*	Name of the file where the experiment data will be stored
	80	*Num. spt-file*	Number of the file where the experiment data will be stored
	81	*1st pos. loop01*	Register number where initiates the first loop
	82	*1st pos. loop02*	Register number where initiates the second loop
	83	*1st pol. loop03*	Register number where initiates the third loop
	84	*1st pos. loop04*	Register number where initiates the fourth loop
	..		
	89	*Name Exp. File*	file name of the emission scan experiment
	90	*Erasable*	
	...		
	98	*Erasable*	
	99	**continue**	Called at the end of each keystroke procedure

Appendix 3:

Fitting of the thermoluminescence glow curve

The basic kinetic model of thermoluminescence (TL) assumes that the ionizing irradiation produces free electron and holes and that some of theses are trapped in local, discrete energy levels within the forbidden band. Theses trapping states are usually associated with defects of the crystal. When the sample is heated, the trapped charges escape from the trapping centers and then recombine with trapped charge carriers of the opposite sing.

The Randall and Wilkins theory describes the TL glow peak due to the thermally detrapping of an electron at a discrete energy level below the conduction band [Horowitz 1995]. It is assumed that the electron in the traps have a Maxwellian distribution of energy. Then the probability to escape from a trap of depth E at a temperature T is

$$p = s \exp(-E/kT) \qquad \text{[A3.1]}$$

where s is called the frequency factor (s^{-1}).

The rate of thermal excitation of the electrons from the trap is

$$\frac{dn}{dt} = -n\, s \exp(-E/kT) \qquad \text{[A3.2]}$$

where the retrapping probability was assumed to be negligible.

The TL intensity is proportional to the eq. [A3.2]. In the case of a linear heating: $T = T_0 + \beta t$ where T_0 is the initial temperature and β the heating rate, then the TL intensity is given by:

$$I(t) = c\, s\, n_0\, e^{-E/kT} \exp\left[\frac{-S}{\beta}\int_{T_0}^{T} e^{-E/kT'}\, dT'\right] \qquad \text{[A3.3]}$$

This expression describes the shape of an isolated glow peak when retrapping is negligible (first order kinetics) which are most of the cases observed in dosimetry. It is taken as a generally applicable equation, however it has not an analytical solution. Several approximated solutions has been proposed and extensively used in simulation studies.

In our case, the TL glow peak analysis was done with a computational program developed by T. M. Piters and co-workers (Tamtam) which is based on the approximated solution:

$$I(T) = A\, s\, e^{-E/kT} \exp\left[\frac{-s}{\beta}\frac{kT^2}{E} e^{-E/kT}\left(0.9920 - 1.620\frac{kT}{E}\right)\right] \qquad [A3.4]$$

where β is the heating rate and s and E defines the glow peak shape. To initiate the fitting is necessary to introduces approximated values of the pair E and $ln\ s$ to construct a proof function closed to the peak to be fitted. The program is not user friendly but after some practice allows easily to find the parameters of several peaks overlapping under the glow curve.

A more user friendly program based on *Windows* to fit experimental data is the non-linear fitting option of the *Origin* commercial software. The equation [A3.4] can be introduced as a user function and the fitting of isolated peaks is easily done. However to fit several peaks, the fitting function should be constructed as a sum of functions [A3.4] which results in a tedious work. The last version of this program (*Origin 7.0 Pro*) introduces a new option to fit easily a curve composed of several peaks of a used-defined peak function. The only condition of this fitting option is that the definition of the user-function should include the peak maximum and the width at half intensity. Therefore, we develop an analytical approximated expression of the glow curve solution which involves the previous both parameters.

The maximum temperature of the peak (T_M) was previously related to the E and S parameters by the expression:

$$\frac{\beta E}{kT_M^2} = S\, e^{-E/kT_M} \qquad [A3.5]$$

This relation was easily deduced by setting the derivate of $\ln I(t)$ from equation [A3.3] to zero.

There is not a reported expression to the width at half intensity and we will deduce it from another of the reported approximated solutions of equation [A3.3] given by:

$$I(T) = I_M \exp\left\{1 + \frac{E}{kT_M}\left(\frac{T - T_M}{T_M}\right) - \exp\left[\frac{E}{kT_M}\left(\frac{T - T_M}{T_M}\right)\right]\right\} \qquad [A3.6]$$

The temperatures T_c at half maximum intensity will be given by:

$$\exp\left\{1 + \frac{E}{kT_m}\left(\frac{T_c - T_m}{T_m}\right) - \exp\left[\frac{E}{kT_m}\left(\frac{T_c - T_m}{T_m}\right)\right]\right\} = \frac{1}{2} \qquad [A3.7]$$

defining the variable x like:

$$x \equiv \frac{E\left(T_c - T\right)}{k\,T_M^2} \qquad \text{[A3.8]}$$

equation [A3.7] can be resumed by

$$\exp(x) = x + 1 - \ln\left(\frac{1}{2}\right) \qquad \text{[A3.9]}$$

This equation has two solutions at $x_1 = -1.46119$ and $x_2 = 0.9852$. The width w is given by the difference of the temperatures T_1 and T_2 corresponding to the previous x_i values. Then the expression to w can be easily deduced:

$$w = \frac{\left(x_2 - x_1\right) k\,T_M^2}{E} = \frac{\left(2.44639\right) k\,T_M^2}{E} \qquad \text{[A3.10]}$$

Therefore the trap depth E can be expressed as a function of T_M and w by:

$$E = \frac{2.44639 k T_M^2}{w} \qquad \text{[A3.11]}$$

From equations [A3.5] and [A3.11] the parameter s as function of T_m and w is given by:

$$s = \frac{2.44639\beta}{w}\exp\left(\frac{2.44639\,T_M}{w}\right) \qquad \text{[A3.12]}$$

Using equations [A3.11] and [A3.12], the approximated solution [A3.4] can be expressed like:

$$I(T) = A\,\frac{2.44639\,\beta}{w}\exp\left[\frac{2.44639\,T_m}{w}\left(1-\frac{T_M}{T}\right)\right]* \\ \exp\left\{\frac{-T^2}{T_M^2}\exp\left[\frac{2.44639\,T_m}{w}\left(1-\frac{T_M}{T}\right)\right]*\left(0.9920-1.620\frac{wT}{2.44639T_M^2}\right)\right\} \qquad \text{[A3.13]}$$

This expression can be introduced in the Origin 7.0Pro as an user fitting function of a glow peak and effectively works. Therefore, to fit the glow curves, we initiate by looking for the approximated values of the fitting parameters of each peak using eq. [A3.13] in the *Origin 7.0Pro*. Then, the simultaneously fitting of the full glow curves at different irradiation times were performed using the *Tamtam* program.